X-ray Study on the Activity History of Sagittarius A* by Three-dimensional View of the Galactic Center

Ryunosuke Gando (= S. G. Ryu)

Department of Physics, Graduate School of Science, Kyoto University
Kitashirakawa Oiwake-cho, Sakyo-ku, Kyoto, 606-8502, Japan
`ryu@cr.scphys.kyoto-u.ac.jp`

This thesis was submitted to the above department on January 7, 2013
in partial fulfillment of the requirements
for the degree of Doctor of Philosophy in physics.

Abstract

Context. The most characteristic high-energy phenomena in the Galactic center (GC) are represented by strong K-shell emission lines from iron, particularly the 6.7 keV and 6.4 keV lines. The 6.7 keV line is from highly ionized iron in hot plasma (Galactic center plasma emission: GCPE) of $\sim 10^{7-8}$ K. The GCPE extends over the entire GC region for about 2° with monotonic flux decrease as a function of its distance from the central super massive black hole (SMBH), Sagittarius (Sgr) A*. The 6.4 keV line is from neutral iron in cold giant molecular clouds (MCs) in the central molecular zone (CMZ), such as Sgr B and Sgr A. The X-ray spectra of these MCs have non-thermal continuum emission with large equivalent width at 6.4 keV and exhibit strong absorption below 5 keV. These spectral features strongly support the X-ray Reflection Nebulae (XRNe) scenario; the X-rays are due to fluorescent and Thomson scattering from MCs illuminated by external X-rays. Since the fluxes of XRNe require a high X-ray luminosity for irradiation larger than those of any brightest Galactic X-ray sources, the potential candidate of the illuminating source is the SMBH Sgr A*. The time variabilities of the 6.4 keV line and the continuum hard X-rays reinforced the idea that the emissions from XRNe are due to a big X-ray flare (or flares) from Sgr A* in the past. According to rough estimations from the light-traveling time of projected distances between XRNe and Sgr A*, the flare should have occurred at about several hundred of years ago and the past X-ray luminosity must be about 10^6 times higher than present. However, the line-of-sight positions of MCs/XRNe were not well known, and hence quantitative estimation of light-traveling time and X-ray luminosity for the past flares was not possible.

Aims. In this thesis, we present an original self-consistent methodology to directly determine the three-dimensional (3-D) positions (projected 2-D plus line-of-sight positions) of multiple XRNe and quantitatively investigate the past activity history of Sgr A*.

Methods & Results. We carefully examined the X-ray spectra from the Suzaku observations on the Sgr B MC complex. The spectra consist of emissions from the XRNe and the GCPE; the GCPE is decomposed into two components, one with large absorptions of $N_{\rm H} \geq 10 \times 10^{22}$ H cm^{-2} (Abs1) and another with absorptions of $N_{\rm H} \sim 6 \times 10^{22}$ H cm^{-2} (Abs2). The large Abs1 is positively correlated with the 6.4 keV flux, and hence is due to the MCs/XRNe. The small Abs2 is nearly constant among all the XRNe, whose values correspond to the Galactic inter-stellar absorption between the GC and the Sun. We further testified and applied this spectral model to the other XRNe in the Sgr C, Sgr D, and Sgr E regions. Combing the two results of the GCPE spatial distribution as an ellipsoid around Sgr A* and the GCPE flux ratio between its part with Abs1 (behind XRN) and the other part free from Abs1 (in front of XRN), we derived the line-of-sight position for each XRN

inside the GCPE.

We obtained an overall view for the 3-D distribution of XRNe around the GC. We found that these XRNe, coincident with MCs in different radial velocities, are largely separated in the line-of-sight position with respect to Sgr A*. XRNe in Sgr B are mostly located in front; the most massive one in Sgr C is behind, while the other two are in front; those in Sgr E and Sgr D are located in front and slightly behind, respectively. These 3-D positions of XRNe are consistent with the MC structures in the bar potential suggested by the radio observations assuming possible Galactic dynamics (e.g., circular rotations). This enhances the reliability of our new method which directly determines the 3-D position. Using X-ray parameters of the 3-D positions, the fluxes, and the XRN column densities (Abs1), we finally reconstructed a long-term light curve of Sgr A*. During the past 50 to 600 years, the SMBH had been in a flare state with luminosities between $L_{\rm X} = 1$–3×10^{39} erg s^{-1}, which were far brighter than the present luminosity by a factor of $\sim 10^6$. The light curve was not flat top in the flare epochs, but exhibited significant variations within a factor of ~ 3. The fluctuations were also confirmed by observations of different short-term ($\sim$ 5 years) variabilities in the 6.4 keV flux, of either increase or decrease, from different XRNe in Sgr B and Sgr C. Thus, we concluded that the X-ray activity of Sgr A* in the past 600 years was not a simple single event, but consisted of multiple short flares occurred continuously and sporadically.

Contents

1 Introduction & Thesis Composition 1

2 Review 3

2.1 The Milky Way Galaxy and the Center Region 4

2.1.1 Basic Information of the Galaxy 4

2.1.2 Central Molecular Zone 8

2.2 Super Massive Black Hole, Sagittarius (Sgr) A* 8

2.2.1 Presence and Basic Properties 8

2.2.2 X-ray Observations of Sgr A* 10

2.3 Thermal X-rays from the Galactic Center 14

2.3.1 Early X-ray Observations on the Galactic Plane 14

2.3.2 The Fe XXV Kα (6.7 keV) Diffuse Emission and the GC Hot Plasma . 16

2.3.3 The S XV Kα (2.45 keV) Diffuse Emission and Possible Presence of Large-scale Low-temperature Plasma 17

2.3.4 Latest Results 18

2.4 Fe I Kα Diffuse Emissions in the Galactic Center 19

2.4.1 The 6.4 keV Line and its Origins 19

2.4.2 Observational Results of the 6.4 keV Emissions 23

2.4.3 X-ray Reflection Nebula and Past Activities of Sgr A* 24

2.5 Objectives and Approach of the Thesis 27

3 Instruments **29**

3.1 Overview of the Suzaku Satellite 29

3.2 X-Ray Telescope (XRT) 33

3.2.1 Overview of the XRT 33

3.2.2 In-flight Performance 35

3.3 X-ray Imaging Spectrometer (XIS) 37

3.3.1 Introduction of X-ray Charge Coupled Device 37

3.3.2 Overview and Specifications of XIS 38

3.3.3 In-flight Performance 41

3.4 Suzaku Advantages in the Study of the Galactic Center 44

4 Study of Sagittarius B **45**

4.1 Observation and Data Reduction 45

4.2 Data Analysis and Results 46

4.2.1 Overall Features of the X-Ray Images 46

4.2.2 Complex Components in the Spectra 48

4.2.3 Model Constructions and Fitting 52

4.3 Discussion for Sgr B 58

4.3.1 Justifications of Model Constraints and Assumptions 58

4.3.2 Line-of-Sight Distribution of Sgr B MCs in the GCPE 59

4.3.3 XRN Features in Sgr B 61

4.3.4 The Correlation of CS Line and 6.4 keV Line 62

5 Study of Sagittarius C **65**

5.1 Observation 65

5.2 Data Analysis and Results 66

5.2.1 Images 66

5.2.2 Spectral Model 68
5.2.3 Spectral Fitting 69
5.3 Discussion for Sgr C 73
5.3.1 Association with the Radio MCs 73
5.3.2 Two-temperature Structure of the GC Plasma and the XRN Parameters 74
5.3.3 Time Variability of the 6.4 keV Line and the Flare Property of Sgr A* 75

6 Study of Sgr D & Sgr E **77**
6.1 Observation 77
6.2 Data Analysis and Results 78
6.2.1 Images 78
6.2.2 Spectra 78
6.3 Discussion for Sgr D and Sgr E 80
6.3.1 Association with the Radio MCs 80
6.3.2 Origin of the 6.4 keV Line 81

7 Overall Results & Discussion **83**
7.1 Longitude Distribution of Physical Parameters 83
7.2 Face-on Distribution of XRNe in the GC Region 85
7.2.1 Computation of Line-of-sight Position 85
7.2.2 Association with the CMZ 90
7.3 Active History of Sagittarius A* 93
7.3.1 Derivation of X-ray Light Curve 93
7.3.2 Behaviours of the Past Flare State 94
7.3.3 Interpretation as Low-Luminosity AGN 97

8 Conclusions **99**

References **100**

List of Figures and Tables **106**

Acknowledgment **113**

Chapter 1

Introduction & Thesis Composition

Thanks to its vicinity, the central several-hundred-parsec region of our Galaxy (GC; Galactic center) provides an unique environment for detailed observational studies on high-energy phenomena associated with the super massive black hole (SMBH). Two major discoveries of the GC region are represented by the iron K-shell lines. One is the hot plasma of 10^{7-8} K emitting ionized iron (Fe XXV Kα) line at 6.7 keV (e.g., Koyama et al. 1986, 2007c). This hot plasma extends over the entire GC region for about 2° with monotonic decrease from the center (Uchiyama et al. 2011, 2012). Another prominent component is the 6.4 keV line of neutral iron (Fe I Kα) found from cold (typically $\sim$70 K) giant molecular clouds (MCs) in the central molecular zone (CMZ; Morris & Serabyn 1996), such as Sagittarius (Sgr) B, Sgr C, and Sgr A (e.g., Koyama et al. 1996; Murakami et al. 2001; Muno et al. 2007). The spectra of these 6.4 keV bright MCs exhibit common features of large equivalent width ($EW \geq 1$ keV) at 6.4 keV and strong absorption ($N_{\mathrm{H}} \geq 10^{23}$ H cm^{-2}) at the continuum X-rays below 5 keV. Rapid 6.4 keV time variabilities, consistent with injecting source of light speed, are also observed from the MCs (e.g., Inui et al. 2009; Ponti et al. 2010). These results strongly suggest external X-rays as the primary source producing the 6.4 keV line rather than the charged particles (electron or proton; Yusef-Zadeh et al. 2007; Dogiel et al. 2011).

In the context of the X-ray origin, a luminous external source emitting hard X-rays (over the Fe absorption edge at 7.1 keV) is required to irradiate the MCs and generate the fluorescent 6.4 keV emission, i.e., the X-ray reflection Nebulae (XRNe; Koyama et al. 1996; Sunyaev et al. 1993). Since no present Galactic X-ray source is bright enough to explain the observed 6.4 keV intensities from XRNe, the SMBH with a mass of 4×10^{6} $M_{\odot}$ (Ghez et al. 2008) sited in the GC (i.e., Sgr A*) is believed to be the most reasonable candidate (e.g., Koyama et al. 1996; Ponti et al. 2010; Nobukawa et al. 2011). Previous works proposed past flare from Sgr A*, with X-ray (2–10 keV) luminosity on the order of

$L_{\rm X} \sim 10^{39}$ erg s^{-1}, occurred several hundreds years ago. However, this picture is not clear due to poor understanding of the three-dimensional position of the MCs.

In this thesis, we present an original self-consistent methodology to measure the three-dimensional (line-of-sight) position of multiple XRNe and quantitatively investigate the past active history of Sgr A*. Following is the composition. In chapter 2, we review the background knowledge of the GC region to introduce the objectives of this thesis. In chapter 3, we describe principles and specifications of the X-ray satellite "Suzaku" and the onboard instruments used for the data analysiss. In chapter 4, we construct a spectral model for the Galactic center diffuse X-rays and propose a new methodology to investigate positions of the Sgr B MCs along the line of sight: a correlation study of the flux of the 6.4 keV line from the MCs and the line-of-sight absorption of the Galactic center plasma emissions. In chapter 5, we study the XRNe in the Sgr C region and testify the spectral model proposed in Sgr B. We investigate the short-term time variability of the 6.4 keV line. We also establish the spectral composition for the Galactic center plasma emission. In chapter 6, we apply the model developed in Sgr B and Sgr C (chapter 4–5) to the Sgr D and Sgr E regions located near the boundary of the CMZ. We probe and investigate the farthest molecular clouds from the GC for the 6.4 keV emissions. In chapter 7, we summarize and analysis the results obtained in chapter 4–6 to quantitatively determine the line-of-sight positions for the multiple XRNe/MCs over the GC and discuss their three-dimensional distribution in association with the CMZ. We finally derive an X-ray light curve for Sgr A* and discuss its active history over the past six centuries.

Throughout this thesis, we use the Galactic coordinates, where the horizontal and vertical axes are the Galactic longitude (l) and latitude (b), respectively. The positive and negative directions of l correspond to east and west, respectively. We adopt 8.0 kpc (Ghez et al. 2008) as the distance between the Sun and Sgr A* ($l = -0.^\circ056$, $b = -0.^\circ046$; Yusef-Zadeh et al. 1999), then 1.0 degree corresponds to 140 pc (or 456 ly) at the GC. The parameter uncertainties are quoted at the 90% statistical confidence-level (1.64 σ) range unless noted otherwise.

Chapter 2

Review

In this chapter, we review the important topics of the Galactic center to explain the objectives of this thesis.

Contents

2.1 The Milky Way Galaxy and the Center Region 4

2.1.1 Basic Information of the Galaxy 4

2.1.2 Central Molecular Zone 8

2.2 Super Massive Black Hole, Sagittarius (Sgr) A* 8

2.2.1 Presence and Basic Properties 8

2.2.2 X-ray Observations of Sgr A* 10

2.3 Thermal X-rays from the Galactic Center 14

2.3.1 Early X-ray Observations on the Galactic Plane 14

2.3.2 The Fe XXV Kα (6.7 keV) Diffuse Emission and the GC Hot Plasma 16

2.3.3 The S XV Kα (2.45 keV) Diffuse Emission and Possible Presence of Large-scale Low-temperature Plasma 17

2.3.4 Latest Results 18

2.4 Fe I Kα Diffuse Emissions in the Galactic Center 19

2.4.1 The 6.4 keV Line and its Origins 19

2.4.2 Observational Results of the 6.4 keV Emissions 23

2.4.3 X-ray Reflection Nebula and Past Activities of Sgr A* 24

2.5 Objectives and Approach of the Thesis 27

2.1 The Milky Way Galaxy and the Center Region

2.1.1 Basic Information of the Galaxy

Composition and Size

The Milky Way is the galaxy hosting our Earth and solar system, which is usually called "the Galaxy" (figure 2.1). As revealed by early observations in the 20th century (e.g., Oort et al., 1958; Okuda et al., 1977), the Galaxy is a typical spiral galaxy with concentric structure consisting of three main components: the disk, the bulge, and the halo. The disk has a pancake-like shape which is approximately ∼30 kpc in diameter and ∼0.3 kpc in thickness. The bulge is a bar-like spheroid, with major radius of ∼2 kpc and minor radius of ∼1.0 kpc, sitting on the disk. The bulge (bar) orientation is about 20° with respect to our line of sight. The very central ∼500 pc region of the bugle is the "Galactic center (GC)". The halo is a big sphere with diameter of ∼50 kpc wrapping up the disk and the halo. The solar system is located on the disk and is about ∼8 kpc away from the center. A global view of the Galaxy is shown in figure 2.2.

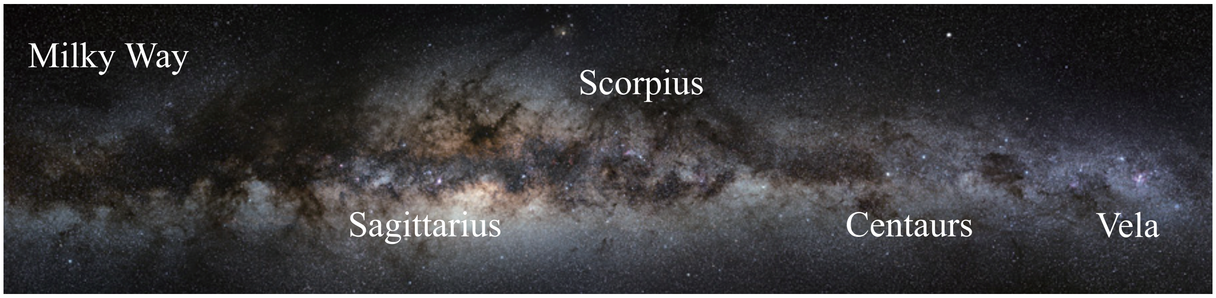

Fig. 2.1.—: Optical picture of the Milky Way galaxy (Laustsen et al. , 1987).

The Galaxy consists mostly of the stars, which dominate the entire galactic mass. The disk, including the bulge, contains ∼100 billion stars (corresponding to mass of $\sim 10^{11}$ $M_\odot$) with exponential spatial distribution dropping from the center. The scale length and height of the stellar-mass density are ∼3.5 kpc and ∼0.3 kpc, respectively. The bulge has ∼10 billion stars distributed in its bar potential. The stellar density is ∼1 star pc^{-3} near the center and ∼0.1 star pc^{-3} near the Sun.

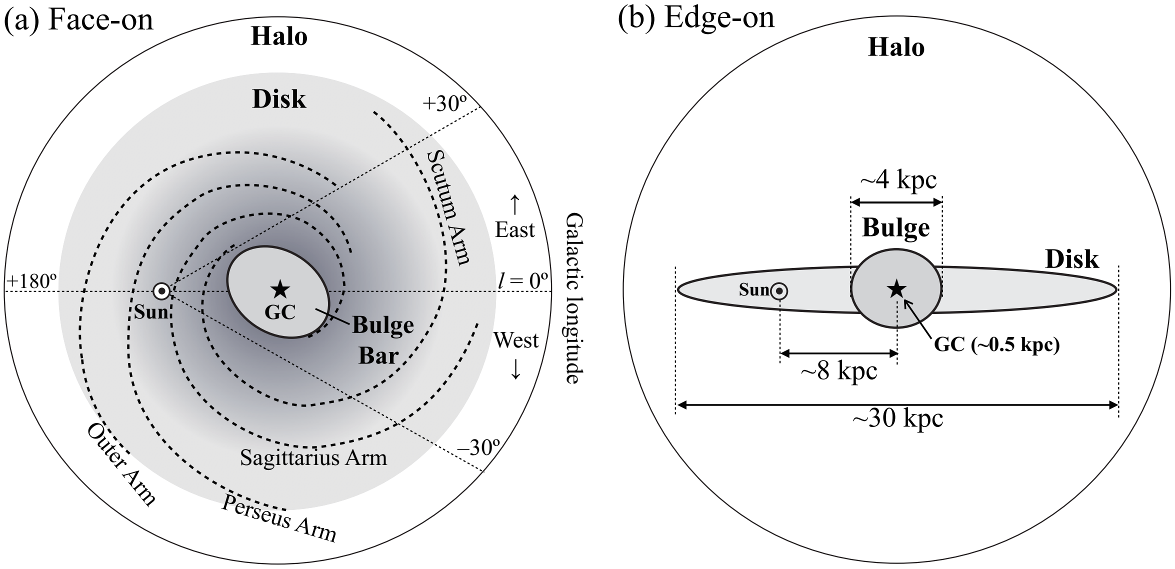

Fig. 2.2.—: Schematic global view of the Galaxy. (a) Face-on view. (b) Edge-on view.

Interstellar Medium

Between the stars is the interstellar medium (ISM), whose mass is ∼5% with respect to the stelar mass. The ISM mainly composed of the hydrogen (H I, H_2, and H II) gases and the dust. The component ratio between gas and dust is ∼100:1.

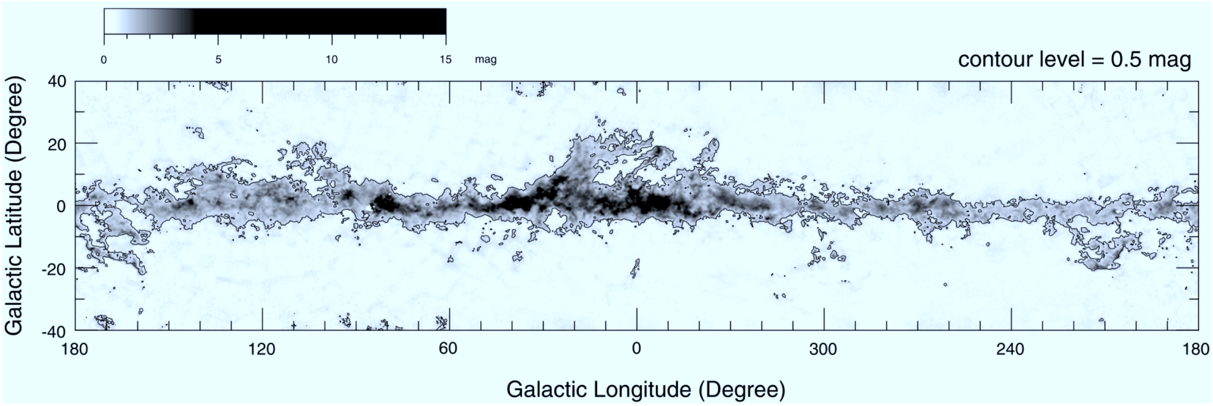

Fig. 2.3.—: Optical extinction (A_V)map of the Galaxy (Dobashi et al., 2005).

The ISM is concentrated on the disk, as observed in different wavelengths. One fundamental parameter is the equivalent hydrogen column density (N_H) along the line of sight. In the optical/infrared band, lights from stars are absorbed and scattered by the dust, which results in the interstellar extinction (figure 2.3; Dobashi et al. 2005). The measured extinction (A_V) can predict the N_H from the following relation (e.g., Güver & Özel 2009).

$$N_\mathrm{H}\ [\mathrm{cm}^{-2}] \;=\; 2.2\times10^{21}\ \ A_\mathrm{V}\ [\mathrm{mag}] \tag{2.1}$$

In the radio observations, H I line (21 cm) and molecular rotation transition lines are powerful tools to trace the neutral hydrogen atom and molecules (e.g., CO) in the ISM. The line intensity and its doppler shift tell the column density and the line-of-sight velocity (i.e., radial velocity) of the gas, respectively. For example, we show a CO map in figure 2.4a (Dame et al., 2001). The N_H of H I gas is expressed by integration of the observed line intensities along velocity ranges ($\int T\ dv$),

$$N_\mathrm{H\,I}\ [\mathrm{cm}^{-2}] \;=\; 1.8\times10^{18}\ \ \int T_{21\ \mathrm{cm}}\ dv\ [\mathrm{K\ km\ s}^{-1}] \tag{2.2}$$

where $T_{21\ \mathrm{cm}}$ is the intensity of the 21-cm line. The H_2 molecule is usually investigated indirectly from the coexisting molecules such as CO and CS; the N_H can be estimated as below.

$$N_{\mathrm{H}_2}\ [\mathrm{cm}^{-2}] \;=\; 0.7\times10^{20}\ \ \int T_\mathrm{CO}\ dv\ [\mathrm{K\ km\ s}^{-1}] \tag{2.3}$$

$$N_{\mathrm{H}_2}\ [\mathrm{cm}^{-2}] \;=\; 4\times10^{21}\ \ \int T_\mathrm{CS}\ dv\ [\mathrm{K\ km\ s}^{-1}] \tag{2.4}$$

where T_CO and T_CS is the intensity of the $^{12}\mathrm{C}^{18}\mathrm{O}$ ($J=1\rightarrow0$) line and the $^{12}\mathrm{C}\,^{32}\mathrm{S}$ ($J=1\rightarrow0$) line, respectively. The conversion factors ($[N_{\mathrm{H}_2}]/[\int T\ dv]$) are values reported by Torii et al. (2010) for the CO line and Tsuboi et al. (1999) for the CS line. Note that these parameters contain systematic uncertainties depending on the molecular composition (H, C, and O) ratio and the critical densities (i.e., optically thin or thick conditions). On the other hand, the X-ray absorption is a direct way to measure the N_H of the ISM, which is about $\sim6\times10^{22}$ H cm^{-2} between the Sun and the Galactic center (e.g., Sakano et al. 2002).

3 Dimensional Dynamics and Structure

The plot of radial velocity (V_LOS or V_LSR) against the Galactic longitude (l-V diagram) shows an inclined bar-like structure (figure 2.4b), which indicates that the entire Galaxy is rotating around the center basically in a circular motion, in spite of some local random motions. From the solar point of view, ISM on the east side ($l>0$) of the center is moving away ($V_\mathrm{LOS}>0$) while ISM of the west side is moving toward. The rotation velocity near the solar system (LSR; local standard of rest) is $V_0\approx220$ km s^{-1}, at distance of R_0=8 kpc from the GC (e.g., Yusef-Zadeh et al. 1999).

The 3 dimensional (line-of-side) distribution of the Galactic ISM is a basic and very curious topic, but is not available for direct observation because we are located inside the

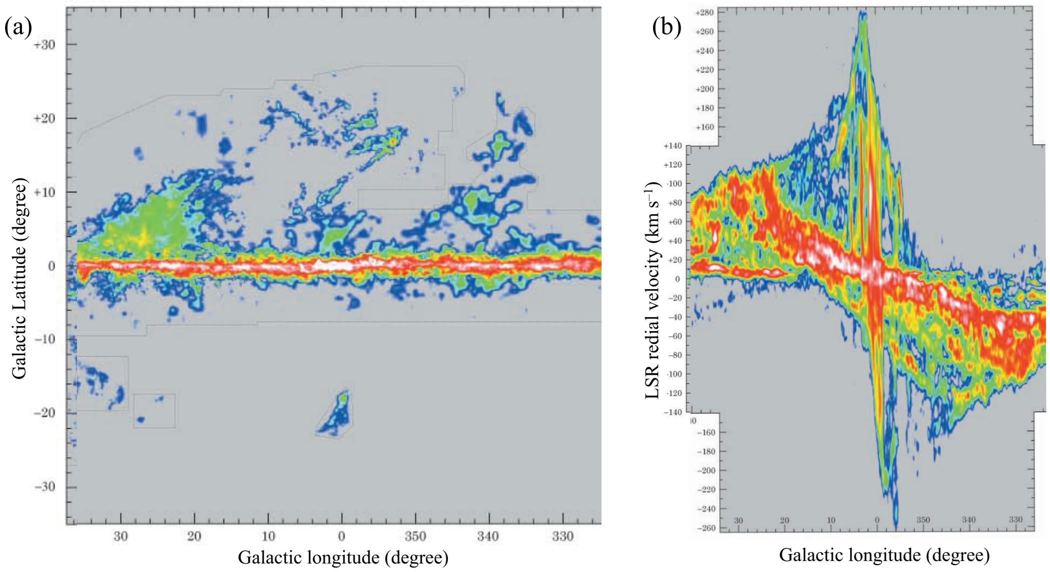

Fig. 2.4.—: Radio CO (1–0) map of the Galaxy (Dame et al., 2001). (a) Spatial distribution on the Galactic Plane. (b) Velocity distribution along the longitude (l-V diagram).

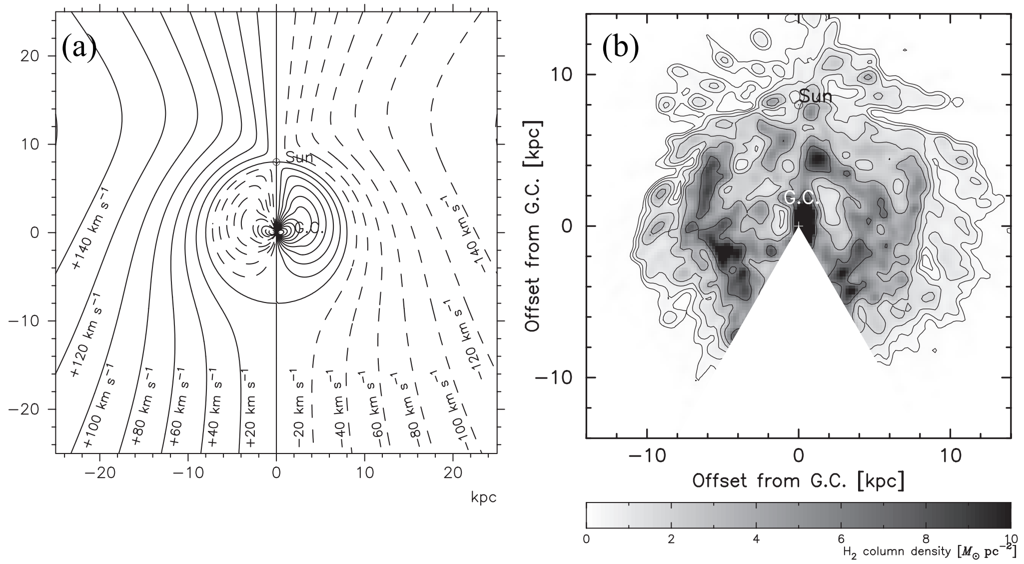

Fig. 2.5.—: (a) Radial velocity field on the Galactic plane calculated with the rotation curve (Nakanishi & Sofue, 2003). (b) Face-on map of molecular (H_2) gas in the Galaxy (Nakanishi & Sofue, 2006).

Galaxy. Assuming that the motion of the Galactic ISM is purely circular, the distance from the Galactic center (R) is a function of the radial velocity (V) as below,

$$V_{\rm LOS}\ (l) = \left[\frac{R_0}{R}\ v(R) - V_0\right]\ \sin(l) \tag{2.5}$$

where $v(R)$ is the known rotation curve (e.g., Clemens 1985; Dehnen & Binney 1998). By the de-convolution of the observed l-V diagram, Nakanishi & Sofue (2006) investigated the face-on view of ISM in the Galaxy (see figure 2.5).

2.1.2 Central Molecular Zone

The GC region is in complex with many molecular clouds (MCs), emission nebulae ($\rm H_{II}$ regions), supernova remnants (SNR), non-thermal radio emissions, and so on. The main component is the central molecular zone (CMZ, $|l| \lesssim 1.5°$; Morris & Serabyn 1996) which contains molecular mass of $\sim 3 \times 10^7$ $\rm M_\odot$ (Dahmen et al. 1998), approximately corresponds to 10% of the whole molecular gas in the Galaxy. Sagittarius (Sgr) B, Sgr A and Sgr C are the most well-known and massive MCs in the CMZ (see figure 2.6). The gas temperature and density of MCs in the CMZ are typically ∼70 K (ranges from 30 to 200 K) and $\geq 10^3$ $\rm cm^{-3}$, respectively.

The 3D structure of the CMZ has been studied mainly by the radio observations. Using l-V diagrams of the CO and CS lines and based on the assumption of the circular motions of the GC region, Sofue (1995) and Tsuboi et al. (1999) predicted the line-of-sight distribution of MCs. On the other hand, Sawada et al. (2004) examined the spatial correlation between 2.6-mm CO line and 18-cm OH absorption line, and investigated the overview of face-on distribution of MCs without assumption of dynamical motions. However, these results were not conclusive and could not reach a consistent view of the CMZ (c.f., figure 2.6b).

2.2 Super Massive Black Hole, Sagittarius (Sgr) A*

2.2.1 Presence and Basic Properties

It is now widely recognized that every galaxy harbors a super massive black hole (SMBH) at the center. The mass of the SMBHs shows extensive correlation with the mass of the bulge, with a ratio of $M_{\rm bh}/M_{\rm bugle} \sim 10^{-3}$ (figure 2.8; e.g., Magorrian et al. 1998). This suggests interaction and co-revolution of the SMBH and the bulge in galaxies. The mass of our Galactic bulge ($\sim 10^{10}$ $\rm M_\odot$) predicts a SMBH existence with mass of $\sim 10^7$ $\rm M_\odot$ at the GC.

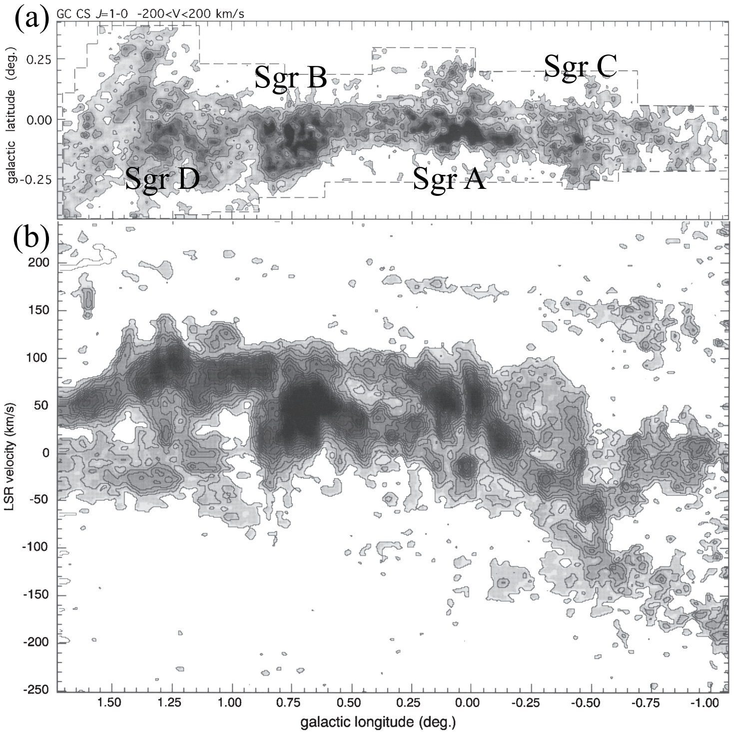

Fig. 2.6.—: Radio CS (1–0) map of the central molecular zone (Tsuboi et al., 1999). (a) Spatial distribution on the Galactic Plane. (b) Velocity distribution along the longitude (l-V diagram).

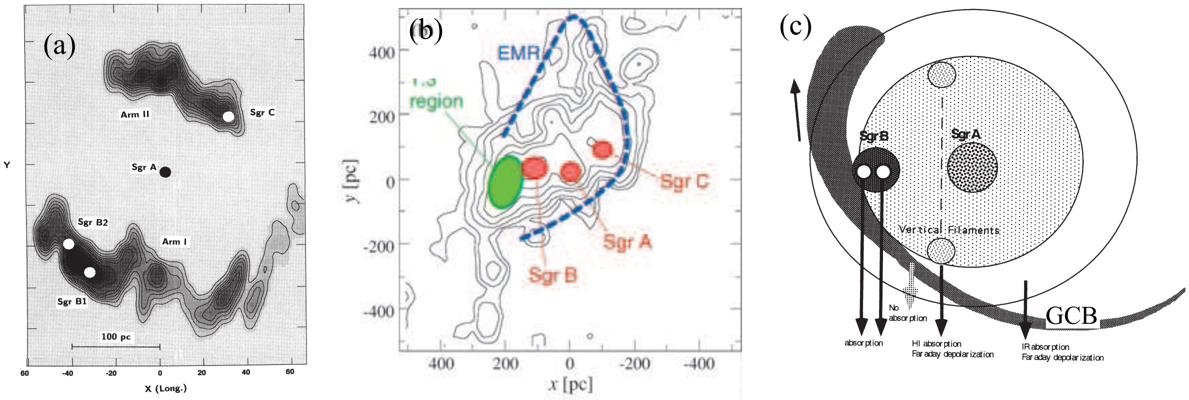

Fig. 2.7.—: Different predictions on the face-on view of the central molecular zone. (a) Sofue (1995). (b) Sawada et al. (2004). EMR represents the "expanding molecular ring". (c) Tsuboi et al. (1999). GCB represents the "Galactic center bow".

The SMBH of the Galaxy was early noticed at the continuum radio band as a very

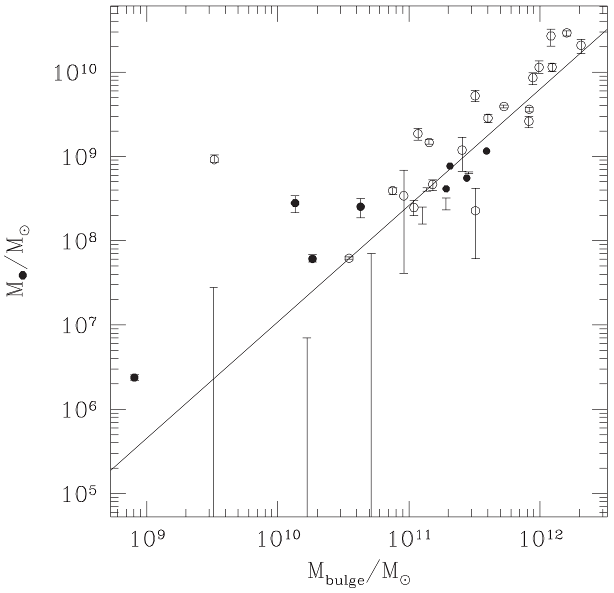

Fig. 2.8.—: Mass correlation between the super mass black hole and its host bulge (Magorrian et al., 1998).

compact point source inside the Sgr A complex of ∼10 pc (see figure 2.10a), which coincides with the dynamical center of the Galaxy. The SMBH is thereafter named Sgr A* and the existence becomes conclusive after infrared observations of the proper motions of stars (S stars) within the central region of $\sim 1'' \times 1''$ (figure 2.9; e.g., Ghez et al. 2005). From the astrometric and radial velocities (Keplerian orbits) of the S stars , the distance to and the mass of Sgr A* is well determined to be $R_0 = 8.0 \pm 0.6$ kpc and $M_{\rm bh*} = 4.1 \pm 0.6 \times 10^6$ $M_{\odot}$, respectively (Ghez et al., 2008). The Galactic location of Sgr A* is measured to be at $l = -0.^{\circ}056$ and $b = -0.^{\circ}046$, by radio VLA observations (Yusef-Zadeh et al., 1999).

2.2.2 X-ray Observations of Sgr A*

After the establishment of presence of the nearest SMBH, Sgr A* is considered as one of the most precious samples to study the high-energy phenomena of SMBH and its surrounding environment. Many X-ray observations have been carried out at the GC region. Started with the Einstein Observatory (Watson et al., 1981), ROSAT (Predehl & Truemper, 1994), BeppoSAX (Sidoli et al., 1999), and ASCA (Koyama et al., 1996) have detected X-rays in 0.5–10 keV from the inner region of $\sim 0.^{\circ}5$ near the radio position of Sgr A*. From these observations, the X-ray absorption was measured to be $N_{\rm H} \approx 5$–8×10^{22} H cm^{-2} with thermal bremsstrahlung model of $k_{\rm B}T \approx 5$ keV. Then, the un-absorbed X-ray luminosity in 2–10 keV

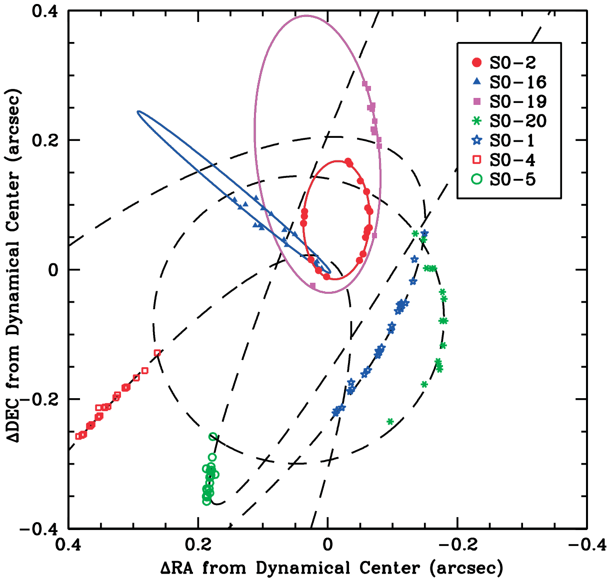

Fig. 2.9.—: Proper motions of S stars around SMBH, Sgr A* (Ghez et al., 2005).

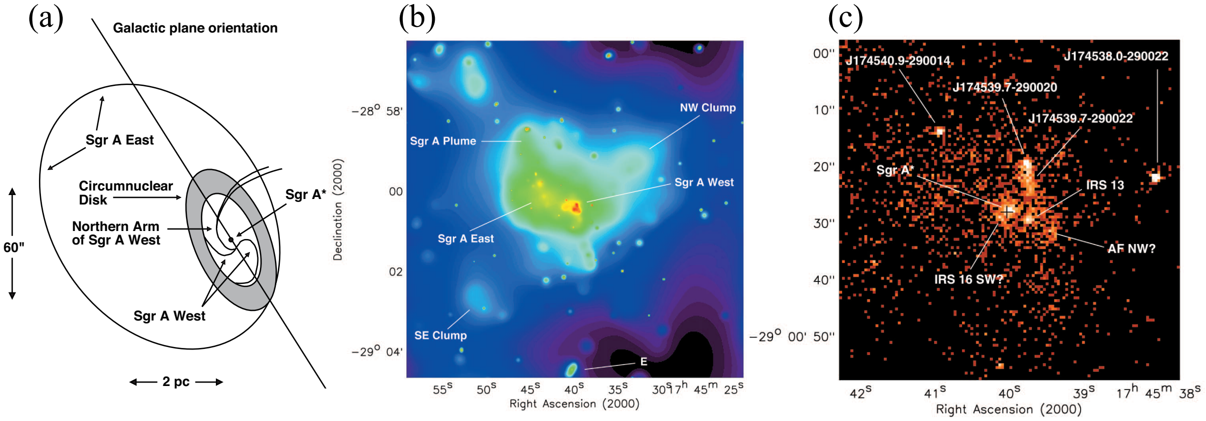

Fig. 2.10.—: X-ray Image of the vicinity of Sgr A* by Chandra (Baganoff et al., 2003). (a) Schematic view of the main constituents of the Sgr A radio complex. (b) X-ray (0.5–7 keV) image of the central $8.'4\times8.'4$ region around Sgr A*. (c) same as (b) but of the central $1'\times1'$ region.

was estimated to be $L_{\rm X}\leq 10^{35}$–10^{36} erg s^{-1}, as the upper limit of Sgr A* because of these observations could not exclude contaminations from nearby sources. In the hard X-ray observations (e.g., Spartan-1, Kawai et al. 1988; Granat, Sunyaev et al. 1993), the presence of a long-term variable source near the position of Sgr A* was suggested and the average 4–20 keV luminosity was reported to be $L_{\rm X}\sim 10^{36}$ erg s^{-1}.

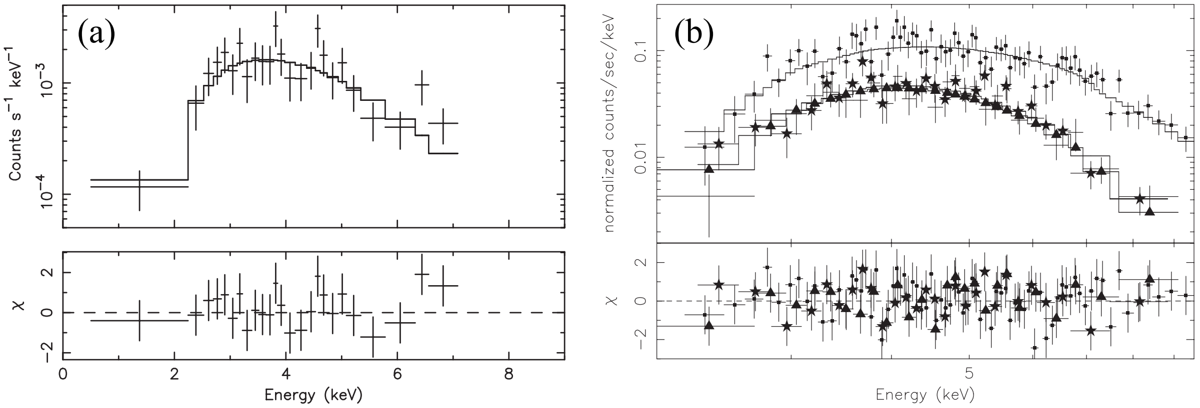

Fig. 2.11.—: X-ray spectra of Sgr A* and fitting with absorbed power-law models. (a) Spectrum from the inner 1.″5 radius circle by Chandra (Baganoff et al., 2003). (b) Spectrum from the inner 10″ radius circle by XMM-Newton (Porquet et al., 2003).

The Chandra X-ray observatory (c.f., Weisskopf et al. 1996), with the unprecedented high-angular resolution of ∼0.″5, resolved the individual sources inside the inner 1′×1′ region. Baganoff et al. (2003) identified X-rays from the radio position of Sgr A* within ∼0.″3, the probability of a false match was estimated to be less than 0.5%. The direct observation of Sgr A* allowed them to extract the pure spectrum without large contamination from nearby sources. The Sgr A* spectrum was well explained by an absorbed power-law model with large $N_{\rm H}= 9.8^{+4.4}_{-3.0}\times10^{22}$ H cm^{-2} and $\Gamma = 2.7^{+1.3}_{-0.9}$ (see figure 2.11a). The X-ray luminosity of Sgr A* in 2–10 keV was $L_{\rm X}$=$2.4^{+3.0}_{-0.6}\times10^{33}$ erg s^{-1} in the quiescent phase.

Short X-ray flares have been found from Sgr A*. Baganoff et al. (2001) reported the first flare detection in 2000 October, with duration of ∼10 ks and $L_{\rm X}$=$1.0^{+0.1}_{-0.1}\times10^{35}$ erg s^{-1}, which is about 45 times brighter than that in the quiescent phase. The biggest flare so far was detected by XMM-Newton in 2002 October (Porquet et al., 2003), which exhibited a duration of ∼2.7 ks and $L_{\rm X}$ of $3.6^{+0.3}_{-0.4}\times10^{35}$ erg s^{-1}, i.e., an increase by a factor of ∼160. The photon index of Sgr A* spectrum varies in different flares, which was $\Gamma = 1.3^{+0.5}_{-0.6}$ in 2000 and $\Gamma = 2.5^{+0.3}_{-0.3}$ in 2002.

As reviewed above, direct X-ray observations toward Sgr A* over the past two decades have shown that the present luminosity is in range of $L_{\rm X}$∼10^{33}–10^{35} erg s^{-1}, which is extremely low. The bolometric luminosity of a $\sim 4\times10^{6}\ M_{\odot}$ SMBH (Sgr A*) radiating at the Eddington rate[1] is $L_{\rm Edd} = 5\times10^{44}$ erg s^{-1}. Therefore, at present, Sgr A* is about 9–11 orders of magnitude fainter than its Eddington limit ($\sim 10^{-11}L_{\rm Edd}$), i.e., the quiescent/off state.

---

[1] Maximum luminosity of the source where the radiation force outwards equals to the gravitational force inwards: $L_{\rm Edd} = 4\pi G M_{\rm bh} m_{\rm p} c/\sigma_{\rm T} = 1.26\times(M_{\rm bh}/M_{\odot})\ 10^{38}$ erg s^{-1}.

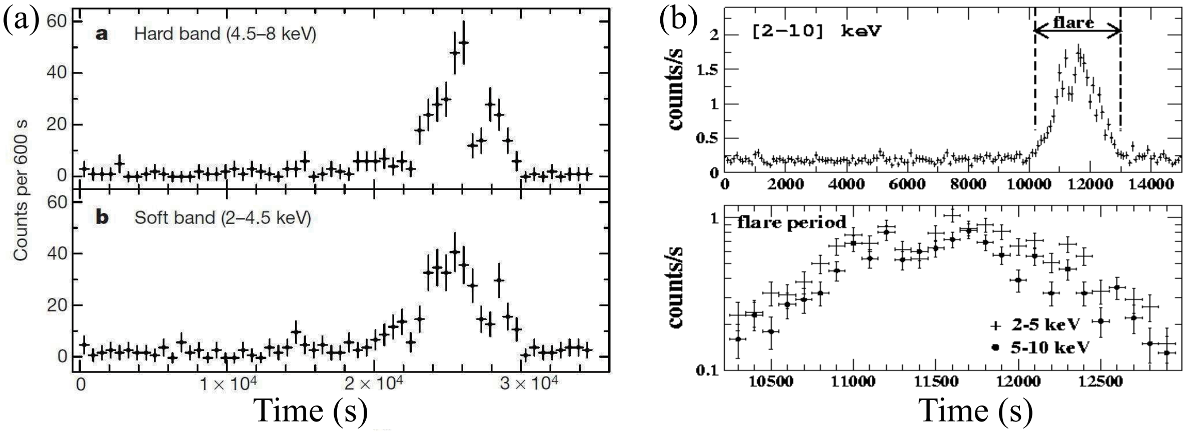

Fig. 2.12.—: Short X-ray flares of Sgr A*. (a) Flare detected in 2000 October by Chandra (Baganoff et al., 2001). (b) Flare detected in 2002 October by XMM-Newton (Porquet et al., 2003).

The present Sgr A* luminosity is even about 6 orders of magnitude lower than the luminosities of other 10^{6-7}-$M_{\odot}$ class SMBHs sitting in nearby spiral galaxies, which emit X-rays at $L_{\rm X}\sim 10^{39}$–10^{40} erg s^{-1} or $\sim 10^{-6} L_{\rm Edd}$ (e.g., M 81, Ishisaki et al. 1996; M 51, Terashima & Wilson 2001). These SMBHs are classified as the low-luminosity active galactic nucleus (LLAGN), which are described by the model of advection-dominated accretion flow (ADAF; c.f., Narayan 2005 and references therein). X-ray emission from LLAGN is dominated by thermal Comptonization of hot electrons ($k_{\rm B}T\sim$100 keV) in optically-thin ADAF gas, which is distinct from the black-body radiation (optically thick) in the standard thin accretion disk model (Shakura & Sunyaev 1973).

On the other hand, as indirect observation of Sgr A*, X-ray reflections are found from giant molecular clouds around Sgr A* and are proposed as echoes of its flares with $L_{\rm X}\sim 10^{39}$ erg s^{-1} occurred in the past (e.g., Koyama et al. 1996). Details will be reviewed in section 2.4.

2.3 Thermal X-rays from the Galactic Center

2.3.1 Early X-ray Observations on the Galactic Plane

Point Sources

X-ray observations on the Galactic plane and central region have found many bright point sources, most of which are X-ray binaries related to white dwarfs, neutron stars, and black holes (e.g., Watson et al. 1981; Kawai et al. 1988; Sakano et al. 2002). The point sources typically show spectra explained by power-law model with photon index of $\Gamma = 2$–3 or featureless thermal bremsstrahlung model with $k_{\mathrm{B}}T$ of ~10 keV. The X-ray (2–10 keV) luminosities of these individual objects are in range from 10^{35} to 10^{37} erg s^{-1}.

Diffuse X-rays

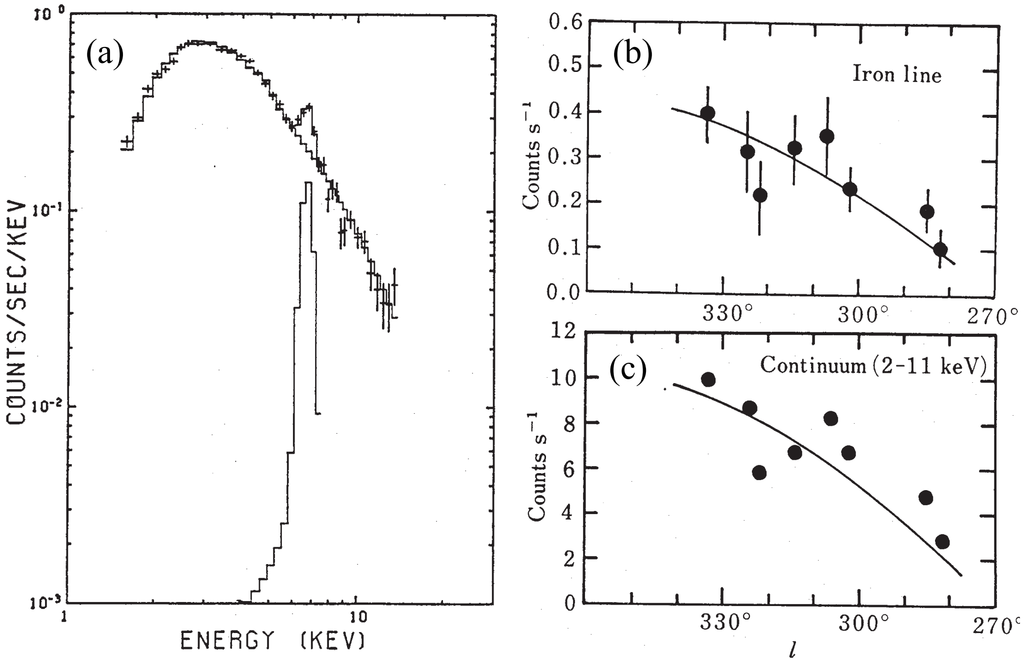

Fig. 2.13.—: X-ray observation of the Galactic ridge by the Tenma satellite (Koyama et al., 1986). (a) X-ray spectrum of the Galactic ridge and the detection of the 6.7 keV line. (b) Galactic distribution of the 6.7 keV line. (c) Galactic distribution of the continuum.

Beside the numerous discrete sources, diffuse X-ray emissions (>2 keV) were found to

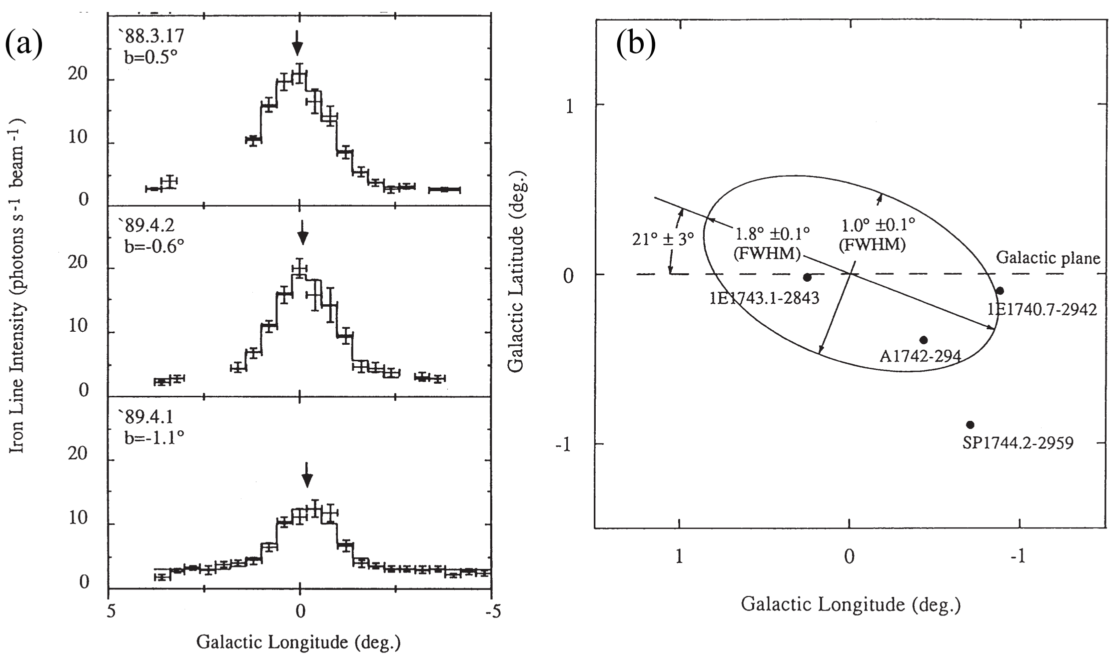

Fig. 2.14.—: X-ray observation of the Galactic center by the Ginga satellite (Yamauchi et al., 1990). (a) Galactic distribution of the 6.7 keV line intensity. (b) Interpretation of the 6.7 keV Galactic distribution as two-dimensional gaussian.

widely extend from either side of the GC out to the Galactic ridge for several kpc (tens of degree) in longitude (e.g., Iwan et al. 1982; Worrall et al. 1982; Warwick et al. 1985; Bleach et al. 1972). This large-scale emission is called the Galactic ridge X-ray emission (GRXE). From improved spectra observed with the Tenma satellite, Koyama et al. (1986) and Koyama (1989) discovered thermal emissions with intense 6.7 keV (He-like, Fe XXV) iron line from the ridge region at $l \sim 270°$–$330°$ (see figure 2.13a). The GRXE spectra were described with optically-thin plasma model with hot temperature of $k_{\rm B}T$ = 5–10 keV.

Subsequently with the Ginga satellite, Yamauchi et al. (1990) performed the 6.7 keV emission-line mapping around the GC, and reported the intense elliptical distribution within the inner $\sim$2° (figure 2.14) region. The line intensity at the GC is about 10 times larger than that from the Galactic ridge (Koyama et al., 1989); this excess can be referred to as the Galactic center diffuse X-rays (GCDX). The 6.7 keV emission from highly-ionized iron implies the existence of hot plasma with $k_{\rm B}T$ of $\sim$ 10 keV concentrated in the GC region.

The next breakthrough is by the ASCA satellite which firstly introduced the photon counting type of X-ray CCDs (Burke et al., 2001; Koyama et al., 2007a) for the high-resolution imaging spectroscopy. From observations of the GCDX from the Sgr A and

Sgr B regions, Koyama et al. (1996) revealed a fact that the iron line at ∼6.7 keV is a complex of three lines: the 6.7 keV (Fe XXV), the 6.9 keV (Fe XXVI), and the 6.4 keV (Fe I) lines (see figure 2.15). The 6.7 keV and 6.9 keV lines are thermal X-rays from ionized iron atoms (Galactic center plasma emission), while the 6.4 keV line is emitted from neutral iron atoms by non-thermal processes. These two emissions have completely different origins and physics behind, hence, we explain them separately in the remaining parts of section 2.3 and section 2.4.

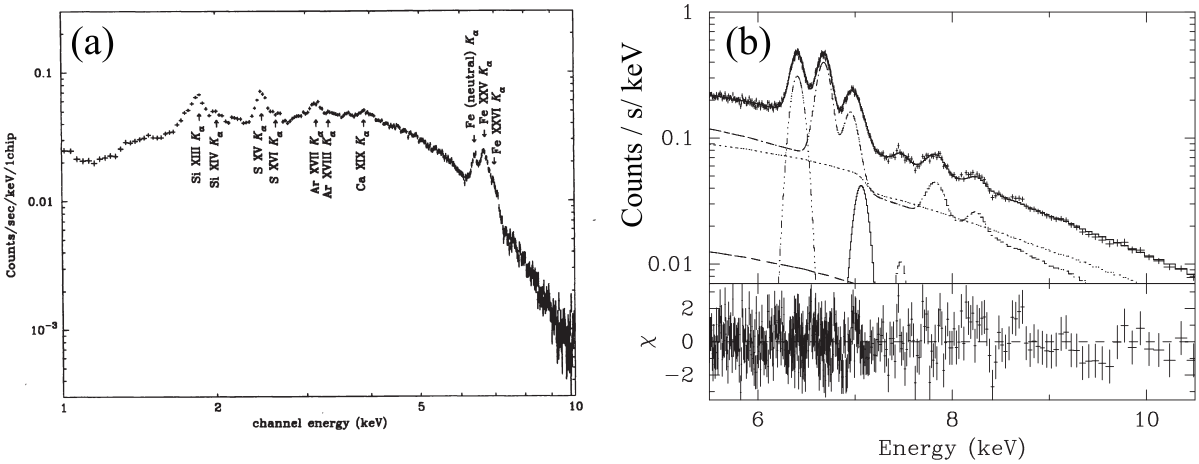

Fig. 2.15.—: (a) X-ray spectra of the GC region by CCDs onboard ASCA (Koyama et al., 1996). (b) same as (a) but by CCDs onboard Suzaku (Koyama et al., 2007c).

2.3.2 The Fe XXV Kα (6.7 keV) Diffuse Emission and the GC Hot Plasma

The prominent feature of the GCDX spectrum (see figure 2.15) is strong K-shell emission lines from highly ionized atoms, such as Fe XXV (6.7 keV) and Fe XXVI (6.97 keV). Two physical processes have been considered for 6.7 keV and 6.9 keV lines: the collision excitation (CE) and re-emission in an optically thin and high-temperature plasma, or the charge exchange (CX) recombination during a collision between neutral hydrogen and ionized irons produced by cosmic-rays (e.g., Tanaka et al. 2000). The 6.7 keV line is mainly composed of the forbidden line (6636 eV) and the resonance line (6700 eV). The CX process produces stronger forbidden line than the resonance line (Otranto et al. 2006) and therefore a line center near 6636 eV, while the resonance line is stronger in the CE case and therefore a line center near 6700 eV (c.f., Koyama et al. 2007c and references therein).

Using the Suzaku satellite, Koyama et al. (2007c) made careful energy measurements of the 6.7 keV and 6.9 keV lines with deep exposure of ~200 ks near the Sgr A region (figure 2.15b). The line center at 6.7 keV at was well determined to be 6680±1 eV, which favors the CE process in plasma. Moreover, the line-intensity ratios of Fe XXVI Kα (6.97 keV)/Fe XXV Kα (6.7 keV) and Fe XXV Kβ (7.88 keV)/Fe XXV Kα (6.7 keV) are about 0.33 and 0.09, respectively. These values indicate that the plasma is in a collisional ionization equilibrium (CIE) at the temperature of $k_{\rm B}T = 6.5 \pm 0.1$ keV. The iron abundance of the plasma was determined to be $Z_{\rm Fe}/Z_{\odot} \approx 1$. In conclusion, the 6.7 keV emission of the GCDX is produced during processes in a hot plasma of 7×10^{7} K; we can called it the Galactic center plasma emission (GCPE), hereafter.

Koyama et al. (1996) made rough estimation for the physical parameters, and then raised the question on the origin of the GC hot plasma. Adopting a temperature of $k_{\rm B}T\approx10$ keV and a size of ~1° (i.e., 140 pc at 8 kpc), the electron (ion) density is ~1 cm^{-3} and the total thermal energy of the plasma is $E_{\rm plasma}\sim 10^{53}$–$10^{54}$ erg. With the sound velocity of 1600 km s^{-1} (at $k_{\rm B}T$=10 keV), the time scale for the plasma to expand over 140 pc is $\tau_{\rm plasma} \sim 10^{5}$ years. The thermal temperature ($k_{\rm B}T\sim$10 keV) is larger than the energy of Galactic gravity; the rotation velocity of molecular gases induced from the gravity potential is only ≤ 250 km s^{-1} (figure 2.6) compared to the sound velocity of the hot plasma. Hence, the plasma would have escaped from the GC region if there were not an huge energy supply. The required energy rate is about $E_{\rm plasma}/\tau_{\rm plasma} \sim 10^{41}$–$10^{42}$ erg s^{-1}. As a candidate for the energy origin, one supernova (SN) event every 100–1000 years (i.e., 10^{-2}–10^{-3} SN yr^{-1}) within the vicinity of GC can somehow explain that energy rate numerically. However, the supernova origin seems to be unrealistic because the supernova rate in the GC ($\sim 10^{-4}$ SN yr^{-1}; estimation from Uchiyama et al. 2012, Diehl et al. 2006, and references therein) is much lower than the above expectation and the reported temperatures of the GC SNRs ($k_{\rm B}T\sim$1 keV; e.g., Nobukawa et al. 2008; Tsuru et al. 2009; Mori et al. 2008; Sawada et al. 2009) are also difficult to explain that of the GC plasma ($k_{\rm B}T\approx$6.5 keV). Still, the energy origin of the GC hot plasma is a mystery if it is truly diffuse.

2.3.3 The S XV Kα (2.45 keV) Diffuse Emission and Possible Presence of Large-scale Low-temperature Plasma

Beside the iron lines, the GCDX spectrum (c.f., figure 2.15a) also displays strong line emission of ionized sulfur at 2.45 keV (S XV Kα). The 2.45 keV line is mainly produced from a plasma with lower temperature of kT ~1 keV (compared with $k_{\rm B}T\approx$6.5 keV of the hot plasma represented by the 6.7 keV line), which is close to the temperature of many SNR candidates found in the GC region (e.g., Nobukawa et al. 2008; Tsuru et al. 2009; Mori et al. 2008). Interestingly, similar to the 6.7 keV emission, the diffuse 2.45 keV emission is present even in the absence of local sources such as SNRs. The 2.45 keV emission probably originates from another large-scale plasma with $k_{\rm B}T{\sim}1$ keV. However, the 2–3 keV band is sensitive to X-ray absorption with $N_{\rm H}{\sim}\,10{\times}10^{22}$ H cm^{-2} from the CMZ (section 2.1.2), which makes the investigation of the 2.45 keV line difficult. The properties of the low-temperature plasma, temperature and relation with the high-temperature (6.5 keV) plasma, are still not clear.

2.3.4 Latest Results

Spatial Distribution of the Emission Lines from the GC to the GR

The 6.7 keV emission is known to spread over the GC region for about 1° with a monotonic decrease as the distance from Sgr A* increases (Koyama et al. 1989; Yamauchi et al. 1990). Recently, with Suzaku, Uchiyama et al. (2011) performed an intensive investigation on the 6.7 keV (Fe XXV Kα) line profile for the whole GC region ($\sim 5^\circ \times 2^\circ$; see figure 2.16), then Uchiyama et al. (2012) extended the work to the other emission lines of highly ionized sulfur (S), argon (Ar), and calcium (Ca). As shown in figure 2.17, these works quantitatively determined the spatial (l) distributions of plasma emissions from the GC to the Galactic ridge (GR). The e-folding lengths of the GC and GR components are measured to be $l_{\rm GC} \approx 0.6^\circ$ and $l_{\rm GR} \approx 50^\circ$, respectively.

Origins as the Source of Thermal Emissions from the GC and the GR

After the discovery of the 6.7 keV and other thermal emissions from the Galactic plane (GR and GC), two origins have been proposed as the source: a large-scale hot plasma of truly diffuse gases or a superposition of unresolved pointed sources.

In a region at $(l,\ b)=(0.^\circ1,\ -1.^\circ4)$, Revnivtsev et al. (2009) resolved more than 80% of the 6.7 keV flux into point sources, with the high-angular-resolution and deep-exposure observation by Chandra. Prime candidates of these point sources are cataclysmic variables (CVs) and active binaries (ABs), whose spectra display irons lines (6.4, 6.7, and 6.9 keV) and indicate high temperature of $k_{\rm B}T{\sim}\,10$ keV (e.g., Ezuka & Ishida 1999; Ishida et al. 2009; Yuasa et al. 2010). Despite some discrepancies of the observed iron-line equivalent width between CVs/ABs ($EW_{6.7\ \rm keV} \sim 200$ eV) and the GR ($EW_{6.7\ \rm keV} \sim 500$ eV; e.g., Uchiyama et al. 2012; Yamauchi et al. 2009), an assembly of numerous discrete faint X-ray stars are presently proposed as the main origin of the GR emission (Revnivtsev et al. 2009; Yuasa et al. 2012).

On the other hand, in the GC region, the 6.7 keV profile demonstrates the excess of $\sim$4 times over that of the stellar mass distribution (Uchiyama et al., 2011). Also from the study of equivalent width of the 6.4 keV and 6.7 keV lines, the point-source contribution to

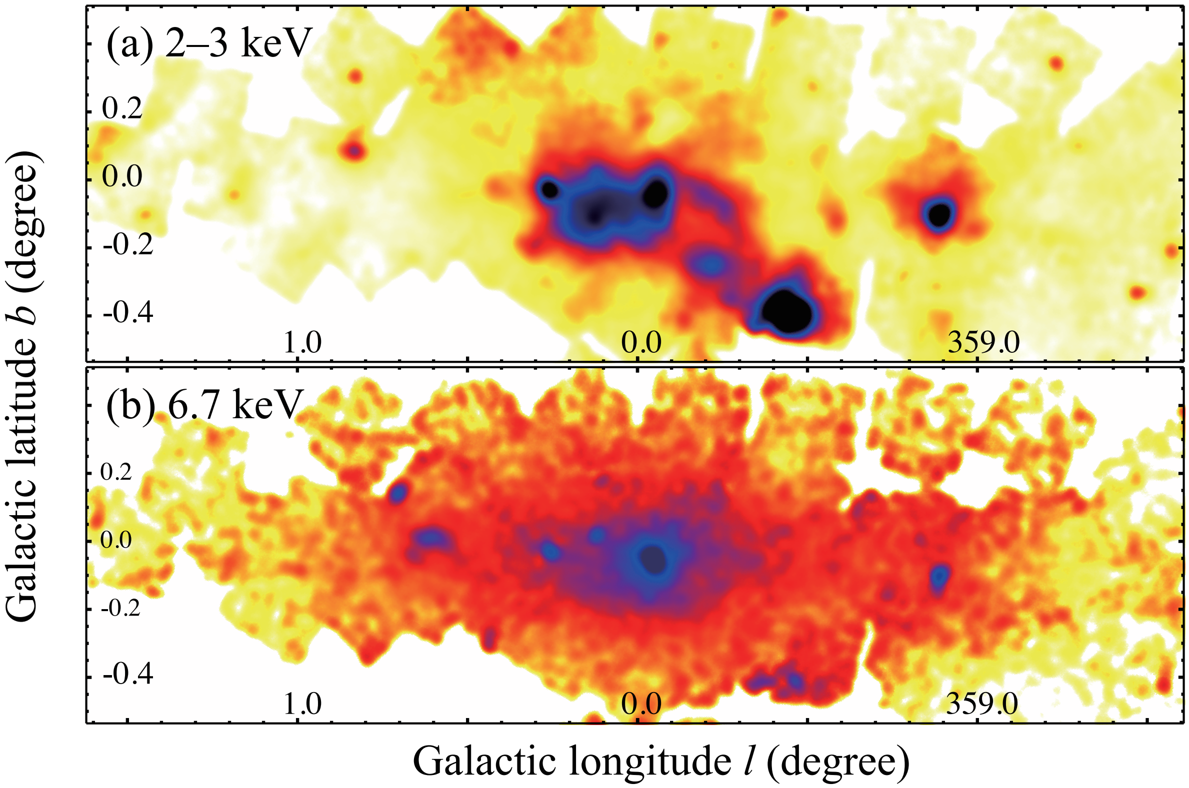

Fig. 2.16.—: X-ray band maps of the GC plasmas by Suzaku (constructed from Uchiyama et al. 2011, 2012). (a) The 6.7 keV (6.5–6.8 keV) band for Fe XXV Kα. (b) The 2–3 keV band for S XV Kα and continuum emission.

the 6.7 keV emission near Sgr A is ∼1/6, estimated by Koyama et al. (2008). These results confirmed the presence of large-scale diffuse thermal plasma as the dominating source of the 6.7 keV emission in the GC.

2.4 Fe I Kα Diffuse Emissions in the Galactic Center

2.4.1 The 6.4 keV Line and its Origins

The GCDX has another main component, non-thermal emissions of the 6.4 keV line from neutral irons (Fe I Kα) and the related continuum X-rays (i.e., 6.4 keV emissions). As shown in figure 2.18, the 6.4 keV line has been found from giant molecular clouds (MCs) such as Sagittarius (Sgr) B, Sgr A, and Sgr C (e.g., Koyama et al. 1996; Murakami et al.

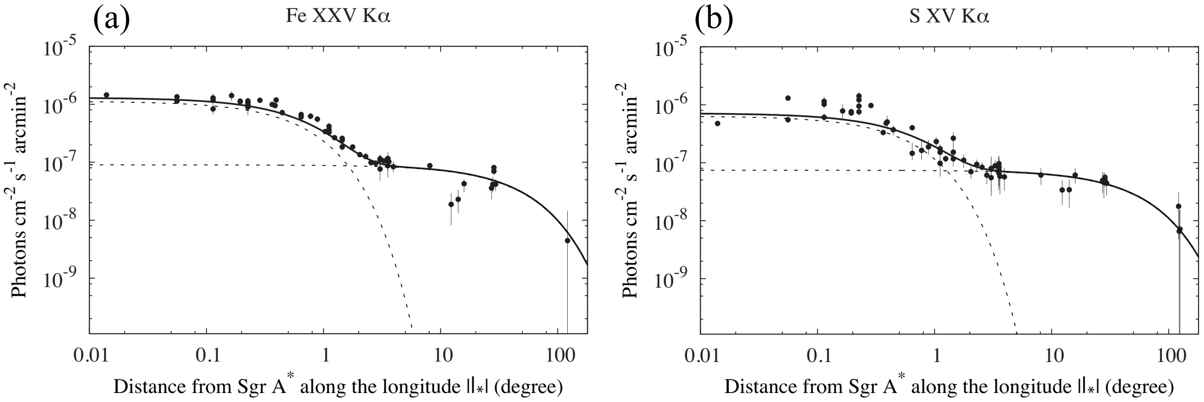

Fig. 2.17.—: Intensity profiles of the plasma emission lines from the GC by Suzaku (Uchiyama et al., 2012). (a) Profile for the 6.7 keV line (Fe XXV Kα). (b) Profile for the 2.45 keV line (S XV Kα).

2001; Park et al. 2004; Muno et al. 2007). Origins of X-ray and sub-relativistic charged particles (electron or proton) have been proposed for producing the 6.4 keV emissions.

X-ray Origin

The 6.4 keV line and the related continuum emission are respectively due to fluorescence and Thomson scattering taking place inside a MC, as consequences of irradiation by external X-rays. For the fluorescence line, the injecting photons have to be harder than $E \geq$7.1 keV, i.e., iron absorption edge, to generate an electron vacancy in the K-shell. Then the characteristic X-rays are re-emitted isotropically. Assuming an power-law model with photon index of Γ= 1.5 for the irradiating X-ray source, the resultant 6.4 keV flux ($F^{\rm X}_{6.4}$) can be approximated to the following form (c.f., Sunyaev & Churazov 1998; Capelli et al. 2012).

$$F^{\rm X}_{6.4} \approx 1.2\times\ Z_{\rm Fe}\ \frac{\Omega}{4\pi R^2_{\rm GC}}\ \tau_{\rm T}\ I_{8\ \rm keV}\ \ [\text{photon cm}^{-2}\ \text{s}^{-1}] \tag{2.6}$$

Here Ω is the solid angle of the target cloud (with projected area S) seen from the illuminating source (at distance D), i.e., $\Omega \approx S/D^2$. The other parameters of $R_{\rm GC}$, $Z_{\rm Fe}$, $\tau_{\rm T}$, and $I_{8\ \rm keV}$ are the distance to the GC, the iron abundance w.r.t solar, optical depth due to Thomson scattering, and the source flux at 8 keV (in unit of photon s^{-1}keV^{-1}). On the other hand, the continuum emission depends on the angle of Thomson scattering (θ); its flux at 6.4 keV ($C_{6.4}$) is written in the following approximate expression.

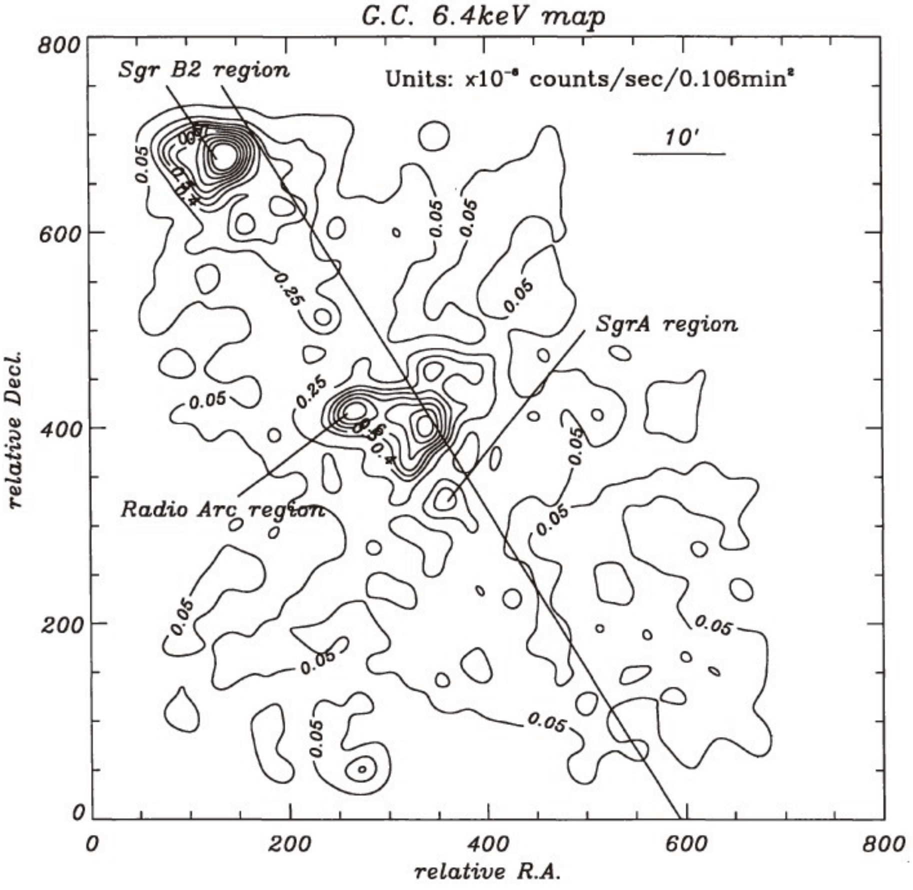

Fig. 2.18.—: Intensity distribution of the 6.4 keV emission in the GC by ASCA (Koyama et al., 1996).

$$C_{6.4} \approx 1.17 \times (1+\cos^2(\theta)) \frac{\Omega}{4\pi R_{\rm GC}^2} \;\; \tau_{\rm T} \; I_{8~\rm keV} \;\; [\text{photon cm}^{-2}\ \text{s}^{-1}\ \text{keV}^{-1}] \qquad (2.7)$$

Then, the equivalent width of the 6.4 keV line ($EW_{6.4~\rm keV}$), defined as $F^{\rm X}_{6.4}/C_{6.4}$, is expressed in following equation.

$$EW^{\rm X}_{6.4~\rm keV} \approx \frac{1.0 \times Z_{\rm Fe}}{1+\cos^2(\theta)} \;\; [\text{keV}] \qquad (2.8)$$

Considering the uncertainty of $Z_{\rm Fe}$ near GC (∼1–2 solar; e.g., Koyama et al. 2007c; Nobukawa et al. 2010) and the range of $\cos\theta$ (i.e., 0–1), $EW_{6.4~\rm keV}$ in X-ray origin should be larger than ∼0.5 keV. In addition, strong absorption features in the spectrum, bending continuum shape below 5 keV and iron absorption edge at 7.1 keV, are also expected because X-ray interactions occur deep inside the MCs (c.f., $N_{\rm H}$ for $\tau_{\rm T} = 0.1 - 1$ is $10^{23} - 10^{24}$ H cm^{-2}).

Electron Origin

Another possible process to produce the 6.4 keV line is the electron ($E \sim 100$ keV) impact on the MCs. Many synchrotron-emitting radio filaments have been found from the GC region (e.g., LaRosa et al. 2000; Law et al. 2008), which suggests the presence of electrons up to ~ 100 keV. In contrast to the X-ray origin, the electron-MC impact process produces weak 6.4 keV feature with $EW_{6.4\ \mathrm{keV}}$ of (250–300)$\times Z_{\mathrm{Fe}}$ eV (e.g., Yusef-Zadeh et al. 2007; Tatischeff 2003). Since electron with energies below ~100 keV would be stopped at surface of MCs with $N_{\mathrm{H}} \sim 0.4 \times 10^{22}$ H cm^{-2} (Tatischeff 2003), the 6.4 keV flux is expressed by the energy density of the injecting electron (U). The 6.4 keV intensity (surface brightness) can be approximated as below (Yusef-Zadeh et al. 2007 and references therein).

$$I_{6.4\ \mathrm{keV}}^{\mathrm{Electron}} \approx 4 \times 10^{-7}\ Z_{\mathrm{Fe}}\ (\frac{U}{100\ \mathrm{eV\ cm^{-3}}})\ [\mathrm{photon\ cm^{-2}\ s^{-1}\ arcmin^{-2}}] \qquad (2.9)$$

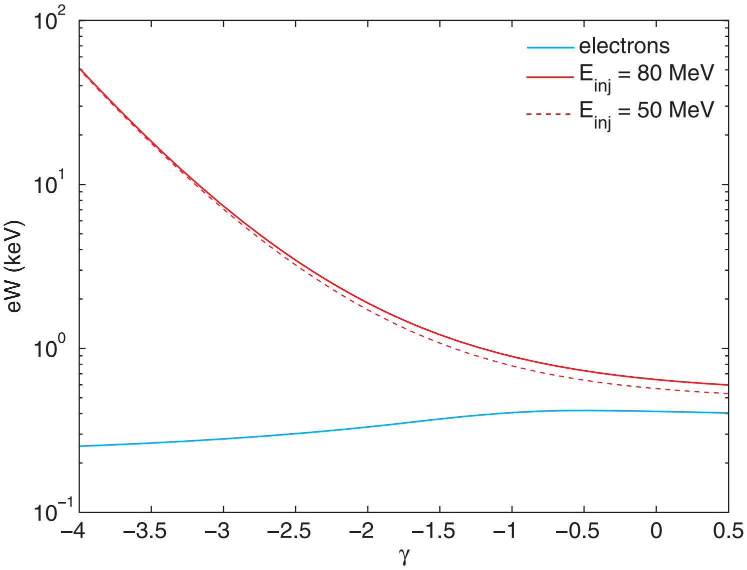

Fig. 2.19.—: Equivalent width of the 6.4 keV line produced by protons and electrons, for the solar abundance of iron (Dogiel et al., 2011). The horizontal axis shows the range of γ, which is the proton/electron index of injecting source assuming power-law spectrum ($N \propto E^{\gamma}$). E_{inj} is the mean kinetic energy per proton.

Proton Origin

In principle, the 6.4 keV line can also be produced by bombardment of sub-relativistic protons ($E \sim 100$ MeV). The presence of proton has been implied by discovery of diffuse TeV emission spatially correlated with the CMZ (Aharonian et al. 2006). The primary protons can be generated by accretion onto the Sgr A* in star capture events (Dogiel et al. 2011; Chernyshov et al. 2012). The $EW_{6.4\ \mathrm{keV}}$ has strong dependence (from ∼0.5 keV to ∼10 keV) on the proton index of the injecting source assuming power-law spectrum ($N \propto E^{\gamma}$; see figure 2.19).

Because of the relatively long lifetime of protons in comparison with the average time of star capture, the 6.4 keV line emission in the GC is quasi-stationary. In this case, extreme parameters of the proton model (star capture frequency, diffusion coefficient, etc) are necessary (Chernyshov et al., 2012).

2.4.2 Observational Results of the 6.4 keV Emissions

The observed X-ray spectra of many giant MCs (e.g., Sgr B2, Sgr C, Sgr A; see figure 2.20) exhibit common features of large equivalent width ($EW \geq 1$ keV) at the 6.4 keV line and strong absorption ($N_{\mathrm{H}} \geq 10^{23}$ H cm^{-2}) at the continuum below ∼ 5 keV, which favor the X-ray origin for the 6.4 keV emissions (e.g., Koyama et al. 1996; Murakami et al. 2000; Nakajima et al. 2009; Park et al. 2004; Nobukawa et al. 2010), rather than the electron origins (e.g., Yusef-Zadeh et al. 2007).

The X-ray origin has become even more conclusive after the discovery of the rapid 6.4 keV variabilities (see figure 2.21) in a few years from the small regions of a few light-years near Sgr B (Koyama et al. 2008; Inui et al. 2009) and Sgr A (Muno et al. 2007; Ponti et al. 2010). At the same time, the emission by the Thomson scattering is also expected because the 6.4 keV fluorescence is produced by the hard X-ray excitation above the iron absorption edge at 7.1 keV. Recently in Sgr B, a-few-years time variabilities of the continuum hard X-rays ($E \geq 8$ keV) in correlation with the 6.4 keV line are reported by Terrier et al. (2010) and Nobukawa et al. (2011). These fast variabilities indicate interactions in MCs by light-speed particle, i.e., X-ray.

On the other hand, there has been only one report for 6.4 keV emission consistent with electron-origin spectrum of low EW and small absorption, which is G 0.16−0.21 (EW ∼0.3 keV and $N_{\mathrm{H}} \sim 1 \times 10^{22}$ H cm^{-2}) found by Fukuoka et al. (2009) near the foot of the largest GC radio non-thermal filament, the radio arc (e.g., LaRosa et al. 2000).

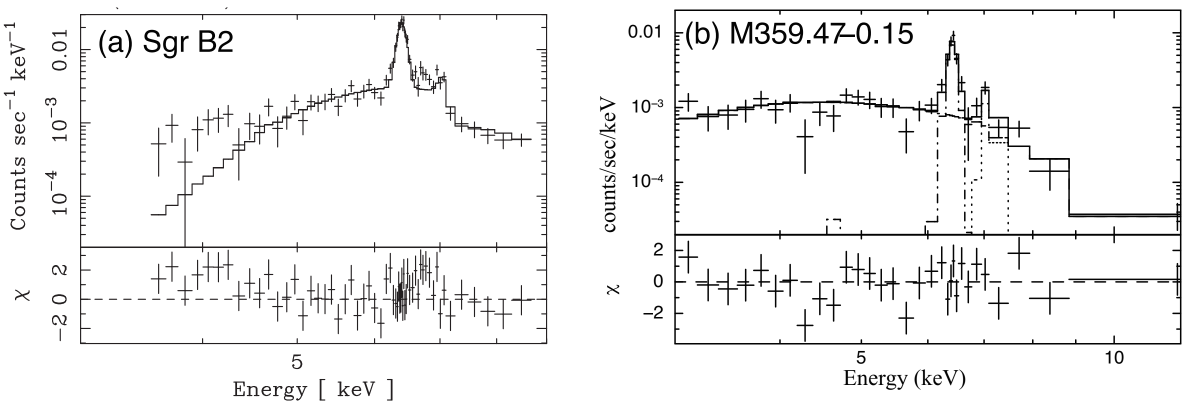

Fig. 2.20.—: X-ray spectra of giant MCs in the GC region after subtraction of the GCPE. (a) spectrum of Sgr B2 (Koyama et al., 2007b). (b) spectrum of M 359.43−0.07 in Sgr C (Nakajima et al., 2009). The spectral features suggest the X-ray origin (see text).

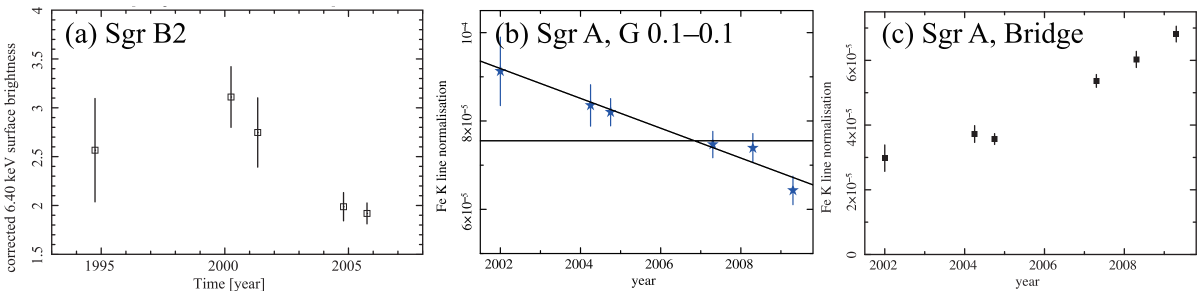

Fig. 2.21.—: Time variabilities of the 6.4 keV fluxes from giant MCs in a few years. (a) Sgr B2 (Inui et al., 2009). (b) G0.11−0.11, (c) Bridge (Sgr A; Ponti et al. 2010).

2.4.3 X-ray Reflection Nebula and Past Activities of Sgr A*

XRN Model

In the context of the X-ray origin (see figure 2.22), a luminous external source emitting hard X-rays is required to irradiate the MCs to produce the fluorescent 6.4 keV emission, i.e., the X-ray reflection Nebulae (XRNe; Koyama et al. 1996; Sunyaev et al. 1993). The estimation of X-ray (2–10 keV) luminosity of the irradiating source ($L_{\rm X}$) depends mainly on the 6.4 keV flux by reflection ($F_{6.4}$), the iron column density of the entire MC ($N_{\rm Fe} = 3.3\times10^{-5}\,Z_{\rm Fe}\,N_{\rm H}$), and the distance ($D$) between the MC/XRN and the source (c.f., Sunyaev & Churazov 1998; Murakami et al. 2000; Muno et al. 2007; Nobukawa et al. 2008; Capelli et al. 2012; also see equation (2.6)). Moreover, there are two cases for $L_{\rm X}$ according to the relation between the flare duration (Δt) and the cloud size ($\sim \sqrt{\text{projected area}} = \sqrt{S}$; typically ∼10 ly).

If the flare duration is longer than the light-crossing time of a cloud ($\Delta t > \sqrt{S}/c$), the entire cloud is illuminated and $L_{\rm X}$ is expressed in the following form.

$$L_{\rm X} \approx \quad A \times F_{6.4} \times D^2 \times N_{\rm Fe}^{-1} \times S^{-1} \times \sigma_{\rm Fe}^{-1} \tag{2.10}$$

Here, A is the integration factor (for $I_{\rm 8keV}$ in equation(2.6)) depending on the photon index of the X-ray spectrum of the primary source. S is the projective area of the cloud. $\sigma_{\rm Fe}$ is the known cross section of photoelectric absorption at 7.1 keV.

When the flare duration is shorter than the light-crossing time of a cloud ($\Delta t < \sqrt{S}/c$), only a part of the cloud ($\sim c\Delta t$) is illuminated. Thus, the actual $L_{\rm X}$ would be higher than the estimation in long-flare case (equation (2.10)) by a factor of $\sim \sqrt{S}/(c\Delta t)$, if assuming a uniform density (n) of the cloud. In other words, equation (2.10) corresponds to the average luminosity of the short flare over the light-crossing time of the cloud.

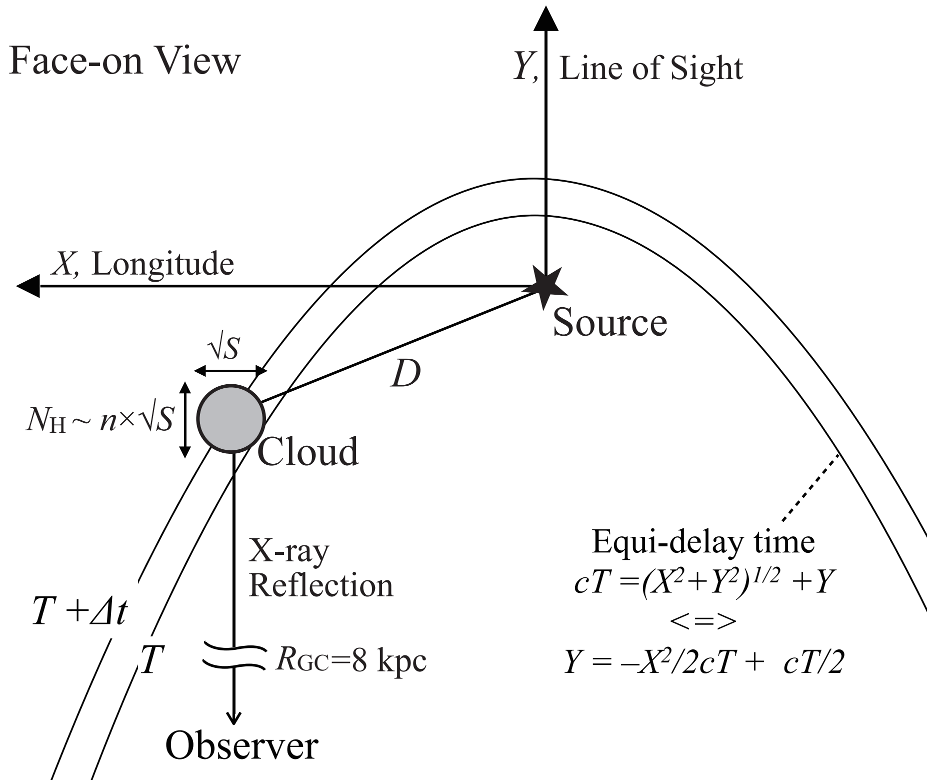

Fig. 2.22.—: Schematic face-on view of the geometry for the XRN model.

Unsolved Issues

The observed $F_{6.4}$ from MCs (e.g., Sgr B2: $\sim 10^{-4}$ photons cm^{-2}s^{-1}) require a primary source with luminosity of $L_{\rm x} > 10^{37}$ erg s^{-1} (Koyama et al. 1996; Nobukawa et al. 2011). Since nearby Galactic X-ray sources, with masses of $\sim 1M_\odot$, are not presently bright enough ($L_{\rm X} \leq 10^{37}$ erg s^{-1}) to explain the observed 6.4 keV fluxes from XRNe, the SMBH sited in the GC (i.e., Sgr A*) is believed to be the most reasonable candidate (e.g., Koyama et al. 1996; Ponti et al. 2010; Terrier et al. 2010; Nobukawa et al. 2011; Capelli et al. 2012).

Using the projected distance or poorly known positions between XRNe and Sgr A*, previous works roughly predicted that Sgr A* was very active several hundred years ago with the luminosity of $L_{\rm x} \sim 10^{39}$ erg s^{-1} (Koyama et al. 1996; Nobukawa et al. 2008; Ponti et al. 2010). This is about 6 order of magnitude higher than the present luminosity in the quiescent state ($L_{\rm x} \sim 10^{33}$ erg s^{-1}; Baganoff et al. 2003).

However, the property of the past activity of Sgr A* is still poorly understood. To begin with, it is not clear whether there was a single flare or multiple flares. Moreover, appropriate estimation for the luminosity, the occurrence time, and the duration of the flare were not possible. The distance is the most important factor to calculate the luminosity because other parameters can be directly determined from the X-ray observation (see equation (2.10)). The line-of-sight position of XRN define the light-traveling time from Sgr A*, i.e., the occurrence time of the flare. So far, these parameters are not well known for MCs in the CMZ (see figure 2.7 and text in section 2.1.2). Thus, in order to access the past of Sgr A*, we need the information on the three-dimensional (3-D; projected 2-D plus line-of-sight) geometry of XRNe.

2.5 Objectives and Approach of the Thesis

Considering the topics and issues of the GC region as reviewed above, we set the objectives of this thesis as below.

- The nature of un-investigated diffuse 6.4 keV emissions and XRNe.
- The nature of the low-temperature plasma emitting the diffuse 2.45 keV line.
- The 3-D positions of giant MCs in the CMZ.
- Quantitative information on the past activity (X-ray light curve) of the SMBH, Sgr A*.

We present an original self-consistent approach based on detailed 3-D spectral modeling and analysis of various emission components, for multiple regions of giant MCs in the GC region (Sgr B, Sgr C, Sgr D, and Sgr E; see figure 2.23) with the Suzaku X-ray data.

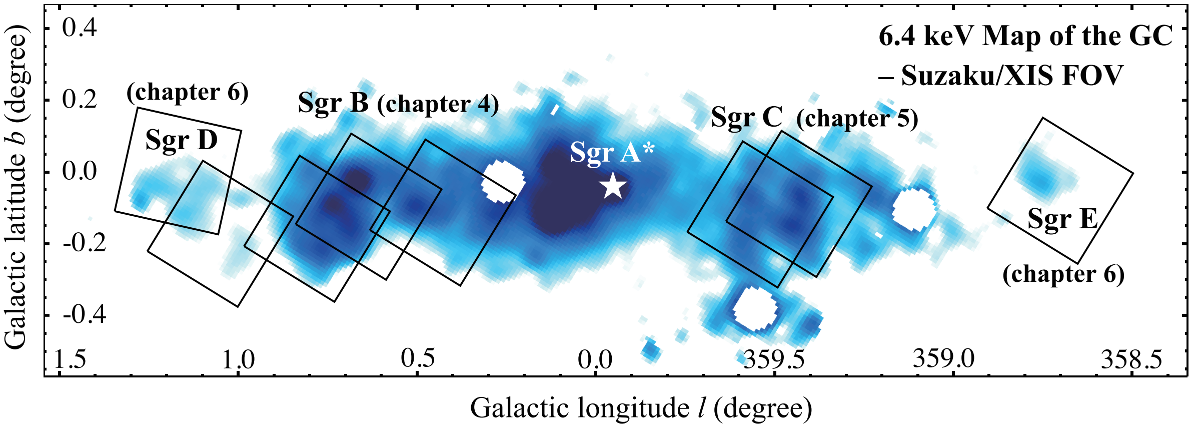

Fig. 2.23.—: The 6.4 keV intensity map of the Galactic center by Suzaku. The black boxes are the field of views (FOV) of the Suzaku/XIS (chapter 3) observations used for the data analyses (chapter 4, 5, and 6) in this thesis. The white circles are the excluded regions for bright point sources.

Chapter 3

Instruments

In this chapter, we review the X-ray satellite ”Suzaku” and the onboard instruments used for the data analysis in the thesis. We give an overview of the satellite in the first section and describe principles and specifications of the telescope and the detector in the following sections.

Contents

3.1 Overview of the Suzaku Satellite 29

3.2 X-Ray Telescope (XRT) 33

3.2.1 Overview of the XRT 33

3.2.2 In-flight Performance 35

3.3 X-ray Imaging Spectrometer (XIS) 37

3.3.1 Introduction of X-ray Charge Coupled Device 37

3.3.2 Overview and Specifications of XIS 38

3.3.3 In-flight Performance 41

3.4 Suzaku Advantages in the Study of the Galactic Center 44

3.1 Overview of the Suzaku Satellite

Following the successful Ginga and ASCA satellites, Suzaku (Mitsuda et al., 2007) is the fifth Japanese X-ray astronomy satellite developed under a Japan–US collaboration. The spacecraft was launched by the Japanese M-V-6 rocket from the JAXA Uchinoura Space Center (USC) on July 10, 2005. It was successfully put into a near-circular orbit with an apogee of 568 km, an inclination of 31.9 degrees, and an orbital period of about 96 minutes. Figure 3.1(a) shows a schematic view of Suzaku in orbit. The spacecraft length is 6.5 m along the telescope axis after extending the extensible optical bench (EOB) and the total weight is ~ 1700 kg, which makes it the largest and the heaviest Japanese X-ray satellite at present.

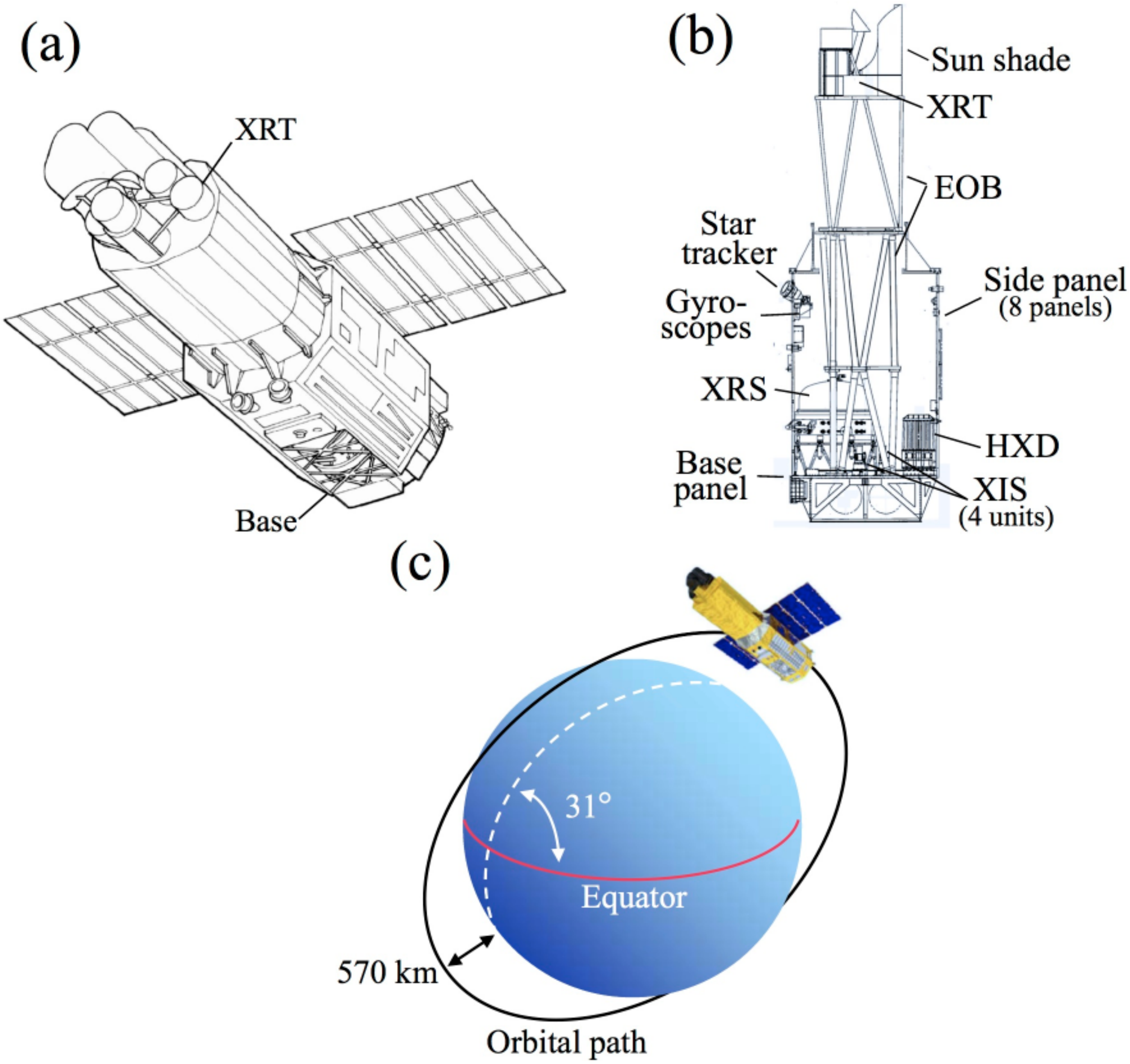

Fig. 3.1.—: (a) Schematic view of the Suzaku satellite (Mitsuda et al., 2007). (b) Schematic cross-section of the Suzaku internal structure after the EOB extension (Mitsuda et al., 2007). (c) The orbit of Suzaku around Earth.

The power supply is from solar panels fixed on the satellite, which provide the total electric power of $\sim$ 660 W. The Sun-angle constraint to the pointing direction is 65°–110° and therefore most celestial sources are available for observations for about 50 days every 6 months. The normal mode of operations have the spacecraft pointing in a single direction for at least 1/4 day (i.e., 10 ks net exposure time). Thus, most targets are blocked by the Earth for about 1/3 of each orbit, while some objects near the orbital poles can be observed nearly continuously. The observing efficiency of the satellite, measured after four years of operation, is about 43%.

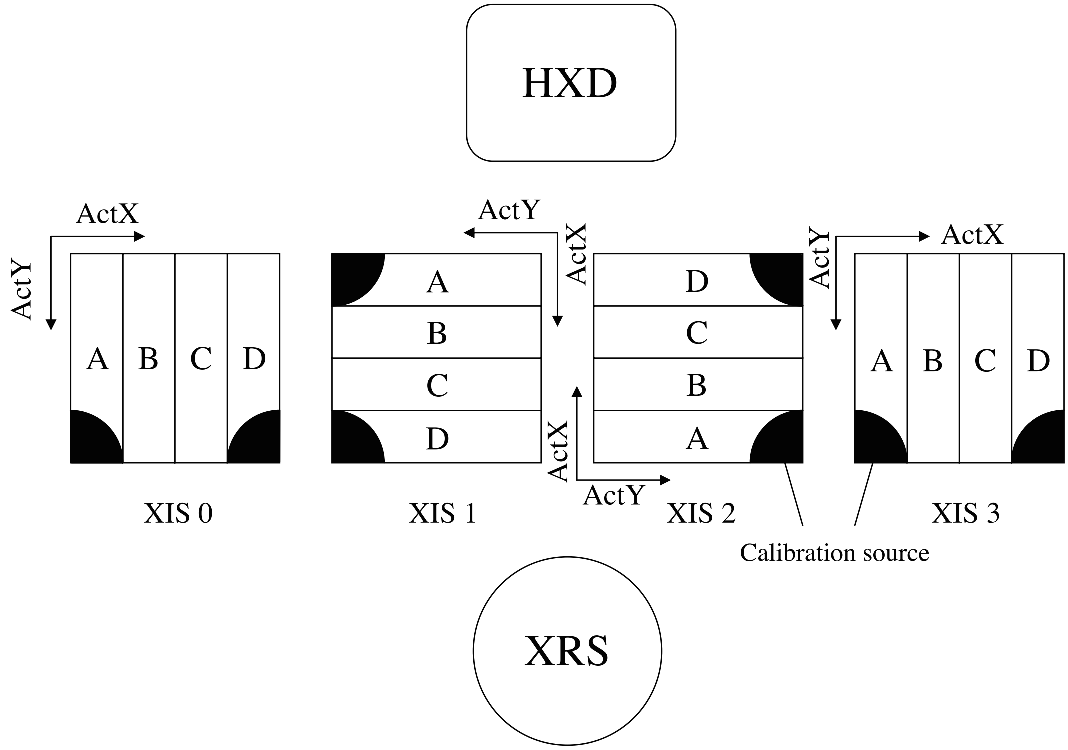

Fig. 3.2.—: Configuration of the detectors in the Suzaku satellite (Suzaku Technical Description, 2011). The definition of the XIS coordinates is also shown.

The scientific payload of Suzaku consists of three distinct co-aligned detector systems: the X-ray Imaging Spectrometer (XIS: Koyama et al. 2007a), the Hard X-ray Detector (HXD: Takahashi et al. 2007; Kokubun et al. 2007), and the X-ray Spectrometer (XRS: Kelley et al. 2007). Each of XRS and XISs is located at the focal plane of the dedicated X-ray Telescope modules (XRT: Serlemitsos et al. 2007). Figure 3.2 shows the configuration of detectors on the base panel.

The XISs are X-ray CCD cameras with a large field of view ($\sim$18'$\times$18'), moderate spectral resolution, and low background in the 0.3–12 keV band. The XRS is a micro-calorimeter for high-resolution spectroscopy, but is no longer operational due to a thermal accident soon after the launch[1]. It will not be used and discussed further. The HXD (Takahashi et al. 2007; Kokubun et al. 2007) is a non-imaging collimated hard X-ray instrument sensitive in the 10–600 keV band. A summary of the Suzaku capabilities is given in table 3.1.

For the scientific objectives of this thesis, we used the Suzaku data obtained with the XRT+XIS system. We describe their details in the following sections.

Table 3.1—: Summary of the Suzaku capabilities.

Space craft	Orbit apogee	568 km
	Orbital period	96 min
	Observing efficiency	$\sim 43\%$
XRT	Focal length	4.75 m
	Field of view	$17'$ at 1.5 keV
		$13'$ at 18 keV
	Effective area	440 cm^2 at 1.5 keV
		250 cm^2 at 8 keV
	Angular resolution	$2'$ (HPD)
XIS	Field of view	$17.'8 \times 17.'8$
	Bandpass	0.2–12 keV
	Pixel grid	1024×1024
	Pixel size	$24\ \mu\mathrm{m} \times 24\ \mu\mathrm{m}$
	Energy resolution	$\sim$130 eV at 6 keV (FWHM)
	Effective area	330 cm^2 (FI), 370 cm^2 (BI) at 1.5 keV
	Time resolution	8 s (normal mode), 7.8 ms (P-sum mode)
HXD	Field of view	$4.^\circ5 \times 4.^\circ5$ ($\geq$ 100 keV), $34^{'} \times 34^{'}$ ($\leq$ 100 keV)
	Bandpass	10–600 keV (PIN: 10–70 keV, GSO: 40–600 keV)
	Energy resolution	$\sim$3.0 keV (FWHM; PIN)
		$7.6/\sqrt{E_{\mathrm{MeV}}}\,\%$ (FWHM; GSO)
	Effective area	160 cm^2 at 20 keV, 260 cm^2 at 100 keV
	Time resolution	61 μs

---

[1] On August 8, 2005, a thermal short between the helium and neon tanks resulted in the liquid helium coolant venting to space.

3.2 X-Ray Telescope (XRT)

3.2.1 Overview of the XRT

Suzaku carries five light-weight thin-foil XRTs to collect the X-ray photon with large effect area. Four XRT modules are used for the XIS cameras and are referred to as XRT-I0, I1, I2, and I3 (figure 3.3), the remaining one is for the XRS, designated as XRT-S. The focal length of the XRT-I is 4.75 m. The XRTs are developed jointly by NASA/GSFC, Nagoya University, Tokyo Metropolitan University, and ISAS/JAXA.

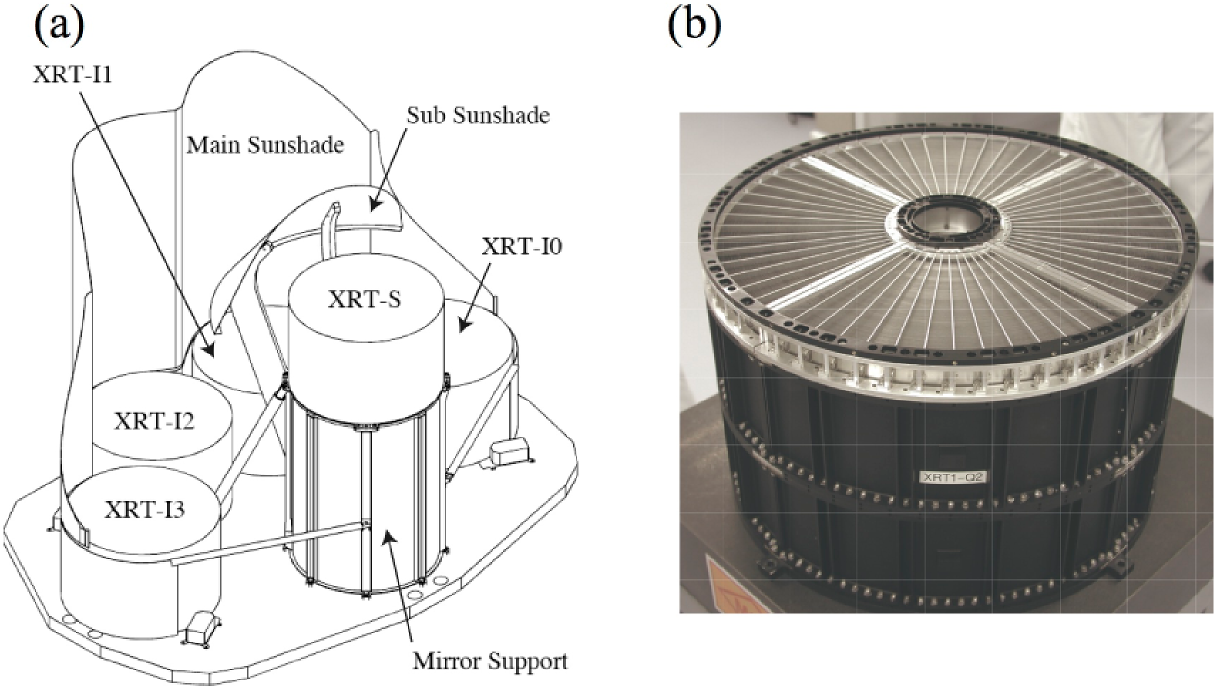

Fig. 3.3.—: (a) Schematic view of the XRT system mounted on the top plate of the Extensible Optical Bench.(b) Picture of the XRT-I1 module (Serlemitsos et al., 2007).

Here we explain the principles of X-ray reflection. X-rays are reflected by smooth surfaces of high-electron-density material at very shallow angles of $\leq 1^\circ$ (grazing incidence). Since the reflection is non-dispersive, circular X-ray mirrors for grazing incidence can focus X-rays over a broad energy band. In this configuration, only a fraction of the geometric area of the telescope can be used to collect X-ray photons for imaging, so multiple layers are combined to increase the effective area.

In Wolter type-I reflective optics, X-rays are reflected twice sequentially by a parabolic

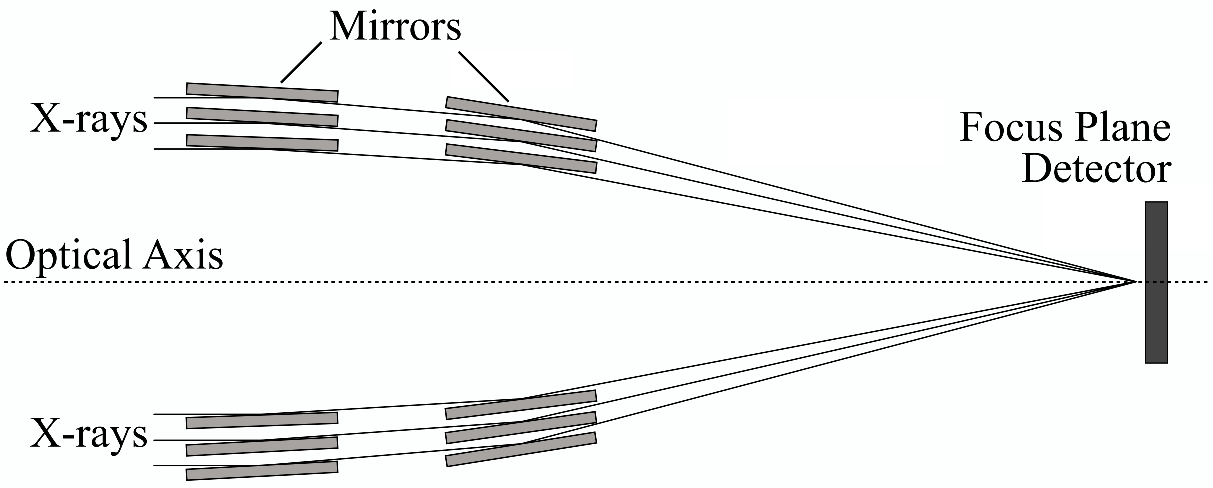

Fig. 3.4.—: Schematic cross-section of Wolter-I type X-ray mirror. Incident X-rays are reflected twice at very shallow angles and concentrated at the focal point.

surface and a hyperbolic surface (figure 3.3). The precise Wolter design yields a spatial resolution of ~ 1 arcsec, such as the X-ray telescope adopted for the Chandra X-ray Observatory (CXO; e.g., Weisskopf et al. 1996). However, this sacrifices the effective area, because the small surface roughness requires a heavy substrate and limits the number of nesting layers. On the other hand, it is difficult to construct a precise Wolter geometry with thin foils. In this case, the primary and secondary reflectors are approximated by simple cones, then the alignment inaccuracy and surface roughness limit the spatial resolution to about $\sim 1'$.

In the tradeoff between the angular resolution and the effective area, Suzaku takes the latter and adopts the grazing-incidence reflective optics consisting of many compactly nested and thin conical elements, rather than the Wolter type-I reflective optics with few and thick substrates. The small thickness of the reflectors on Suzaku permits high density nesting and thus provide large collecting efficiency with a moderate imaging capability in the energy range of 0.2–12 keV. The reflector surface is coated with Au with a thickness of ≥ 1000 Å for the high atomic number and therefor the high electron density. The weight of each telescope units are under 20 kg.

The angular resolutions of the XRTs range from $1.'8$ to $2.'3$, expressed in terms of half-power diameter (HPD), which is the diameter within which half of the focused X-rays (point source) are enclosed. The angular resolution does not significantly depend on the energy of the incident X-rays in the energy range of Suzaku, 0.2–12 keV.

3.2.2 In-flight Performance

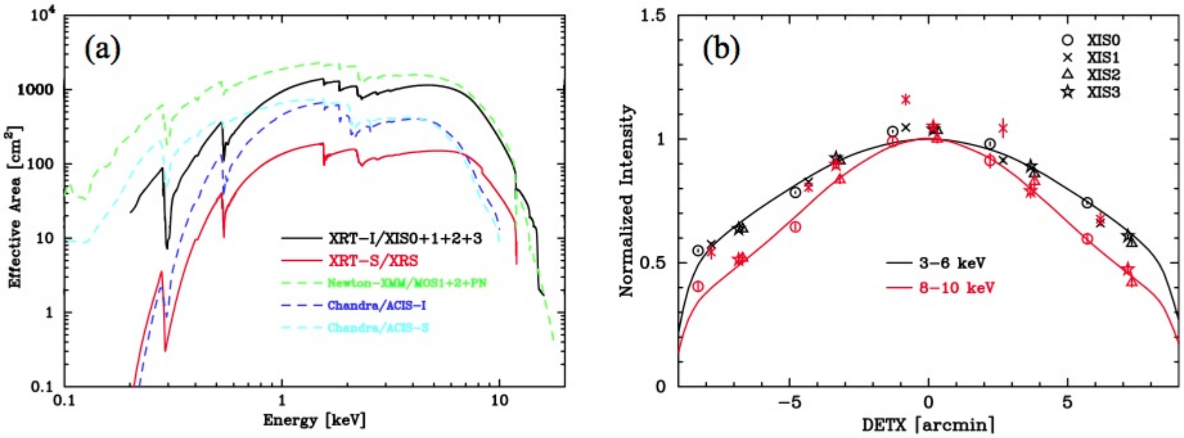

Fig. 3.5.—: (a) Total effective area of the XRT combined with the quantum efficiency of XISs (Serlemitsos et al., 2007). Those of other X-ray missions are also shown for comparison. (b) Off-axis angle dependence (vignetting effect) of the effective area, normalized at the optical axes. The soft and hard bands are shown with black and red points, respectively (Serlemitsos et al., 2007). Data are obtained from the observations of Crab nebula. The solid lines show the simulated model.

As the results of the grazing-incidence reflective optics of XRT and four XISs, Suzaku has moderate effective area in the soft band (440 cm^2 at 1.5 keV) and large effective area in the hard band (250 cm^2 at 8 keV), in comparison with other X-ray satellites. The energy-dependent on-axis effective area, including the detector efficiency, are shown in the left panel of figure 3.5. At larger off-axis angles, incident X-rays are partially obscured by neighboring reflectors and therefore smaller effective area, which is called the vignetting effect. This effect is prominent at high energy because high-energy photons have smaller critical angles and are more efficiently reflected at innermost mirrors, where the cone angles is small and the reflectors are tightly packed. Figure 3.5 (b) shows the vignetting curve in the soft (3–6 keV) and hard (8–10 keV) bands. Since the effective area is defined by the number of source photons within the CCD field of view (FOV) of a $17.'8$ square, the model curves show sharp drops at $\sim 8'$.

The angular resolution was verified with the SS Cyg data in quiescence state, as a target of point source (figure 3.6). The point source image appears to be a cross or a butterfly because the reflectors are made of four sections (”quadrants”) and therefore the spaces between any two quadrants are dead areas. Figure 3.7a and b show the point spread function (PSF) and the encircled energy function (EEF), respectively. These are typical indicators of the spatial resolution. Since the primary factor of the XRT spatial resolution is dominated by the imperfect alignment of the nested reflectors, and therefore the PSF is nearly independent on the energy.

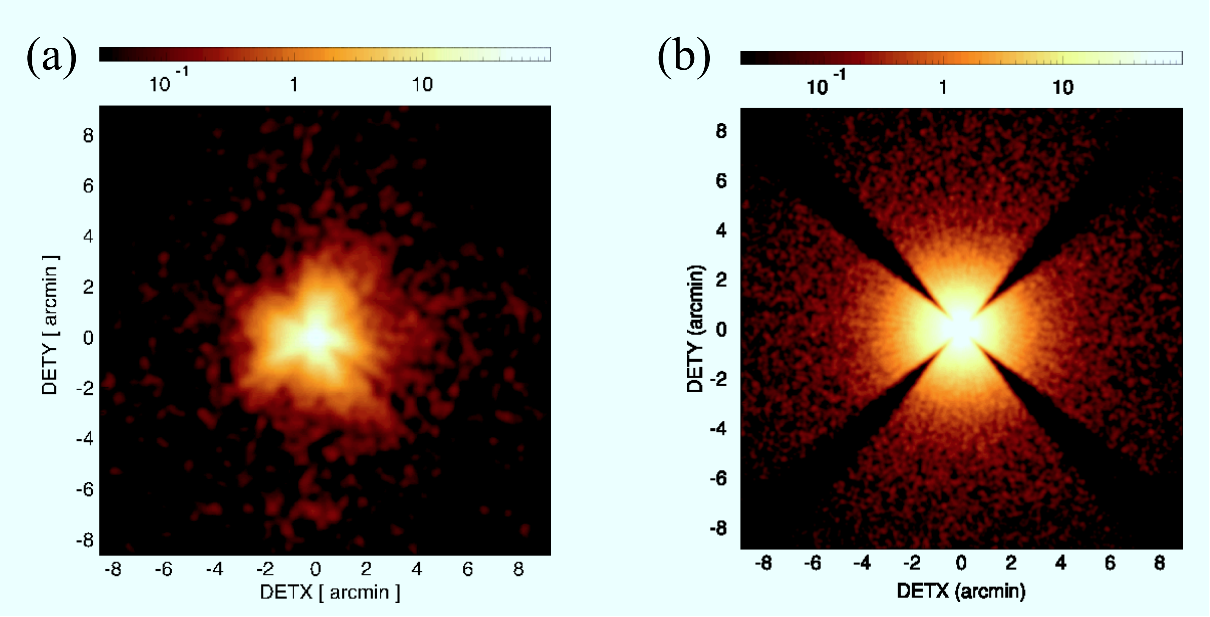

Fig. 3.6.—: (a) Observed image of SS Cyg (point source) at the optical axis taken with XRT-I0 (Suzaku Technical Description, 2011). (b) Simulated image of SS Cyg with XRT-I0. Note that the abrupt drop of the model curves at $\sim 8'$ is due to the source approaching the detector edge.

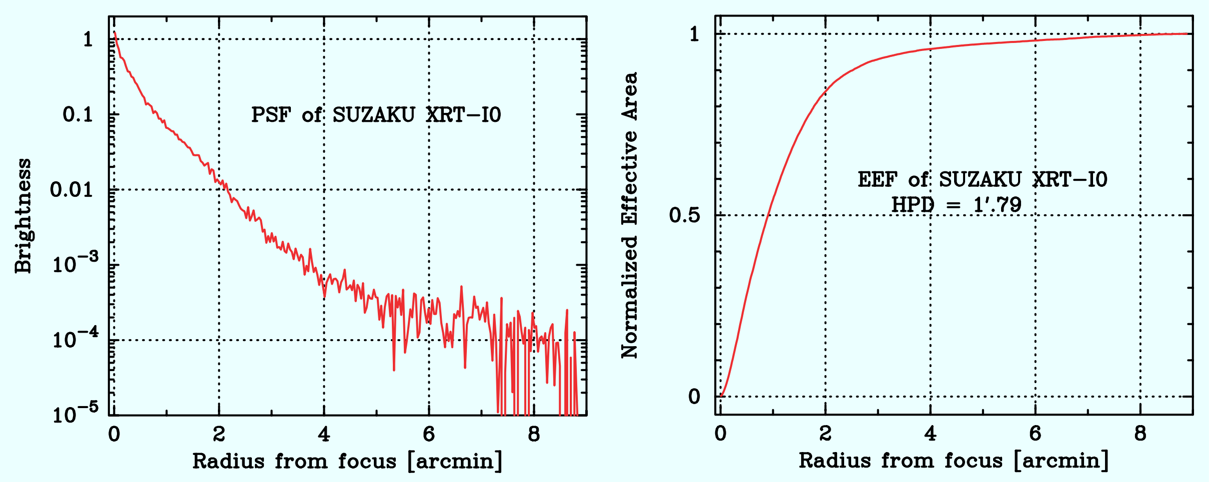

Fig. 3.7.—: Point spread function (PSF; left panel) and the encircle energy fraction (EEF; right panel) of the XRT-I0 (for XIS0) at the focal plane (Serlemitsos et al., 2007).

3.3 X-ray Imaging Spectrometer (XIS)

3.3.1 Introduction of X-ray Charge Coupled Device

Since the ASCA satellite, the charge-coupled device (CCD) has become the standard detector in the X-ray astronomical missions, i.e., Chandra (Garmire et al., 2003), XMM-Newton (Strüder et al., 2001; Turner et al., 2001), and Suzaku (Koyama et al., 2007a). The CCDs have good performance both in high-resolution imaging ($\sim$20 μm pitch pixel) and high energy resolution with fano-limited readout noise ($\leq$ 10 electrons in rms), which enable scientists to obtain the spatial and spectral information at the same time. This plays a very important role in studies of most celestial objects including supernova remnants, pulsar wind nebulae, and cluster of galaxies.

Through the photoelectric absorption in the silicon, CCD converts an incident X-ray photon to a electron cloud, the amplitude of which is proportional to the energy of the absorbed X-ray photon. The cloud made in the depletion layer in each pixel is then transferred to the gate of the output transistor by three-phase electric potential clocking. In MOS-type CCDs (figure 3.10), the gate is made of poli-Si ($\underline{\text{M}}$etal), the insulator is made of SiO_2 ($\underline{\text{O}}$xide), and the depletion layer is made of Si ($\underline{\text{S}}$emiconductor).

In the typical CCD readout architecture, the signal of each pixel is transferred in the form of charge over a long distance to a small number of readout nodes and then converted into voltage serially for all pixels. The readout noise is substantially reduced by applying the correlated double sampling (CDS) method at the readout node. The gain is uniform because of the small number of readout nodes. On the other hand, the time resolution is determined by the number of pixels, e.g., the readout time per frame is a few seconds for a CCD consisting of $\sim$1 M pixels. Another feature during the transfer is the charge transfer inefficiency (CTI), in which some fractions of the charge are trapped and lost due to the defects in silicon crystal after radiation damages by the cosmic rays in space. This effect can be suppressed and well corrected with the charge injection technology such as applied in Suzaku/XIS (Uchiyama et al., 2009).

After vigorous developments over the past two decades, X-ray CCDs have nearly matured and leaves little room for further essential advancements. In the near future, CCDs may be replaced by the progressing active pixel sensors (APS; e.g., Lechner et al. 2010; Prigozhin et al. 2009; Ryu et al. 2011), which access pixels directly and therefore are capable of more flexible and faster readout (see figure 3.8).

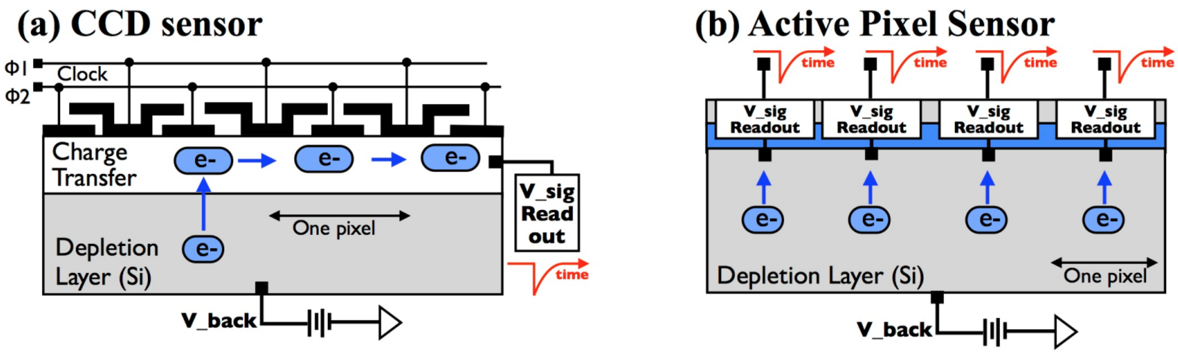

Fig. 3.8.—: Readout architectures of the CCD and the active pixel sensor (APS).

3.3.2 Overview and Specifications of XIS

The Suzaku XIS system (figure 3.9) is comprised of four MOS-type CCD cameras: three sets of front-illuminated (FI) CCD cameras (XIS 0, 2, and 3) and one set of back-illuminated (BI). Each CCD chip has an imaging area consisting of 1024 × 1024 pixels (1 pixel = 24μm square) for the 17.′8×17.′8 field of view (FOV). Schematic views are shown in figure 3.10 and figure 3.11.

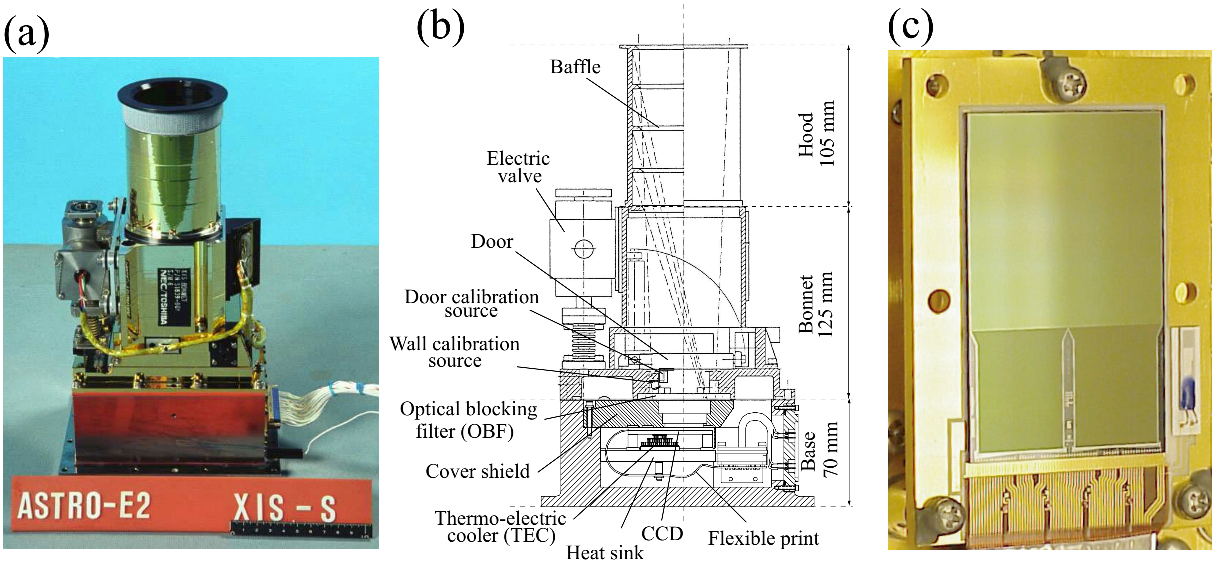

Fig. 3.9.—: (a) Picture of one of the XIS systems. (b) Cross section of the XIS system (Koyama et al., 2007a). (c) Picture of the XIS CCD sensor (Koyama et al., 2007a).

The front side of CCD is coated with the gate structure made of Si (0.28 μm) and

SiO_2 (0.44 μm). The back surface of BI CCD consists of 5 nm HfO_2 , 1 nm Ag, and 3 nm SiO_2, which is made by the chemisorption charging process in order to improves the charge collection efficiency near the back surface. These are the dead layers because X-ray charges generated there are not collected to the sense node. The dead layers of the FI and BI CCDs are ~ 0.7 μm and ~ 10 nm (see figure 3.10), respectively. Due to the absence of the gate structure, BI CCD achieve a high quantum efficiency (QE) even below ~ 1 keV. On the other hand, FI CCDs employ thicker depletion layer than BI CCDs (~ 76 μm for FI CCDs and ~ 42 μm for BI CCD), and therefore have higher QE for high-energy photons. The QE of FI and BI XIS, including the effects described above, are show in figure 3.12. Each XIS also has an optical blocking filter (OBF) to shutoff the optical and UV photons. The OBF is made of ~ 100 Å polyimide ($C_{22}H_{10}N_2O_4$) coated with Al of a ~ 1200Å thickness.

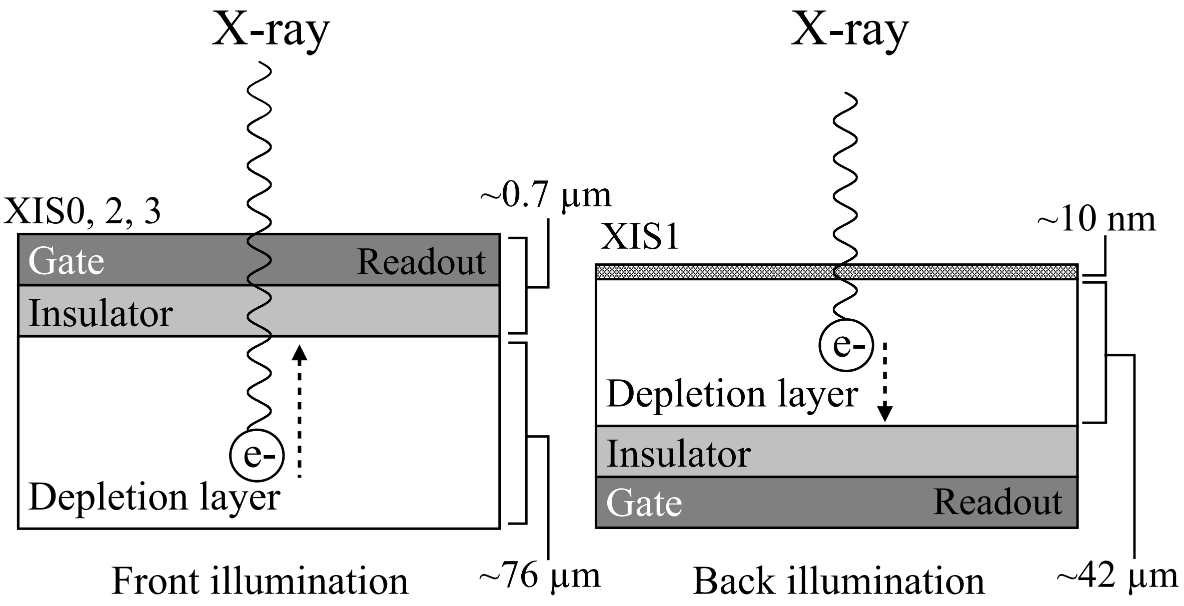

Fig. 3.10.—: XIS (MOS-type CCDs) in front illumination and back illumination.

When the CCD is operated in the frame transfer mode, the charges are transferred from the imaging area (IA) to the frame store (FS) region after an exposure (figure 3.11). The charges in the FS region are transferred vertically along the ActY direction and horizontally along the ActX direction sequentially. In both the IA and FS regions, the CCD chips have a format of 1024×1024 pixels and four read-out nodes. Thus, a CCD chip is composed of four segments of 256×1024 pixels (A–D; figure 3.11). The pixel size of the IA is 24 μm$\times$24 μm. In combination with XRT, one pixel corresponds to $1.''04 \times 1.''04$ of the sky, and the field of view is $17.'8 \times 17.'8$.

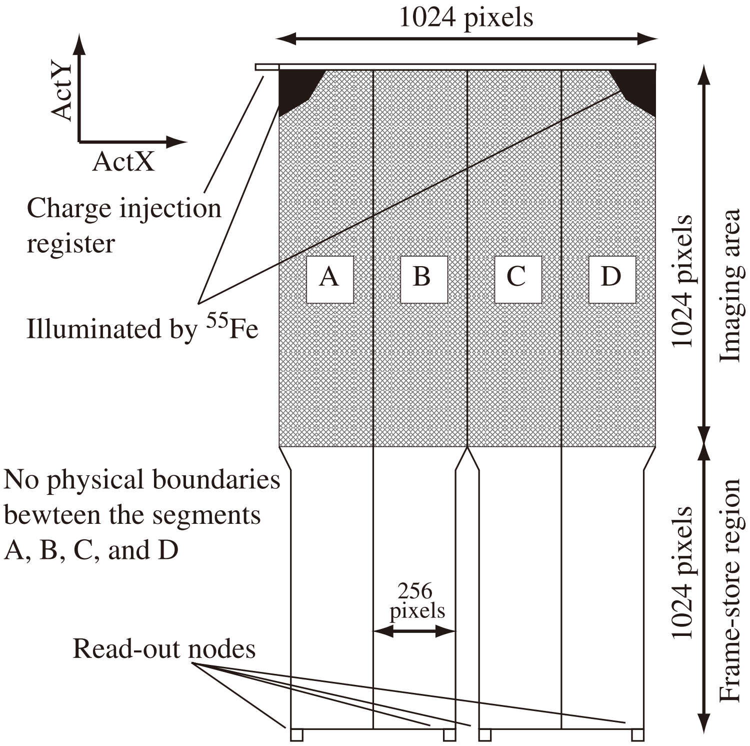

Fig. 3.11.—: Schematic view of the XIS CCD and the readout system (Koyama et al., 2007a).

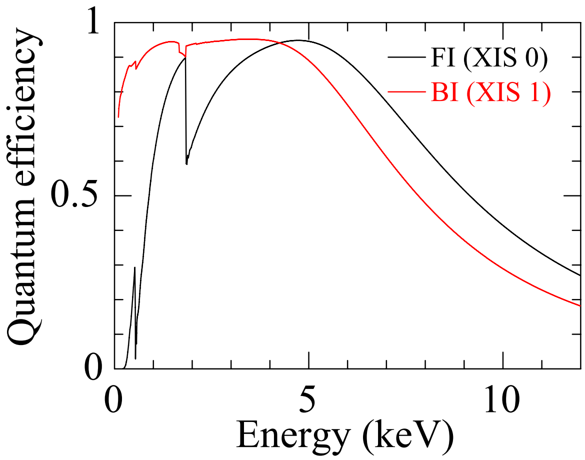

Fig. 3.12.—: Quantum efficiency of the XIS as a function of incident photon energy. The black and red curves are for XIS 0 and XIS 1 respectively (Koyama et al., 2007a). The effect of contaminant on the OBF is not included.

3.3.3 In-flight Performance

Operation

The on-orbit operating temperature of XISs is ~ -90°C controlled by Pertier coolers and always monitored at the JAXA Uchinoura Space Center.

The XISs have two clock modes for the on-board data processing: the Normal mode and the Parallel-Sum (P-sum) mode.

- **Normal mode:** the exposure time is 8 seconds, and all the pixels on the CCD are read out every 8 seconds, which corresponds to the time resolution. The data of pixels can be combined with either of the 5×5, 3×3, and 2×2 editing modes.
- **P-sum mode:** the pixel data from multiple rows are summed in the Y-direction in the FS region, and the summed value is put in the memory as a single row. The 1024 rows of data are read out in 8 s, and therefore the time resolution in the is $8/1024 = 7.8$ ms. This mode is useful to avoid the photon pileups in observations of very bright sources, at the sacrifice of the spatial information.

The Galactic center data in this thesis are all obtained in the Normal mode with the 3×3 editing mode.

Energy Calibration

For the calibration of the energy scale (gain tuning), each XIS is equipped with two radioactive sources (^{55}Fe), located on the side wall of the housing, to illuminate two far corners from the read-out nodes. A small fraction of the X-rays from the calibration sources is scattered onto the entire CCD. ^{55}Fe decays to leave ^{55}Mn via electron capture mainly (88.5%) from the K-shell. Subsequently, fluorescent X-ray is emitted, accompanied by an L→K electron transition (Kα: 5.895 keV) or an M→K electron transition (Kβ: 6.513 keV). These two lines are used to calibrate the high-energy range. Suzaku also has regular observations on 1E0102$-$72, which emits the $\mathrm{O_{VII}}$ (0.57 keV) and $\mathrm{O_{VIII}}$ (0.65 keV) lines, for the calibration of the low-energy range.

Charge Injection Capability

The charge transfer inefficiency (CTI) has been increasing since the launch due to charge traps caused by radiation damage (Nakajima et al., 2008; Ozawa et al., 2009). Consequently, the energy resolution has degraded, which was initially of ~ 130 eV at 5.9 keV in full width at half maximum. (figure 3.13). To mitigate the degradation, spaced-row charge injection (SCI) technique is applied for almost all observations since October 2006. In the SCI technique, electrons are injected from the furthest side from the read-out nodes to fill the traps as "sacrificial charges". This prevents charges generated by X-rays from being captured by the traps and actively reduces the CTI. A new calibration method dedicated for SCI observations has been established (Uchiyama et al., 2009). With this method, the energy resolution still retains ~ 155 eV and ~ 175 eV at 5.9 keV for FI and BI CCDs respectively as of March 2008 (figure 3.13).

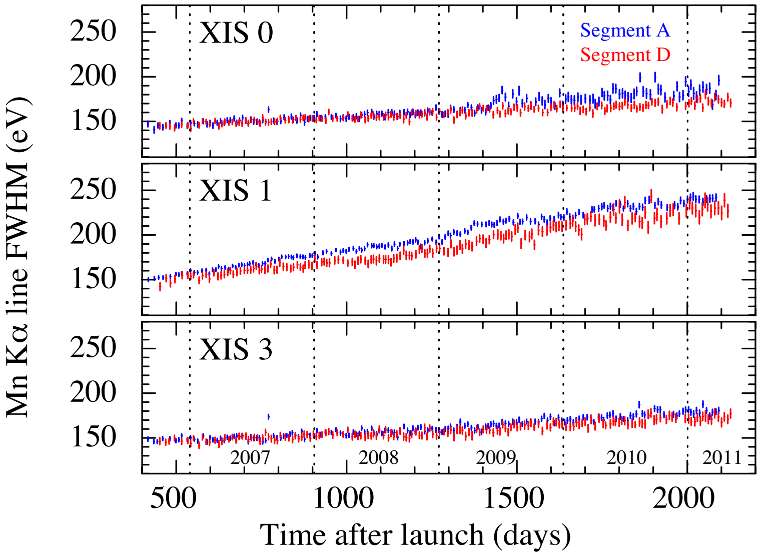

Fig. 3.13.—: Long-term trend of energy resolution (Suzaku Technical Description, 2011).

Contamination

Due to the accumulation of out-gassing from the satellite onto the OBF, the low energy QE has been gradually degraded (Koyama et al., 2007a). The contaminant is mainly composed of carbon and oxygen. The time evolution of the contamination has been measured using regular observations of 1E 0102–072. Although the chemical composition of the contaminant is still uncertain, it is assumed to be C/O=6. In the data analysis, the contamination effect is included in ancillary response files made by `xissimarfgen` (Ishisaki et al., 2007).

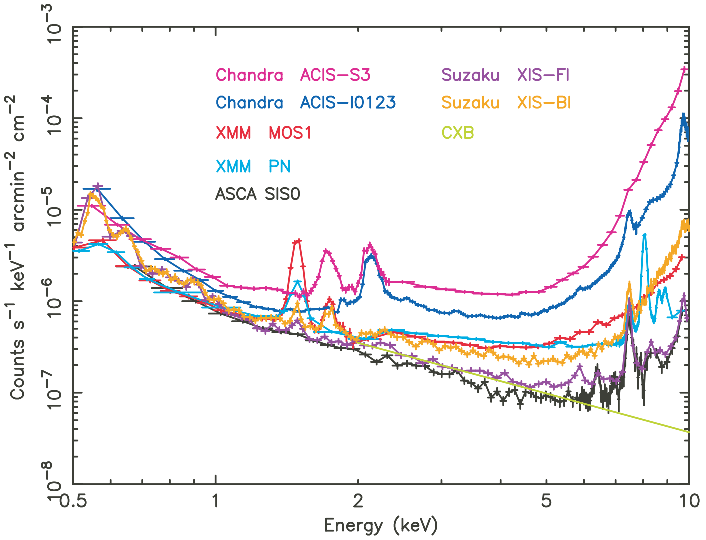

Fig. 3.14.—: Non-X-ray background (NXB) spectra of Suzaku XIS 0 (FI) and XIS 1 (BI). The spectra are constructed from night Earth observations. For comparisons, the background spectra of ASCA, Chandra, and XMM-Newton are also shown.

Non–X-ray background

The XISs are subject to the Non–X-ray background produced by the cosmic-rays on orbit. Figure 3.14 shows the non–X-ray background (NXB) accumulated during night-earth observations. The data are obtained during the South Atlantic anomaly passages and the calibration source areas are excluded. The NXB in the 0.5–10 keV band is about 8×10^{-8} counts s^{-1} pix^{-1} for the FI CCDs and 2×10^{-7} counts s^{-1} pix^{-1} for the BI CCD. The flux of NXB also depends on the geo-magnetic cut-off rigidity (COR, figure 3.14), but great concern on the COR is not necessary for most of the XIS observations. The NXB can be constructed for any observations with an accuracy of $\sim 5\%$, which is much smaller than the spatial fluctuation of the cosmic X-ray background in the 1–7 keV band, and is almost comparable to that in the 5–12 keV band (Tawa et al., 2008). Suzaku XISs have low backgrounds in comparison with other X-ray missions (see figure 3.14), thanks to the combination of the Suzaku orbit and the instrumental design.

Accidents

So far, the Suzaku CCD cameras have experienced two major accidents. On November 9, 2006, XIS 2 suddenly showed an anomaly, in which about 2/3 of the imaging area became unusable due to a large amount of charge leakage. Although not conclusive, this event was possibly caused by a micro-meteoroid impact, which is also seen in XMM-Newton and Swift. Since this anomaly, XIS 2 has been dysfunctional. On June 23, 2009, XIS 0 also showed an anomaly at once. During a Normal clocking operation, a part of the segment A of XIS 0 was flooded with a large amount of charges, which caused saturation of the analogue electronics. The anomaly was very similar to that occurred in the XIS 2 in 2006, probably had the same origin. Data from the segment A of XIS 0 is not available after this event. From the point of view in statistical expectation, for XISs, two impacts in four years is not too surprising.

3.4 Suzaku Advantages in the Study of the Galactic Center

As reviewed in chapter 2, the observation of Fe lines (6.4 keV and 6.7 keV) and hard X-rays up to 10 keV is essentially to reveal the nature (hot plasmas and X-ray reflection nebulae) and solve the issues in the Galactic center. Suzaku has two big advantages for this study. First, among all the present X-ray satellites and in the band over 5 keV, the Suzaku instruments (XRT+XIS) have the best overall performances in good energy resolution, low and stable NXB, and large effective area. Moreover, we have already strategically obtained rich Suzaku data of the Galactic center; the overall exposure is over 5 Msec and the FOVs cover a wide region of $\sim 4^\circ \times 2^\circ$. For these reasons, in the following chapters, we analyze the Suzaku data to attain the objectives of this thesis.

Chapter 4

Study of Sagittarius B

In this chapter, we construct a spectral model for the Galactic center diffuse X-rays and propose a new methodology to investigate positions of the Sgr B molecular clouds (MC) along the line of sight: a correlation study of the 6.4 keV line from the MCs and the line-of-sight absorption of the Galactic center plasma emissions (GCPE).

Contents

4.1 Observation and Data Reduction 45

4.2 Data Analysis and Results 46

4.2.1 Overall Features of the X-Ray Images 46

4.2.2 Complex Components in the Spectra 48

4.2.3 Model Constructions and Fitting 52

4.3 Discussion for Sgr B 58

4.3.1 Justifications of Model Constraints and Assumptions 58

4.3.2 Line-of-Sight Distribution of Sgr B MCs in the GCPE 59

4.3.3 XRN Features in Sgr B 61

4.3.4 The Correlation of CS Line and 6.4 keV Line 62

4.1 Observation and Data Reduction

The Sgr B region, located at east side of the GC (l ∼0.°7), contains the most well-known and massive MCs (e.g., Sgr B1 and B2) in the CMZ (c.f., section 2.1.2). Deep multiple pointing observations toward the Sgr B region were performed with Suzaku/XIS from October 2005 to September 2007. The observations were made in the normal clocking mode with read-out cycle of 8 s. We screened the data by excluding the events observed below the low and day-Earth elevation angles at 5°and 20°, in addition to the removal of events during passage of the South Atlantic Anomaly. The total effective exposure time was about 400 ks. The observation log is shown in table 4.1.

We performed the data reduction and analysis using HEADAS software version 6.5. The calibration database used to calculate the response of XIS and the effective area of XRT was the version released[1] on 2008-06-02. Since the relative gains and response functions of the FI CCDs are essentially the same, the FI spectra were merged in the spectral fitting. For the image and spectral analyses described in the following sections, the non-X-ray background (NXB; Tawa et al. 2008) was generated using the night-Earth observation data and was subtracted from the raw data.

Table 4.1—: Suzaku Observations near the Sgr B Region

Target name	Obs.ID	Pointing direction*		Obs.date	Exposure
		α (J2000.0)	δ (J2000.0)	(yyyy-mm-dd)	(ks)
GC Sgr B2	100037060	$17^{\rm h}47^{\rm m}30.^{\rm s}60$	$-28^\circ26'36.''6$	2005-10-10	76.6
GC Number2	500005010	$17^{\rm h}47^{\rm m}04.^{\rm s}63$	$-28^\circ37'46.''2$	2006-03-27	88.4
GC Sgr B East	501039010	$17^{\rm h}48^{\rm m}04.^{\rm s}87$	$-28^\circ21'06.''5$	2007-03-03	96.4
Sgr D SNR	502020010	$17^{\rm h}48^{\rm m}46.^{\rm s}13$	$-28^\circ07'38.''6$	2007-09-06	139.1

*The center of the XIS field of view.

4.2 Data Analysis and Results

4.2.1 Overall Features of the X-Ray Images

Figure 4.1 shows XIS images of the Sgr B region in the (a) 6.3–6.5 keV and (b) 2.5–3.5 keV bands. The images were made by co-adding the FI and BI CCDs data, followed by correcting the exposure time and the vignetting effects of the XRTs. The data of the CCD corners illuminated (contaminated) by the calibration sources were excluded. To increase the visibility, we binned the images with 4×4 pixels and smoothed them with a Gaussian kernel of $\sigma = 1'$.

---

[1] http://www.astro.isas.ac.jp/suzaku/caldb/

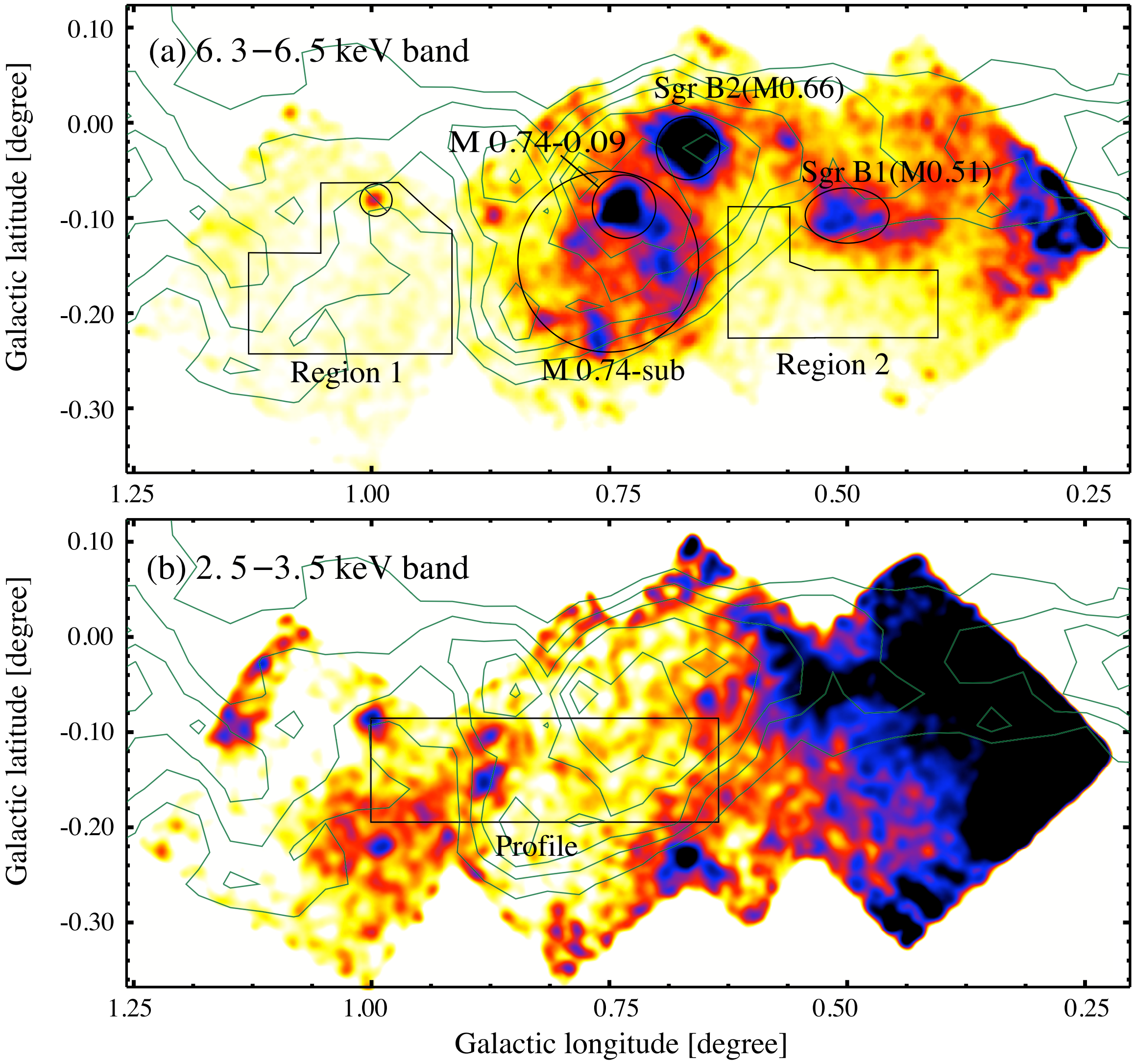

Fig. 4.1.—: XIS band images around the Sgr B region smoothed with a Gaussian kernel of $\sigma = 1'$. (a) The 6.4 keV band (6.3–6.5 keV), which contains the Fe I Kα line, tracing the dense molecular clouds. (b) Medium band (2.5–3.5 keV) showing the distribution of the GCDX in low energy. The CS-line contours (Tsuboi et al. 1999) in velocity range of -50–140 km s^{-1} are added with green solid lines in (a) and (b). A hint of anti-correlation between (a) and (b) near $l \sim 0.^\circ 75$ would be due to strong absorption by the molecular clouds. Spectra regions are shown in black solid lines in (a); the spectrum region for M 0.74-sub is the largest circle excluding the small circle of M 0.74-0.09. The bright point source (SAX J1748.2−2808; Nobukawa et al. 2009) is excluded for Region 1. The scan profile in figure 4.2 is made from the large rectangle (0.4 degree × 0.1 degree) in (b).

The bright clumps in figure 4.1a are Sgr B2 (M 0.66−0.02), M 0.74−0.09, and Sgr B1 (M 0.51−0.10). These are reported to be candidates of the X-ray reflection Nebula (XRN; Koyama et al. 2007b; Nobukawa et al. 2008). In addition, we found a new diffuse structure in the 6.4 keV line at the south of M 0.74−0.09 (hereafter, M 0.74-sub; figure 4.1a).

The GCDX flux in the 2.5–3.5 keV band (figure 4.1b) is sensitive to absorption in $N_{\rm H}$ ranges of 10^{22}–10^{24} H cm^{-2}. This range corresponds to the interstellar absorption toward the GC region and the intra-cloud absorption of the MCs. Comparing figure 4.1a and b, we found a hint of anti-correlation between the 6.3–6.5 keV (6.4 keV line) and the 2.5–3.5 keV band fluxes near l=0.°75: the 2.5–3.5 keV band flux is relatively weak in contrast with the strong emission of the 6.4 keV line from the Sgr B MCs.

To confirm this anti-correlation, we made one-dimensional flux profiles in the 2.5–3.5 keV band and the 6.4 keV-line band along the Galactic longitude of l=1.°0–0.°6 (see figure 4.2). For comparison, we also made profile and contours (in figure 4.1a and b) of the radio CS line ($J = 1 \rightarrow 0$) by extracting the velocity-integrated flux in the range of −50–140 km s^{-1} (Tsuboi et al. 1999), within which most of the Sgr B MCs is included. The CS-line flux profile is added in figure 4.2. For all of the profiles, the vertical axis represents the sum-value at the Galactic latitude $b = -0.°15 \pm 0.°05$ (see the solid rectangle in figure 4.1b); the flux of each profile is normalized at the maximum value, and hence the relative flux range is from 0 to 1.

As shown in figure 4.2, the flux profile of the 6.4 keV line shows a bump at l =0.°65–0.°85, which is in general agreement with that of the CS line. The 2.5–3.5 keV band flux, on the other hand, shows an intensity drop at the bump of the 6.4 keV line and the CS line, which implies absorption due to the MCs. Since the 2.5–3.5 keV band flux is sum of the GCPE behind the MCs (should be anti-correlated to the 6.4 keV-line flux) and the GCPE in front of the MCs (no correlation to the 6.4 keV-line flux), the intensity drop would be smeared out to only $\sim 15\%$. Detailed study of the spectra is given in section 4.2.2. We note that the angular size of the 6.4 keV bump is slightly narrower than that of the CS line and that of the intensity drop in the 2.5–3.5 keV band at $l \sim 0.°85$ (section 4.3.4).

4.2.2 Complex Components in the Spectra

We obtained X-ray spectra of the Sgr B region in the 0.5–10.0 keV band from the 6 solid line regions given in figure 4.1a. These are Sgr B2, M 0.74−0.09, Sgr B1, M 0.74-sub, Region 1, and Region 2. In figure 4.3, for brevity, we show 2 typical examples of the spectra.

The spectra have two notable common features (see figure 4.3). One is that the spectra exhibit many emission lines such as Fe XXV Kα (6.7 keV), Fe XXVI Kα (6.97 keV), Si XIII Kα (1.86 keV), S XV Kα (2.45 keV), and Fe I Kα (6.4 keV). These are K-shell lines

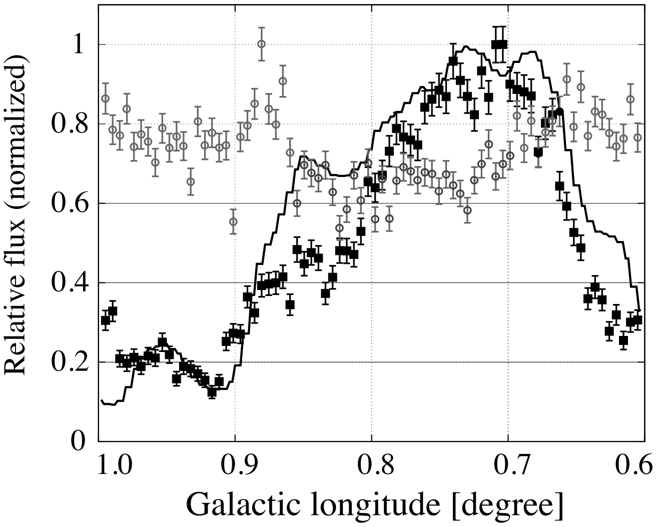

Fig. 4.2.—: One-dimensional profiles of the Sgr B region along the Galactic longitude from $l = 1.0°–0.6°$ at $b = -0.15° \pm 0.05°$ (see the solid rectangle in figure 1b). Gray open circles and black filled squares are data of the 2.5–3.5 keV band and the 6.4 keV band (6.3–6.5 keV) with 1-σ error bars, respectively. The radio CS line profile (-50–140 km s^{-1}) is plotted with the black solid line. The flux of each data is normalized to its maximum value.

from various atoms in various ionization states and hence the spectra are likely to consist of multi-temperature components, but may be reduced to at least three temperatures, which are responsible for the emission lines of the 6.4 keV (Fe I, cool gas), the 2.45 keV (S XV, hot plasma), and the 6.7 keV (Fe XXV, very hot plasma). The other feature is that the continuum shape shows broad local minima near 1–3 keV. Since the absorption of the GCDX spectrum is in the range of 6×10^{22}–10^{24} H cm^{-2}, the flux should rapidly drop below ~ 2 keV. The presence of the local minima, therefore indicates that the full-band spectra have an additional soft X-ray component with no significant (small) absorption (the foreground emission). As a consequence, we decompose the spectra of the Sgr B regions to the following five components:

(1) Very hot plasma responsible for the 6.7 keV line.

(2) Hot plasma responsible for the 2.45 keV line.

(3) Cool gas component that emits the 6.4 keV line.

(4) Low energy (0.5–2 keV) X-rays with small absorption.

(5) The cosmic X-ray background (CXB).

Koyama et al. (2007c) studied component (1) using the iron/nickel line flux ratios of K α

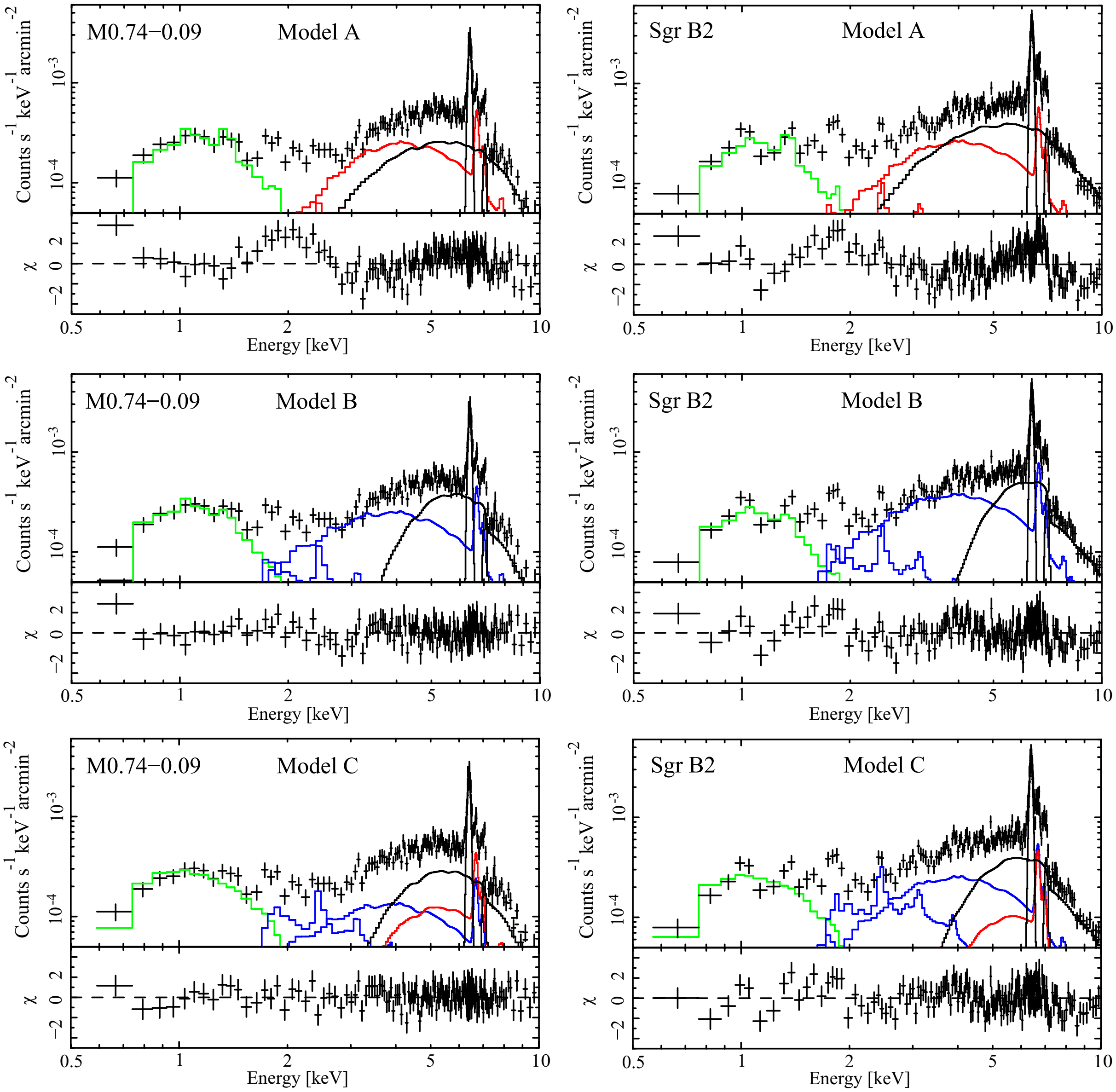

Fig. 4.3.—: FI spectra of M 0.74-0.09 (left column) and Sgr B2 (right column) as examples for different models. The best-fit spectra and the residuals (χ-distributions) of models A, B, and C are shown in the top, middle, and bottom rows, respectively. In each spectrum, components of the NGCE and the XRNE are shown by green and black solid lines; components of GCPE suffered by Abs1 × Abs2 and Abs2 are shown by the red and blue solid lines, respectively.

and K β in the GC region. They concluded that component (1) is a plasma of temperature k$T \simeq 6.5$ keV in collisional ionization equilibrium. The iron abundance was determined to be

$\simeq 1$ solar[2]. We therefore use an APEC model[3] for component (1) and express it as APEC1 with fixed temperature and abundances of 6.5 keV and 1 solar, respectively.

With the Suzaku GC survey observations, many SNR candidates were found in the 2.45 keV-line band images. The plasma temperatures are nearly the same at about 1 keV. (Nobukawa et al. 2008; Mori et al. 2008; Tsuru et al. 2009). The abundances are slightly different in each element, but are consistent with 1 solar. The abundances of S, the most prominent Kα line emitter, are 0.6–1.3 solar (hereafter, the numbers in the parenthesis are in 90% error range) for G 0.42−0.04 (Nobukawa et al. 2008), 1.2–1.5 solar for G 359.79−0.26 (Mori et al. 2008), and 1.1–2.7 solar for G 359.41−0.12 (Tsuru et al. 2009). Removing these SNR candidates, we still found the 2.45 keV line prevailing in all of the GC region (component (2)). Thus we use an APEC model for component (2) (APEC2), assuming that the temperature and abundances to be ~ 1 keV (free) and 1 solar (fixed), respectively, the same values to those of SNR candidates near the GC region.

Component (3) is emission possibly produced by the fluorescence and reflection from the MCs (XRNE): the fluorescent Fe I Kα (6.4 keV line) with Thomson scattering continuum. The spectra of XRNs in the Sgr B and Sgr C complexes were extensively studied with Suzaku (Koyama et al. 2007b; Nobukawa et al. 2008; Nakajima et al. 2009). Following these results, we use a phenomenological model: a power-law plus 2 Gaussian lines for the Fe I Kα and Kβ as,

$$\mathrm{XRNE} = A \times (E/\mathrm{keV})^{-\Gamma} + \mathrm{Gaussian1} + \mathrm{Gaussian2} \quad [\mathrm{photons\ cm^{-2}\ s^{-1}\ arcmin^{-2}}] \tag{4.1}$$

where the Gaussian center energy and relative intensity ratio of the Fe I Kα, Kβ lines are fixed to 6.4 keV and 7.05 keV, and $1 : 0.125$, according to the theoretical values (Kaastra & Mewe 1993).

Component (4) is low energy (≤ 2 keV) emission extending to nearly 0.5 keV, indicating small or no absorption, and hence the foreground emission, which is unrelated to the GC region. The origin is unknown but would be either a local Galactic plasma (Ebisawa et al. 2008) or unresolved faint dM stars (Masui et al. 2009). Apart from the real origin, the spectra of component (4) contains faint line-like structure (see figure 4.3), we therefore used an APEC model (APEC3). Since the contribution of component (4) above ~ 2 keV is small, the fitting results of the spectra above ~ 2 keV depend very weakly on the model assumption of component (4).

Component (5) is the cosmic X-ray background (CXB). We applied the CXB model obtained from the Suzaku data at the north ecliptic pole,

---

[2] The solar abundance here is referred to Anders & Grevesse (1989).

[3] Astrophysical Plasma Emission Code: A model of an emission spectrum from collisionally-ionized diffuse gas (Smith et al., 2001).

$$\mathrm{CXB} = 7.4\times10^{-7}\times(E/\mathrm{keV})^{-1.486} \quad [\mathrm{photons\ cm^{-2}\ s^{-1}\ arcmin^{-2}}] \tag{4.2}$$

As a matter of fact, the surface brightness of the CXB (see also Kushino et al. 2002) in the Sgr B region is far lower than those of the other components by more than two orders of magnitudes, and hence the contribution of the CXB is almost negligible.

4.2.3 Model Constructions and Fitting

For the full-band spectra of the five components, we tried model fitting with many free parameters. However, due to large errors, no significant constraint on the best-fit parameters was obtained for any further scientific study and discussion. We therefore set several constraints on the model based on reasonable assumptions.

We assume that the spectral shape of the GCPE, which comprises the two plasmas (APEC1 and APEC2), is the same in all of the Sgr B regions. We thus combine components (1) and (2),

$$\mathrm{GCPE} = \mathrm{APEC1} + \mathrm{APEC2} \quad [\mathrm{photons\ cm^{-2}s^{-1}arcmin^{-2}}] \tag{4.3}$$

The temperature and abundances of APEC1 are fixed to 6.5 keV and 1 solar, respectively. We define a parameter α, the normalization ratio of APEC1 and APEC2, assuming the common value in all regions near Sgr B (see figure 4.6). Thus, free parameters for the GCPE spectra are the temperature and the normalization factor of APEC2, and α with the same value among the relevant regions.

The photon indices (Γ) of the continuum of XRNs in Sgr B are scattered. This may be due to the limited energy band fittings in former studies. On the other hand, the equivalent width values of the 6.4 keV line are nearly the same (Koyama et al. (2007b), Nobukawa et al. (2008), Nakajima et al. (2009)). Since the emission mechanisms would be the same for all Sgr B XRNs, we assume that the photon index (Γ) and the equivalent width (EW) of the 6.4 keV line are the same in all regions of Sgr B.

Although each of components (1)–(5) should have a different absorption, we truncated them into three absorptions: Abs1, Abs2, and Abs3. Abs$\,i$ ($i = 1, 2, 3$) is the integrated value along the line of X-ray path into our sight, which is given as $\exp(-N_{\mathrm{H}}\times\sigma_{(E)})$; N_{H} and $\sigma_{(E)}$ are respectively the hydrogen column density and absorption cross section with solar abundance. A schematic view of these three absorptions is given in figure 4.4.

Abs1 is the largest absorption ($N_{\mathrm{H}} \geq 10^{23}$ H cm^{-2}), which takes place in/through the MCs. Abs2 is the interstellar absorption to/beyond the GC of $N_{\mathrm{H}} \sim 6\times10^{22}$ H cm^{-2} (Sakano et al. 2002). Abs3 is the smallest absorption applied to the foreground emission ($N_{\rm H} < 10^{22}$ H cm^{-2}).

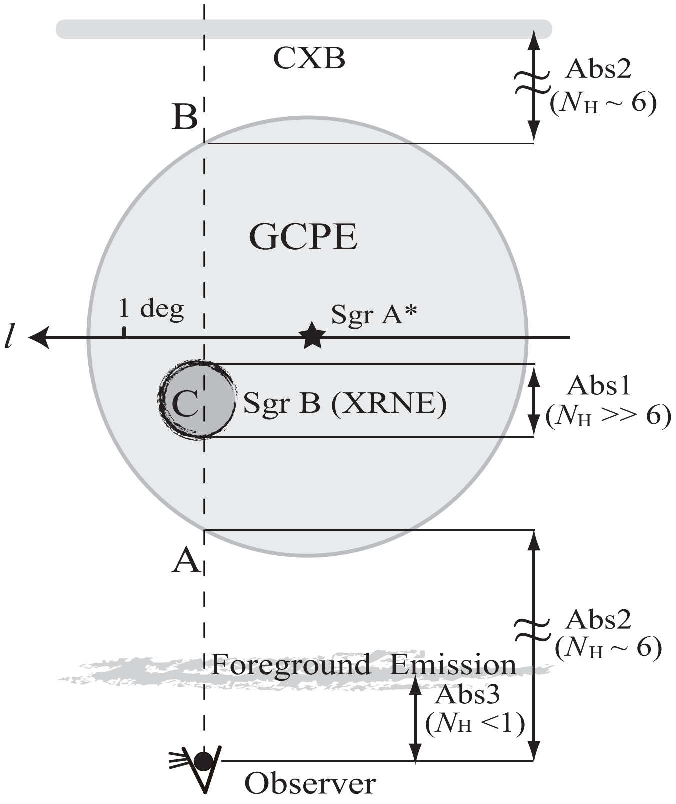

Fig. 4.4.—: Schematic view of the MCs distribution along the line of sight for Model C. The unit of absorption ($N_{\rm H}$) in the parentheses is 10^{22} H cm^{-2}.

In all 6 regions, we needed additional common components (4) and (5), which are not due to the emission from the GC region. We combined these components and define them as the non GC emission (NGCE):

$$\begin{aligned} \mathrm{NGCE} &= \mathrm{Abs1} \times \mathrm{Abs2} \times \mathrm{Abs2} \times \mathrm{CXB} + \mathrm{Abs3} \times \mathrm{APEC3} \\ &\qquad [\mathrm{photons\ cm^{-2} s^{-1} arcmin^{-2}}] \end{aligned} \tag{4.4}$$

The term Abs2×Abs2×CXB indicates that the CXB suffers from interstellar absorption (Abs2) two times: coming from the front and back sides of the GCPE. Here we assume that the absorption due to the back side on the GC is same as that on the front side of the GC.

Referring the schematic view of the geometry of the MCs (XRNE) and the GCPE, we tried two extreme cases (see figure 4.4). (A): a MC is located at the near-side edge of the GCPE, then the XRNE and GCPE would have nearly the same absorption of Abs1×Abs2. (B): a MC is located at the far-side edge of the GCPE; thus, the XRNE and the GCPE would have independent absorptions, given as Abs1×Abs2 and Abs2, respectively. Model A and Model B, therefore, are given as,

$$\begin{aligned} (\mathrm{A}): &\quad \mathrm{Abs1} \times \mathrm{Abs2} \times (\mathrm{XRNE} + \mathrm{GCPE}) + \mathrm{NGCE} \\ (\mathrm{B}): &\quad \mathrm{Abs1} \times \mathrm{Abs2} \times \mathrm{XRNE} + \mathrm{Abs2} \times \mathrm{GCPE} + \mathrm{NGCE} \\ &\qquad\qquad [\mathrm{photons\ cm^{-2}\ s^{-1}\ arcmin^{-2}}] \end{aligned} \tag{4.5}$$

In the fittings, the free parameters are Abs1, Abs2, and the normalization factors of the 6.4 keV-line flux, the GCPE, and the APEC3. While the mixing ratio α of APEC1 and APEC2 (in the GCPE), Abs3, the temperature and the abundance of APEC3, the equivalent width of the 6.4 keV line with respect to the power-law continuum ($EW_{6.4\ \mathrm{keV}}$), and the photon index (Γ) for the power-law spectrum of XRNE are also free, but are assumed to be the same (commonly linked) in all relevant regions. We list the fitting parameters according to their properties in table 4.2.

Table 4.2—: Summary of free and fixed parameters in the fittings for Model A, B, and C.

	Free parameters for each region
Absorption:	N_{H} (Abs1), N_{H} (Abs2)
XRNE*:	normalization (Fe I Kα 6.4 keV line)
GCPE*:	normalization (APEC2), position $R^{\dagger}$
NGCE*:	normalization (APEC3)
	Free parameters commonly linked in all regions
Absorption:	N_{H} (Abs3)
XRNE*:	photon index Γ, equivalent width $EW_{6.4\ \mathrm{keV}}$
GCPE*:	kT (APEC2), α (normalization ratio of APEC1/APEC2)
NGCE*:	kT (APEC3), abundances Z (APEC3)
	Fixed parameters
XRNE*:	Fe I line energy Kα = 6.4 keV, Kβ = 7.05 keV, flux ratio (Kβ/Kα) = 0.125
GCPE*:	kT (APEC1) = 6.5 keV, Z (APEC1 & APEC2) = 1 solar
NGCE*:	CXB = equation (4.2)

* See equation (4.1), equation (4.3), equation (4.4) for the definitions of XRNE, GCPE, and NGCE, respectively.

† For Model C only, see equation (4.6) and the text.

We performed a simultaneous fitting for the 2×6 spectra (the FI and BI spectra of 6 regions) with Model A and Model B. The best-fit parameters and χ^2/d.o.f are listed in table 4.3. As a results, both models were rejected by the χ^2/d.o.f test. Model A gave a large χ^2/d.o.f of 1.87, and shows large residuals in the medium range of 1–3 keV and the hard range of 5–7 keV (see figure 4.3). The best-fit values of Abs1 × Abs2 (with Model A) is $\simeq 10 \times 10^{22}$ H cm^{-2} (see table 4.3), which are close to the typical value toward the GC region. These values may be reasonable for the GCPE but could not be applied to the XRNE,

Table 4.3—: Results of best-fit parameters* with Model A and B.

	MODEL A		MODEL B		
Region	$N_{\rm H}$† (Abs1×Abs2)	6.4 keV line‡	$N_{\rm H}$† (Abs1)	$N_{\rm H}$† (Abs2)	6.4 keV line‡
Sgr B2	$10.9^{+0.9}_{-0.5}$	$3.0^{+0.1}_{-0.1}$	$54.8^{+2.8}_{-2.4}$	$5.8^{+0.4}_{-0.1}$	$6.6^{+0.2}_{-0.2}$
M0.74-0.09	$10.7^{+0.5}_{-0.4}$	$2.5^{+0.1}_{-0.1}$	$40.4^{+2.0}_{-1.7}$	$5.2^{+1.0}_{-0.8}$	$4.3^{+0.1}_{-0.6}$
Sgr B1	$8.4^{+0.2}_{-0.2}$	$1.53^{+0.04}_{-0.08}$	$26.3^{+2.0}_{-1.8}$	$6.3^{+0.2}_{-0.1}$	$2.2^{+0.1}_{-0.1}$
M0.74-sub	$7.4^{+0.1}_{-0.4}$	$1.25^{+0.02}_{-0.02}$	$21.9^{+0.6}_{-1.0}$	$5.0^{+0.1}_{-0.1}$	$1.63^{+0.03}_{-0.02}$
Region1	$6.1^{+0.1}_{-0.1}$	$0.24^{+0.01}_{-0.01}$	$18.6^{+1.9}_{-1.2}$	$4.6^{+0.1}_{-0.1}$	$0.33^{+0.01}_{-0.01}$
Region2	$7.7^{+0.1}_{-0.3}$	$0.43^{+0.01}_{-0.03}$	$31.8^{+2.2}_{-1.9}$	$5.8^{+0.1}_{-0.2}$	$0.76^{+0.02}_{-0.04}$
Region-common parameters					
kT (keV) (APEC2)	0.70 (0.68–0.72)		0.69 (0.68–0.74)		
α ($\frac{\rm APEC1\,norm}{\rm APEC2\,norm}$)	0.47 (0.46–0.48)		0.59 (0.57–0.60)		
Photon index Γ	0.52 (0.47–0.59)		2.16 (2.10–2.23)		
$EW_{6.4\ \rm keV}$ (keV)	1.78 (1.75–1.80)		1.31 (1.28–1.34)		
Abs3 (10^{22} H cm^{-2})	0.21 (0.21–0.22)		0.20 (0.19–0.21)		
kT (keV) (APEC3)	1.02 (0.99–1.05)		0.93 (0.92–0.94)		
Z (solar) (APEC3)	0.004 (0.002–0.006)		0.008 (0.007–0.011)		
χ^2/d.o.f §	$4749/2537 = 1.872$		$4479/2537 = 1.765$		

*The uncertainties are at 90% confidence level.

†The value of $N_{\rm H}$ in the unit of 10^{22} H cm^{-2}.

‡Flux in the unit of 10^{-6}photons cm^{-2}s^{-1}arcmin^{-2}.

§The results obtained by the simultaneous fitting of the 12 spectra (the FI and BI spectra of 6 regions).

because the absorption of each XRNE was found to be $> 10^{23}$ H cm^{-2} by independent analysis of XRN (Koyama et al. (2007b); Nobukawa et al. (2008); Nakajima et al. (2009)).

In Model B, the apparent residuals in the medium and hard range found in Model A disappeared partially, and hence χ^2/d.o.f was improved to 1.77. We still see unnatural residuals between 2–4 keV. Although the χ^2/d.o.f of 1.77 is large enough to reject Model B at more than the 99.9% confidence level, this value is slightly smaller than that of Model A. At the end of this section, we discuss why we reject Model B from a different point of view.

We then constructed Model C, adding a new free parameter R (for each region), in which a MC/XRN is inside the GCPE with a relative position of R (0–1); the smaller R indicates the nearer (front) side.

$$\begin{aligned} \text{(C)}:\quad & \text{Abs1} \times \text{Abs2} \times (\text{XRNE} + (1-R) \times \text{GCPE}) \\ & + \text{Abs2} \times (R \times \text{GCPE}) + \text{NGCE} \\ & \qquad [\text{photons cm}^{-2}\ \text{s}^{-1}\ \text{arcmin}^{-2}] \end{aligned} \tag{4.6}$$

We performed a simultaneous fitting for Model C by the same procedure as for Model A and B. Although Model C has six new free parameters (R for the six regions) more than Model A and Model B, the degree of freedom (d.o.f) of Model C (2531) is almost equal to that of Model A and and B (2537). On the other hand, the χ^2/d.o.f of Model C is largely improved to 1.34 from those of Model A (1.87) and Model B (1.77).

One may argue that the spectra are contaminated by unresolved point sources in the Sgr B region. In fact, Koyama et al. (2009) estimated that the point source fluxes provide a significant fraction of the GCDX (GCPE + XRNE) emission, up to about 1/6 near Sgr A*, which may partially contribute to the 6.7 keV-line and the 6.4 keV-line fluxes in the GCPE and XRNE, respectively. According to the Chandra cataloged sources reported by Muno et al. (2006), the number of point sources per solid angle near Sgr B2 is $\sim 10\%$ compared to that near Sgr A*, while Nobukawa et al. (2008) shows that the GCDX flux near Sgr B2 is also $\sim 10\%$ of that near Sgr A*. We can infer that the contribution of point sources to GCDX would be roughly the same in the Sgr B region. The point source contribution may cause possible systematic errors in the present spectral analysis. The most serious errors, therefore, should be the region-to-region fluctuation of the fractions of the point source fluxes, which may be rather small effects in a relative comparison of the best-fit parameters. At this moment, we have no information on the exact flux and spectrum of the integrated point sources in the Sgr B region. We therefore ignore the point source contribution.

All together, taking account of possible systematic errors due to the point source contribution and those due to the simplified model, we regard Model C as a good approximation of the overall spectra in the Sgr B region, although the χ^2/d.o.f of 1.34 is statistically marginal to be acceptable. The best-fit common parameters for all regions are as follows (hereafter, the numbers in the parenthesis are in 90% error range). The temperature of APEC2 is 0.87 (0.81–0.91) keV and the mixing ratio (α) in the GCPE is determined to be 0.27 (0.26–0.28). The photon index (Γ) and the equivalent width (EW) of the 6.4 keV line for the XRNE are 1.72 (1.64–1.80) and 1.59 (1.54–1.63) keV, respectively. The absorption (Abs3), temperature (kT) and the abundance of the foreground emission (APEC3) are 0.17 (0.16–0.18)$\times 10^{22}$ H cm^{-2}, 0.85 (0.83–0.87) keV, and 0.011 (0.009–0.014) of solar, respectively. The other best-fit parameters of Model C for each region are listed in table 4.4.

The 6.4 keV line is likely to be fluorescence in the MC generated by an external X-ray source. Then the flux should be proportional to the product of the external X-ray flux and the number of iron atoms along the line-of-sight X-ray path in the MC, in the optically thin case at the energy near 6.4–7.1[4] keV ($N_{\rm H} \leq 10^{24}$ H cm^{-2}). The number of iron atoms is approximately proportional to the column density $N_{\rm H}$ of the MC. Therefore, in the case that the external X-ray fluxes are the same among the MCs, Abs1 should be approximately proportional to the 6.4 keV-line flux.

In figure 4.5, we plot the best-fit Model C values of Abs1 and Abs2, as a function of the 6.4 keV line flux. For a comparison, we also plot the results of Model B. A notable fact to support Model C is that Abs1 is in good proportionality to the 6.4 keV flux. This feature is in

---

[4] E = 7.1 keV is the K absorption-edge of neutral iron.

Table 4.4—: Detailed results of best-fit parameters with Model C.

Region	$N_{\mathrm{H}}^{\dagger}$ (Abs1)	$N_{\mathrm{H}}^{\dagger}$ (Abs2)	6.4 keV line‡	APEC3 norm§	GCPE norm$^{\Vert}$	Position $R^{\#}$
Sgr B2	$36.5^{+2.4}_{-2.2}$	$8.2^{+0.3}_{-0.5}$	$5.1^{+0.3}_{-0.3}$	$0.09^{+0.01}_{-0.01}$	$3.40^{+0.36}_{-0.48}$	$0.44^{+0.06}_{-0.06}$
M0.74-0.09	$22.9^{+2.0}_{-1.8}$	$6.8^{+0.4}_{-0.4}$	$3.3^{+0.2}_{-0.2}$	$0.11^{+0.01}_{-0.01}$	$2.67^{+0.29}_{-0.28}$	$0.31^{+0.04}_{-0.04}$
Sgr B1	$12.3^{+1.0}_{-1.0}$	$7.0^{+0.2}_{-0.3}$	$1.8^{+0.1}_{-0.1}$	$0.11^{+0.01}_{-0.01}$	$3.46^{+0.25}_{-0.38}$	$0.41^{+0.06}_{-0.06}$
M0.74-sub	$11.5^{+0.5}_{-0.5}$	$5.3^{+0.1}_{-0.2}$	$1.42^{+0.03}_{-0.03}$	$0.090^{+0.003}_{-0.004}$	$1.66^{+0.10}_{-0.09}$	$0.26^{+0.04}_{-0.04}$
Region1	$7.2^{+0.2}_{-0.2}$	$3.6^{+0.2}_{-0.3}$	$0.26^{+0.01}_{-0.01}$	$0.105^{+0.006}_{-0.004}$	$1.40^{+0.05}_{-0.04}$	$0.15^{+0.01}_{-0.01}$
Region2	$12.0^{+0.6}_{-0.8}$	$6.3^{+0.1}_{-0.1}$	$0.47^{+0.03}_{-0.03}$	$0.130^{+0.004}_{-0.036}$	$2.88^{+0.11}_{-0.18}$	$0.34^{+0.04}_{-0.04}$
χ^2/d.o.f**			$3382/2531 = 1.336$			

[*] The uncertainties are at 90% confidence level.

[†] The value of N_{H} in the unit of $10^{22}\,\mathrm{H\,cm^{-2}}$.

[‡] Flux in the unit of 10^{-6}photons $\mathrm{cm^{-2}s^{-1}arcmin^{-2}}$.

[§] The normalization factor for the foreground emission (c.f., APEC3 in equation (4.4)) of the APEC model re-normalized with the region size A [arcmin^2]; it is expressed as $7.07 \times 10^{-11}/(4\pi D^2\, A)\, EM$ [cm^{-5}arcmin^{-2}], where D and EM are the distance to the source [cm], and the emission measure [cm^{-3}], respectively.

[‖] In same expression as §, but the normalization factor of APEC2 in the GCPE (c.f., equation (4.3) and text).

[#] R is the fraction of the GCPE suffered by Abs2, which indicates the positions of MCs (see equation (4.6) and figure 4.7).

[**] The results obtained by the simultaneous fitting of the 12 spectra (the FI and BI spectra of 6 regions).

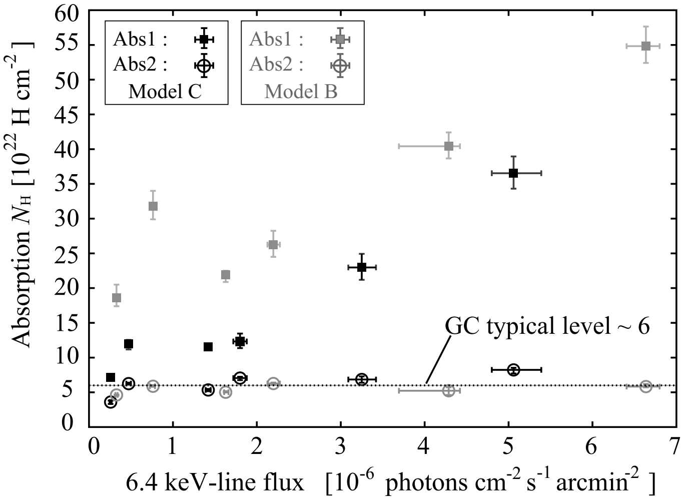

Fig. 4.5.—: Correlations between the 6.4 keV-line flux and absorptions (made from data listed in table 4.3 and table 4.4). Results of Model C and Model B are plotted by the black and gray marks; filled squares and open circles represent Abs1 and Abs2, respectively.

contrast to the results of Model B, where the proportionality is not very good in the low-flux range. Most importantly, Model B requires an extra off-set of about 2×10^{23} H cm^{-2}, which is un-realistic. This leads us to exclude Model B in addition to the χ^2/d.o.f test. We estimated $N_{\rm H}$ values of the Sgr B MCs from the data of the CO line (Sofue 1995; Dahmen et al. 1998) and the CS line (Tsuboi et al. 1999). They are in the range of $N_{\rm H} = 10^{23}$–10^{24} H cm^{-2}, in good agreement with the Model C prediction.

As shown in figure 4.5 for Model C, we found that Abs2 is almost constant at $N_{\rm H} \sim 6 \times 10^{22}$ H cm^{-2}. This is consistent with the view that Abs2 is interstellar absorption (see figure 4.4) toward the GC of about $N_{\rm H} \simeq 6 \times 10^{22}$ H cm^{-2} (Rieke et al. 1989; Sakano et al. 2002).

4.3 Discussion for Sgr B

4.3.1 Justifications of Model Constraints and Assumptions

In the previous section, we introduced a complicated model to described the spectra of the GCDX. In order to obtain meaningful values (no large errors) of physical parameters, we further added some constraints and assumptions. If, for example, we let the normalization ratio α (APEC1/APEC2) to be free for all regions, we can not give a significant constraint on the absorptions of GCPE and/or the temperature of APEC1, because the two plasma emission become nearly the same in the band near 2 keV. We summarize the adopted constraints and assumptions below for further discussions:

- The 6.5 keV plasma and ~ 1 keV plasma, which comprise the GCPE, have nearly the same angular distribution near the Sgr B region. (see figure 4.6)
- The abundances of the GCPE are nearly 1 solar, the same value as those of nearby new SNR candidates.
- The XRNE has a common photon index (Γ) and $EW_{6.4\ {\rm keV}}$ near the Sgr B region.
- The point sources contribution to the GCDX is small and hence could be ignored in the Sgr B region.

The most fundamental constraint is the first item; the factor α is constant from region to region. This implies that the angular distributions of the very hot (6.5 keV) and hot ($\sim$1 keV) plasmas are nearly the same near Sgr B. In order to judge this constraint, we show the flux distribution of the 6.7 keV and 2.45 keV lines along the galactic longitude of

$l = 1.^\circ 2$–$0.^\circ 4$ at $b = -0.^\circ 15 \pm 0.^\circ 05$ (figure 4.6). The 6.7 keV and 2.45 keV lines are strong characteristic lines that well represent, respectively, the distributions of the 6.5 keV plasma and the ~ 1 keV plasma with the least systematic errors.

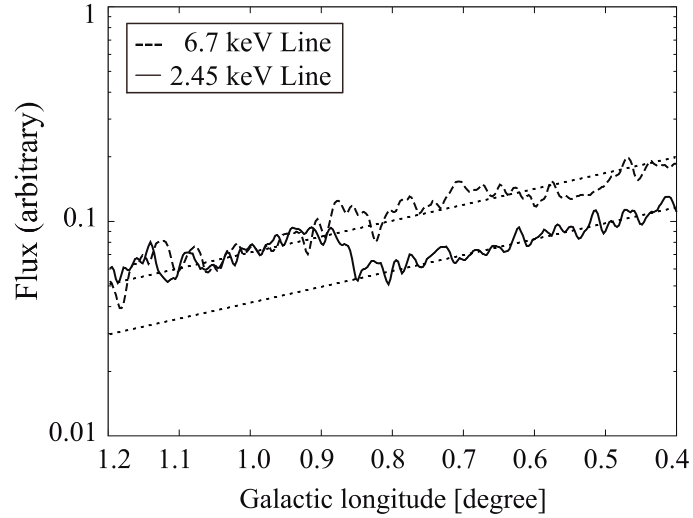

Fig. 4.6.—: Flux distribution of the 6.7 keV line (6.5 keV plasma; dashed line) and the 2.45 keV line ($\sim$1 keV plasma; solid line) along the galactic longitude from $l = 1.^\circ 2$–$0.^\circ 4$ at $b = -0.^\circ 15 \pm 0.^\circ 05$. Two parallel dotted lines guide eyes to see the same distribution of the 6.5 keV plasma and the $\sim$1 keV plasma.

As is found in figure 4.6, the 2.45 keV line and the 6.7 keV line have almost the same slope (angular distribution). The small drop of the 2.45 keV-line flux near at $l = 0.^\circ 85$–$0.^\circ 6$ would be due to absorption by the M 0.74−0.09 MC and the drop at $l = 0.^\circ 6$–$0.^\circ 4$ is due to the absorption by the Sgr B1 MC. This figure, therefore, indicates that the emission of the $\sim$1 keV plasma (APEC2) and the 6.5 keV plasma (APEC1) have a common normalization ratio (α) for the GCPE near the Sgr B regions. The justification of the other constraints and assumptions listed in the last three items are separately discussed in the previous sections. We thus conclude that Model C with the above listed constrains and assumptions provides a practical approximation for the overall spectra in the Sgr B region, although the χ^2/d.o.f of 1.34 is statistically marginal to be acceptable.

4.3.2 Line-of-Sight Distribution of Sgr B MCs in the GCPE

From the results of section 4.2.3, we conclude that the MCs of Sgr B should be located in the GCPE (Model C), neither in the near-side edge (Model A) nor in the far-side edge (Model B) of the GCPE. For simplicity, we assume that the volume emissivity of the GCPE is approximately a uniform sphere with a uniform plasma density on the Galactic plane. Koyama et al. (1989) and Yamauchi et al. (1990) reported that the 6.7 keV line distributed with a Gaussian shape of 1.8 deg (FWHM) (in parallel to the Galactic plane). We therefore take the boundary (radius) at $|l| = 1.25$ deg, within which 90% of the GCPE is included. The center of the GCPE is approximately Sgr A* (at l= -0.°056; Yusef-Zadeh et al. 1999). Then the parameter R gives the line-of-sight positions of the MCs within the GCPE[5], where $R = 0$ and 0.5 indicate the anterior border line and the center line (Sgr A* is on this line) of the GCPE, respectively. We plot the best-fit position parameter (R) for the 6 regions (indicated in figure 4.1a) in the schematic view of figure 4.7. As demonstrated in figure 4.7, the MCs in the Sgr B region are generally on the near-side with respect to Sgr A*.

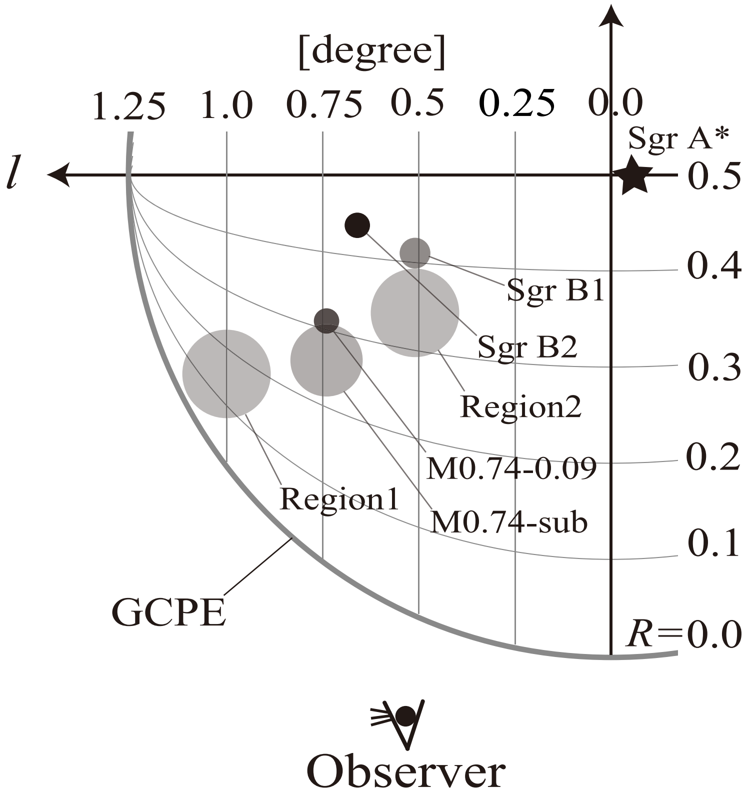

Fig. 4.7.—: Relative positions of each MC (filled circles) along the line of sight, where the horizontal lines of $R = 0.0$ and 0.5 imply the anterior border line and the GC line (Sgr A* is on this line), respectively. The circles filled with darker colors indicate MCs of the larger N_{H} values.

---

[5] The emission measure EM can be written as $\int n_{\mathrm{e}} n_{\mathrm{H}} \mathrm{d}V = n_{\mathrm{e}} n_{\mathrm{H}} S \int \mathrm{d}l \propto n_{\mathrm{e}} n_{\mathrm{H}} S L$, where L is the length of the GCPE in the line of the sight, S and $n_{\mathrm{e}} n_{\mathrm{H}}$ are the projected area and the product of densities of electrons and hydrogens, respectively. Then the parameter R is the fraction of $EM^{\mathrm{front}}_{\mathrm{GCPE}}/EM^{\mathrm{all}}_{\mathrm{GCPE}}$, which is equal to $L^{\mathrm{front}}_{\mathrm{GCPE}}/L^{\mathrm{all}}_{\mathrm{GCPE}}$: the relative line-of-sight position of MCs in the GCPE.

It may be suspicious that the best-fit values of R in Model C indicate that the MCs are all closer to the near-side edge of the GCPE rather than to the far-side edge, while χ^2/d.o.f. $= 1.872$ of Model A (MCs at the near-side edge) is rather worse than χ^2/d.o.f. $= 1.765$ of Model B (MCs at far-side edge). As shown in equation (4.5), Model B have the extra-part Abs2×GCPE which Model A does not have. This gives a slightly better χ^2/d.o.f. of Model B (1.765) than Model A (1.872). On the other hand, the improvement of Model C (χ^2/d.o.f.$= 1.336$) from Models A (and B) is far larger than that between Model A and B.

In this section, we have only shown the line-of-sight positions for MCs from the values of R under an assumption of a uniform density for the GCPE. We can furthermore determine the actual positions quantitatively using the R parameter together with the three-dimensional information of the GCPE distribution measured by Uchiyama et al. (2012). This analysis will be performed in chapter 7.

4.3.3 XRN Features in Sgr B

According to former studies (Koyama et al. 2007b; Nobukawa et al. 2008), the equivalent width of the 6.4 keV line and the continuum photon index (EW, Γ) of the Sgr B XRNs have been reported to be (1.1 keV, 3.2) for Sgr B2, (1.55 keV, 1.4) for M 0.74-0.09, and (1.4 keV, 1.8) for Sgr B1. The Γ values are significantly scattered among the XRNs, but the variation of EW is not very large. The GCPE flux is position-dependent, which means that a proper background-selection is difficult. The large scatter of Γ values in the former studies may be due to the nearby GCPE-subtraction and would also be due to the band limited (e.g. 5–8 keV) spectral fitting. In this work (Model C), the EW and Γ values are estimated by an independent method, a simultaneous fitting of a wide energy band (0.5–10.0 keV), in which nearby GCPE was not subtracted but directly included as the GCPE model. We also note that these uncertainties do not largely affect the EW values. In fact, We found that the averaged $EW \simeq 1.6$ keV, which is consistent with the previous studies of the Sgr B XRNs. Koyama et al. (2009) studied the GCDX near the Sgr A region ($|l| \leq 0.^\circ2$), and found that the Γ of the continuum flux is 1.9; this reduced to 1.4 if we exclude the point sources contribution. Nakajima et al. (2009) studied the 6.4 keV clumps in the Sgr C region and found Γ to be in range of 1.6–1.9. We determined the common Γ in Sgr B to be $\simeq 1.7$; this value agrees with the results in Sgr A, B, and C. Thus, we infer that the XRNE may have a unified photon index of 1.4–1.9 in the overall GC region.

As discussed by Koyama et al. (2008) and Nobukawa et al. (2008), a possible external X-ray source is Sgr A*, therefore the X-ray flux at the Sgr B MCs should be proportional to $L_0 D^{-2}$, where L_0 and D are, respectively, the luminosity of Sgr A* and the distance between Sgr A* and MCs. Thus the flux of the fluorescent 6.4 keV line should be modified by this

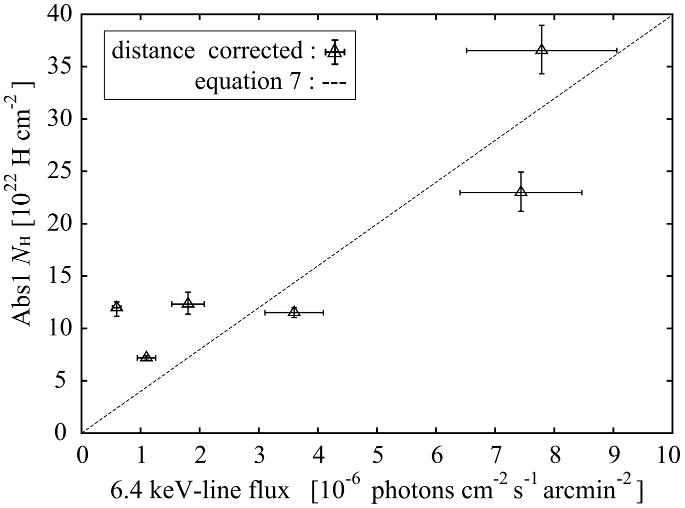

Fig. 4.8.—: The best-fit absorption (Abs1) vs the distance-corrected 6.4 keV-line flux from results of Model C in table 4.4 (open triangles), where the correction factors are estimated from the distances between MCs and Sgr A* with figure 4.7, and are normalized to that of Sgr B1.

distance effect. In figure 4.8, we plotted distance-corrected 6.4-keV fluxes as a function of Abs1, where the distances are estimated using figure 4.7. We then fitted the correlation between the best-fit absorption (Abs1) and the 6.4 keV line flux (distance-corrected), and obtained,

$$\begin{aligned} N_{\rm H}\,({\rm Abs1}) &= 3.99\,(\pm 0.56)\times I_{6.4\ {\rm keV}}\ \ [10^{22}\ {\rm H\ cm^{-2}}], \\ I_{6.4\ {\rm keV}} &: [10^{-6}\ {\rm photons\ s^{-1}\ cm^{-2}\ arcmin^{-2}}] \end{aligned} \tag{4.7}$$

This relation is generally in agreement with the fluorescent process due to irradiation by Sgr A* with the past luminosity of 2–3×10^{39} ergs s^{-1}. If L_0 was time constant, the relation between the distance-corrected 6.4 keV-line flux vs. Abs1 should be in good proportionality. However, we see some data scatters from the proportionality relation (figure 4.8). It can be explained by assuming a time variable flux of the irradiating source Sgr A* (Koyama et al. 2008; Inui et al. 2009). We will show and discuss its details in chapter 7.

4.3.4 The Correlation of CS Line and 6.4 keV Line

As shown in figure 4.2, the 2.5–3.5 keV band flux shows an intensity drop at the bump of the 6.4 keV line and the CS line. The anti-correlation to the 2.5–3.5 keV band flux is clearer in the CS line than that in the 6.4 keV line. This may be because that the CS line traces all (GC + foreground) MCs in the line of sight from which the GCPE may suffer absorption, while the 6.4 keV line only traces MCs near the irradiating source in the GC region. The better anti-correlation of the CS line against the 2.5–3.5 keV band flux indicates that a large amount of MCs, identified by the velocity-integrated CS lines but not bright in the 6.4 keV line, is located in the near side of the GCPE. The angular size of the 6.4 keV bump is slightly narrower than that of the CS line, as seen at the bump edges near $l \sim 0.^\circ 85$ and $l \sim 0.^\circ 63$. The narrower angular size of the 6.4 keV bump than that of the CS line may also be explained if Sgr A* is the external X-ray source to produce the 6.4 keV clumps. The surface brightness of fluorescent X-rays is faint at the near and far sides of the cloud-limb because of small $N_{\rm H}$ values, but becomes brighter when the external X-rays go into the large $N_{\rm H}$ ($\geq 10^{23}$ H cm^{-2}) region in the MCs. Another possible reason of the faint 6.4 keV-line flux at the far-side cloud limb from Sgr A* is due to the time variability of the Sgr A* X-rays; an X-ray front of possible X-ray outbursts about 300 years ago (Koyama et al. 2008; Inui et al. 2009) does not yet reach at the far-side limb of $l \sim 0.^\circ 85$.

Most of the CS MCs near Sgr B show positive velocities of 0–100 km s^{-1}. From spatial comparison between individual 6.4 keV clumps and the CS (J=1→0) maps in different velocity ranges (Tsuboi et al. 1999), we can roughly estimate that Sgr B2, Sgr B1, M 0.74−0.09, and M 0.74-sub lie in the velocities of +50 (40–80) km s^{-1}, +30 (20–40) km s^{-1}, +50 (40–60) km s^{-1}, and +50 (30–80) km s^{-1}, respectively.

Chapter 5

Study of Sagittarius C

In this chapter, we study the X-ray reflection nebulae (XRNe) in the Sgr C region and testify the spectral model proposed in Sgr B (chapter 4). We investigate the short-term time variability of the 6.4 keV line. We also establish the spectral composition for the Galactic center plasma emission.

Contents

5.1 Observation 65

5.2 Data Analysis and Results 66

5.2.1 Images 66

5.2.2 Spectral Model 68

5.2.3 Spectral Fitting 69

5.3 Discussion for Sgr C 73

5.3.1 Association with the Radio MCs 73

5.3.2 Two-temperature Structure of the GC Plasma and the XRN Parameters 74

5.3.3 Time Variability of the 6.4 keV Line and the Flare Property of Sgr A* 75

5.1 Observation

The Sgr C complex is composed of several giant molecular clouds located at $l \sim 0.5^\circ$, on the opposite side of Sgr B with respect to Sgr A*. We have made two deep pointing observations on the Sgr C region separated by ∼5 years between February 2006 and September

2010. These observations are conducted using the Suzaku/XIS. We operated the XIS in the normal clocking mode with a read-out cycle of 8 s. The details of Suzaku and XISs are given in chapter 2. The observation log of the Sgr C data for spectral analysis is shown in table 5.1. Information on archive data of other relevant GC regions used for image construction can be found in Uchiyama et al. (2011).

Table 5.1—: Suzaku Observations at the Sgr C Region.

Target name	Obs. ID	Obs. point (FOV center) α (J2000)	δ (J2000)	Obs. date (yy-mm-dd)	Effective exposure
Sgr C	500018010	$17^{\mathrm{h}}44^{\mathrm{m}}37.30^{\mathrm{s}}$	$-29°28'10.''2$	2006-02-20	106.9 ks
Sgr C	505031010	$17^{\mathrm{h}}44^{\mathrm{m}}58.01^{\mathrm{s}}$	$-29°22'51.''2$	2010-09-25	82.6 ks

5.2 Data Analysis and Results

We performed the data reduction and analysis using HEADAS software version 6.12. The calibration database used to calculate the response of XIS and the effective area of XRT was the version released on 2011-02-10. The screening for the XIS data were performed in the same way as those of Sgr B (described in section 4.1). The FI spectra were merged in the spectral fitting, and the NXB was subtracted from the raw data. The XRT vignetting effects and the exposure-time differences were corrected.

5.2.1 Images

We constructed the XIS images of the Sgr C region with the 6.4 keV-line (Fe I), the 6.7 keV-line (Fe XXV), and the 2–3 keV bands (see figure 5.1). The images were generated by adding data from multiple observations together (c.f., table 5.1 and Uchiyama et al. 2011) to cover a wide region near Sgr C. In addition, the FI and BI data were combined to increase the statistics. For the 6.4 keV and 6.7 keV line images, the fluxes underlying the continuum were estimated from the 5–6 keV band and subtracted from the 6.3–6.5 and 6.6–6.8 keV bands, respectively. Details of the subtraction procedures are explained in Nobukawa et al. (2010).

Figure 5.1a displays many bright clumps in the 6.4 keV-line band near Sgr C. These are spatially associated with giant MCs (see figure 5.1c) as observed in the radio CS (J=1→0) line by Tsuboi et al. (1999). We designate the brightest three 6.4 keV clumps: C1, C2, and

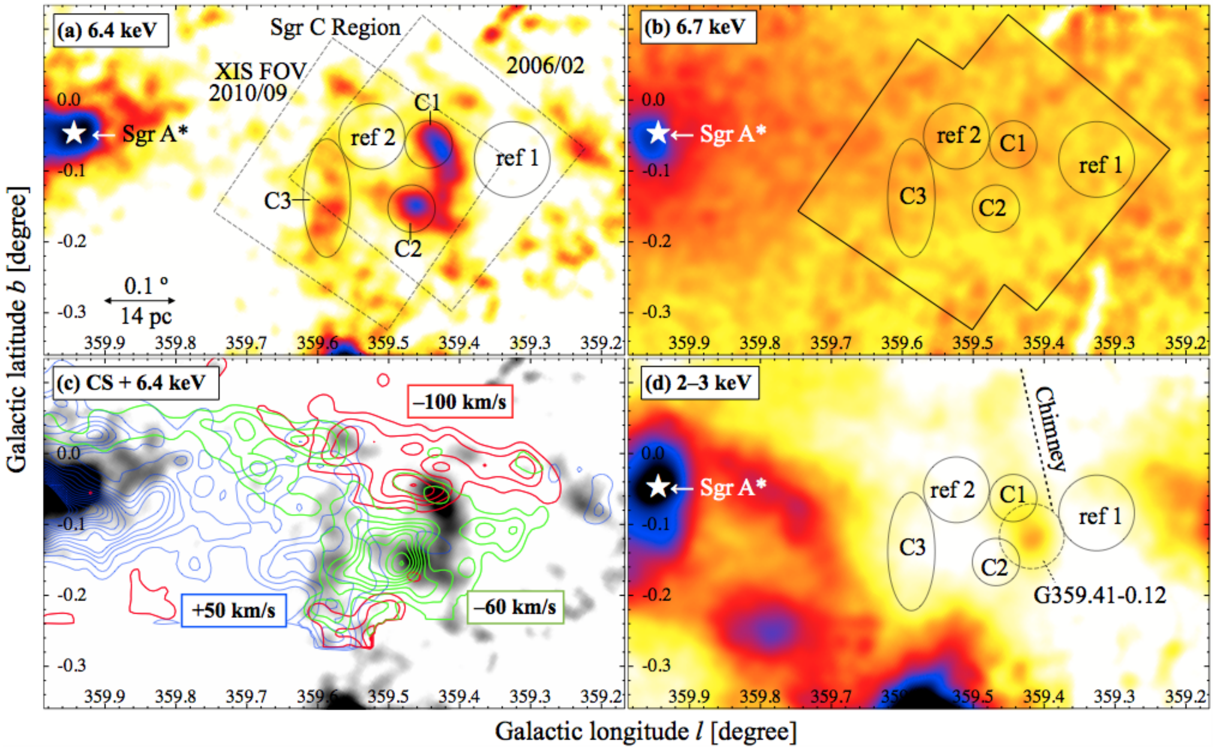

Fig. 5.1.—: Added XIS (FI+BI) images near the Sgr C region. The images are binned with 12×12 pixels and smoothened with a Gaussian kernel of $5''$. (a) 6.4 keV line (Fe I) image obtained by subtracting the continuum component (see text) from the 6.3–6.5 keV band flux. The XIS field of views (FOV) of the 2009 and 2006 observations are represented by the large boxes. The regions for spectral analyses (C1–3, ref 1–2) are indicated by solid circles. (b) Same as panel (a), but for the 6.7 keV line (Fe XXV) image. (c) 6.4 keV line image (gray) with the superposed radio CS (J=1→0) contours (Tsuboi et al. (1999)) in the velocity range of -100 ± 20 km s^{-1} (red), -60 ± 20 km s^{-1} (green), and $+50 \pm 30$ km s^{-1} (blue). The contour level begins at the intensity of 5 K km s^{-1} and increases every 5 K km s^{-1}. (d) Same as panel (a), but for the 2–3 keV band image (color). The region of G359.41−0.12 in Tsuru et al. (2009) is represented by the dashed circle.

C3 (solid circles; figure 5.1a). The clumps C1 and C2 were previously identified as XRNe by Nakajima et al. (2009), while C3 is a new XRN candidate revealed in the 2010 observation.

Figure 5.1b (the 6.7 keV line image) traces the high-temperature plasma (HP) of the GCPE (section 3.2), and shows a more uniform distribution than the 6.4 keV emission shown in figure 5.1a. Figure 5.1d shows the 2–3 keV band image including the 2.45 keV line (S XV) and displays the distribution of the low-temperature plasma (LP) and individual thermal diffuse sources, mainly supernova remnants candidates, with temperatures of $kT \sim 1$ keV. The faint diffuse sources near the Sgr C clumps are the supernova remnants G359.41−0.12

and its outflow "Chimney" (Tsuru et al. 2009). To investigate the nature of the GCPE (HP and LP), we selected two regions with relatively weak 6.4 keV emission for spectral analyses, and designate them as ref1 and ref2 (solid circles; figure 5.1a, b, and d).

5.2.2 Spectral Model

The X-ray spectra of the GC region have been extensively studied in chapter 4 and Uchiyama et al. (2012). The spectra can be reproduced by the superposition of four components: the GCPE, the XRN emissions (XRNE), the foreground emission (FE), and the cosmic X-ray background (CXB). These components have the following properties. The GCPE has two-temperature plasmas with kT∼1 keV and kT∼7 keV for LP and HP, respectively. The XRNE is expressed as neutral ion lines (Kα and Kβ) associated with a power-law component. Since the XRNE is formed by Thomson scattering of a continuum component and fluorescence of iron atoms in the MCs, it shows a large absorption (Abs1) of $N_{\mathrm{H}} \sim 10^{23}$ H cm^{-2} (e.g., Murakami et al. 2001), which is approximately equal to the N_{H} through the MC. The GCPE including the HP and LP is extended in the GC region, and the MC is inside this region. Thus, a fraction (R) of the X-ray from the GCPE is not absorbed by the MC while the other fraction ($1-R$) is absorbed by the MC (Abs1). Both GCPE and XRNE exhibit an common interstellar absorption (Abs2) of $N_{\mathrm{H}} \sim 6 \times 10^{22}$ H cm^{-2} between the GC and the sun (see chapter 4; Sakano et al. 2002). The FE is approximated to a thermal plasma of kT∼1 keV with small absorption. The CXB (e.g., Kushino et al. 2002) has the absorption of Abs2 by twice (interstellar absorption in front of and behind the GC), in addition to Abs1 (MC). Thus, the spectral model can be expressed by equation (5.1). A schematic picture of this model is shown in figure 5.2.

$$\begin{aligned} f(E) = {} & [\mathrm{Abs1} \times \mathrm{Abs2} \times (1-R) + \mathrm{Abs2} \times R] \times (\mathrm{HP} + \mathrm{LP}) \\ & + [\mathrm{Abs1} \times \mathrm{Abs2}] \times \mathrm{XRNE} \\ & + [\mathrm{Abs1} \times \mathrm{Abs2} \times \mathrm{Abs2}] \times \mathrm{CXB} + \mathrm{FE} \end{aligned} \tag{5.1}$$

In chapter 4, we successfully applied this model to the X-ray spectra of the 6.4 keV clumps near Sgr B. In addition, Muno et al. (2004) and Nobukawa et al. (2010) reproduced the X-ray spectra of Sgr A regions with similar models. Therefore, we apply the same model to the Sgr C region. In figure 5.3, we show a simulated spectrum (XIS/FI; 0.5–10.0 keV) with the typical GC parameters (see caption). The plasma emission code used in this chapter is APEC[1] and the absorption is evaluated in solar abundances[2].

---

[1] Astrophysical Plasma Emission Code: A model of an emission spectrum from diffuse gas in collisionally-ionized equilibrium (Smith et al. 2001).

[2] The solar abundance in this chapter is referred to the values from Anders & Grevesse (1989).

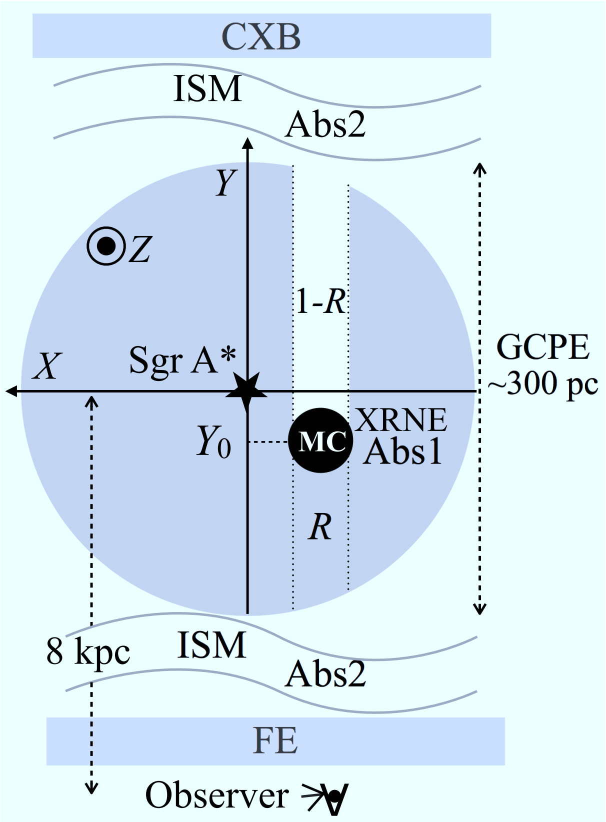

Fig. 5.2.—: A schematic face-on view for line-of-sight alignment. Coordinates X, Z, and Y correspond to directions of l, b, and line of sight, with respect to Sgr A*.

5.2.3 Spectral Fitting

As shown figure 5.5, we extract seven spectra from five regions (solid circles in figure 5.1). The spectra of C1 and C2 are obtained twice in the observations of 2006 and 2010, whereas C3 is only observed in 2010. All spectra are simultaneously fitted in the band of 0.5–10.0 keV with the model given in equation (5.1). Since the spectral model is highly complicated with many physical parameters, it is impractical to fit the data with all parameters free. Therefore, we adopt several reasonable constraints in the fitting. The parameter settings are the same as those in Sgr B (chapter 4). The FE is fixed to an APEC model with $\mathrm{k}T$=0.85 keV and abundance of Z=0.011, applied by small absorption of N_{H}=0.17×10^{22} H cm^{-2} (chapter 4). The center energy of the Fe Kα and Kβ lines are respectively fixed to 6.4 keV and 7.05 keV with the flux ratio (Kα/Kβ) of 0.125 (Kaastra & Mewe 1993). The temperature of the HP ($\mathrm{k}T_{\mathrm{HP}}$) is fixed to 6.5 keV (Koyama et al. 2007b), and the abundances of HP and LP are fixed to one solar ($Z = 1$). The parameter α, normalization ratio of HP/LP, can be approximated to a constant near Sgr C. This estimation is inferred from results of Uchiyama et al. (2012)

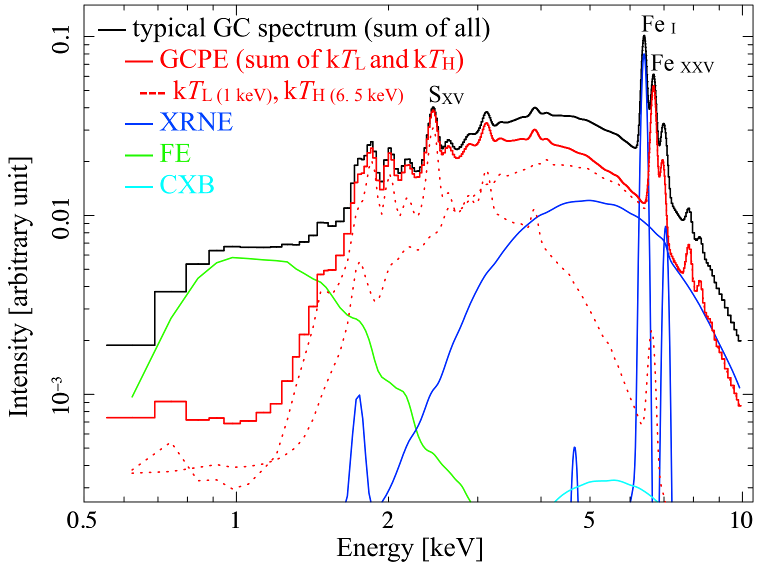

Fig. 5.3.—: Simulated XIS/FI spectrum with typical GC parameters reported in chapter 4. Model components of GCPE (k$T_{\rm LP}$ =1 keV, k$T_{\rm HP}$ =6.5 keV, α=0.27, R=0.5), XRNE ($EW_{6.4\ \rm keV}$=1.6 keV, Γ=1.7), FE, and CXB are shown in red, blue, green, and cyan lines, respectively. The column densities of Abs1 and Abs2 are set to 10×10^{22} H cm^{-2} and 6×10^{22} H cm^{-2}, respectively.

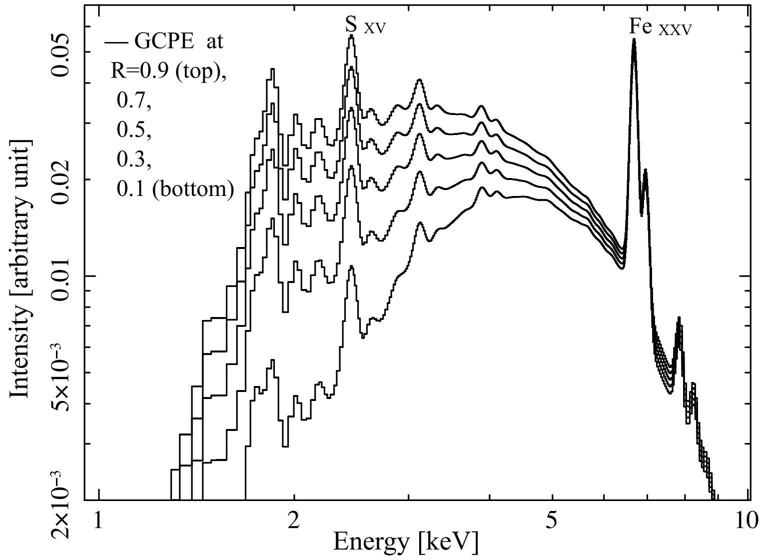

Fig. 5.4.—: Simulated XIS-FI spectra of the GCPE (k$T_{\rm L}$ =1 keV, k$T_{\rm H}$ =6.5 keV, α=0.27, $N_{\rm H}$(Abs1)=10×10^{22} H cm^{-2}, $N_{\rm H}$(Abs2)=6×10^{22} H cm^{-2}) for the parameter R from 0.1 to 0.9.

(c.f., figure 3 and table 2 therein), which indicate that the two plasmas exhibit nearly the same spatial distribution with an e-folding length of ~0.°6.

After all, the free parameters are the temperature of LP ($kT_{\rm LP}$), the normalization ratio of HP/LP (α= $\mathrm{norm}_{\rm HP}/\mathrm{norm}_{\rm LP}$), the photon index ($\Gamma$) of the power law, and the equivalent width of the 6.4 keV line with respect to the power-law continuum ($EW_{6.4~\rm keV}$); these free parameters are linked in all regions including C1–3 and ref1–2. These settings are designed to verify a common and consistent XRN model. Other parameters, such as line intensity ($I_{6.4~\rm keV}$) and absorption ($N_{\rm H}$), are free and independent for each region. To investigate the time variability for C1 and C2, the 6.4 keV intensities of the 2006 and 2010 spectra are set as free parameters, while other parameters are common between the two spectra.

As is seen in figure 5.1b, C1 is entirely overlapped with the "Chimney", which is a thermal plasma outflowing from G359.41−0.12. In order to include the Chimney contamination, we add the spectral model with fixed parameters (kT, $N_{\rm H}$, Z) reported in Tsuru et al. (2009). The flux (normalization of Chimney) is calculated from the average surface brightness and the region size of C1 (radius=2.′0), which is 35% of the GCPE flux.

All seven spectra are generally reproduced by the model of equation (5.1) with a reduced χ^2/d.o.f of 3773/3031=1.26. The fitting results are shown in figure 5.5 and the best-fit parameters are listed in table 5.2. The large $EW_{6.4~\rm keV}$ of ~1.2 keV and the strong absorption ($N_{\rm H}$(Abs1)~ 10^{23} H cm^{-2}) agree with the XRN scenario for all the regions. The $N_{\rm H}$ of Abs2 are in the range of 5.0–6.5 $\times 10^{22}$ H cm^{-2}. These values are consistent with the interstellar medium (ISM) absorption toward the GC region (Nobukawa et al. 2010; Sakano et al. 2002). As for the time variability of the 6.4 keV line between the 2006 and 2010 observations, C1 exhibits a small increase of 8% at 2.9-σ level, while C2 shows no significant change (see figure 5.6).

For confirmation, we also apply independent fitting with free $EW_{6.4~\rm keV}$ parameters for each region. The spectra of C1, C2, and C3 show $EW_{6.4~\rm keV}$ of 1.1–1.5 keV, 1.1–1.6 keV, and 0.7–1.3 keV, respectively. These values are consistent with the fitting result when $EW_{6.4~\rm keV}$ is a common free parameter ($EW_{6.4~\rm keV}$=1.15–1.27 keV; table 5.2), and agree with the XRN scenario of large $EW_{6.4~\rm keV}$. However, the independent $EW_{6.4~\rm keV}$ fittings result in large statistical errors in the R parameters (about 2–4 times larger than those in table 5.2), which is not practical for determination of cloud positions and discussions in chapter 7. Thus, we adopt the fitting results with $EW_{6.4~\rm keV}$ as a common free parameter between the regions (table 5.2).

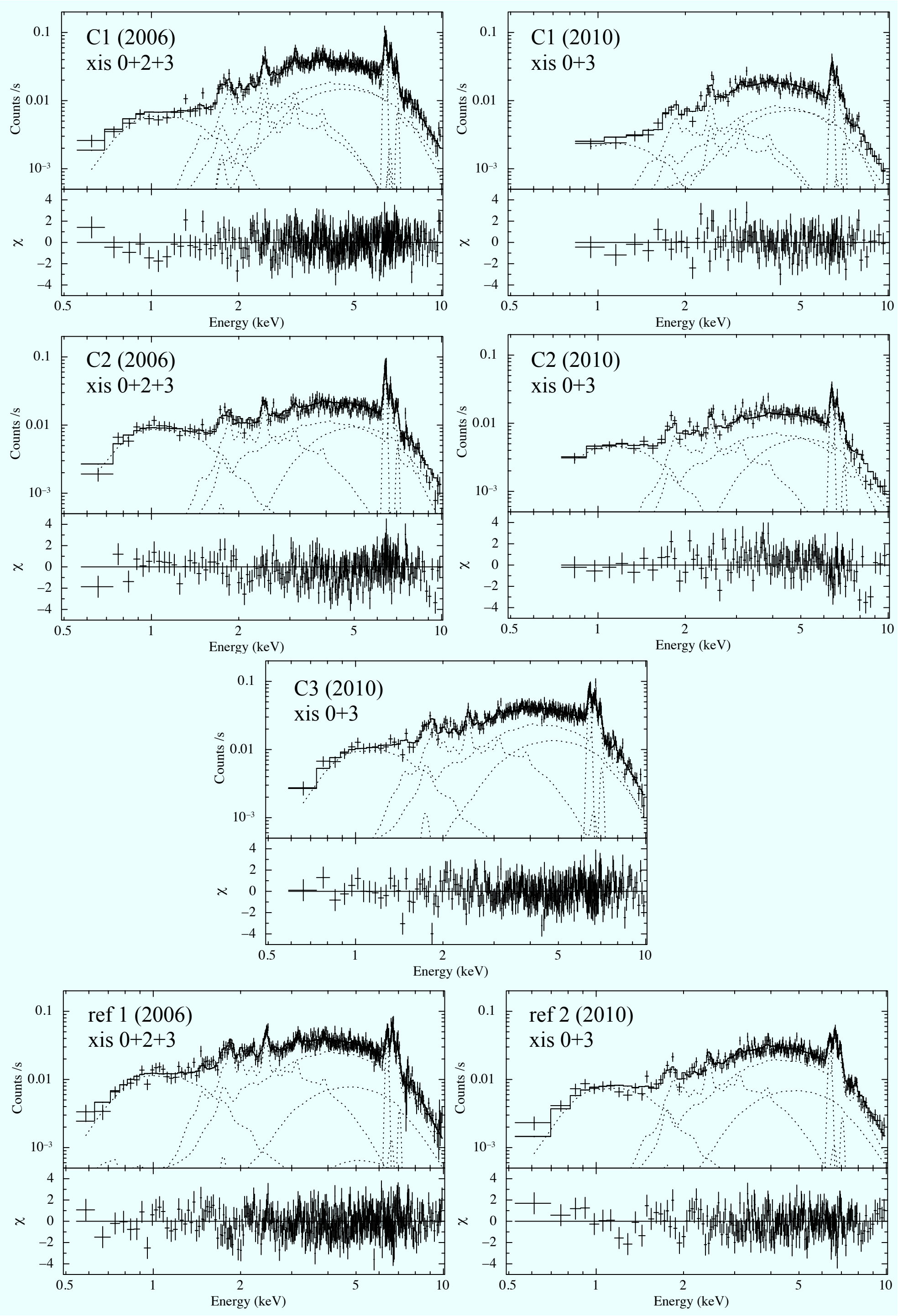

Fig. 5.5.—: Fitting results for all selected spectra (regions represented by black solid circles in figure 5.1a) near Sgr C. The FI (XIS 0+2+3 for 2006; XIS 0+3 for 2010) spectra with 1-σ error bars and the best-fit models (c.f., figure 5.3) are represented with solid crosses and dashed lines, respectively. The best-fit parameters are summarized in table 5.2.

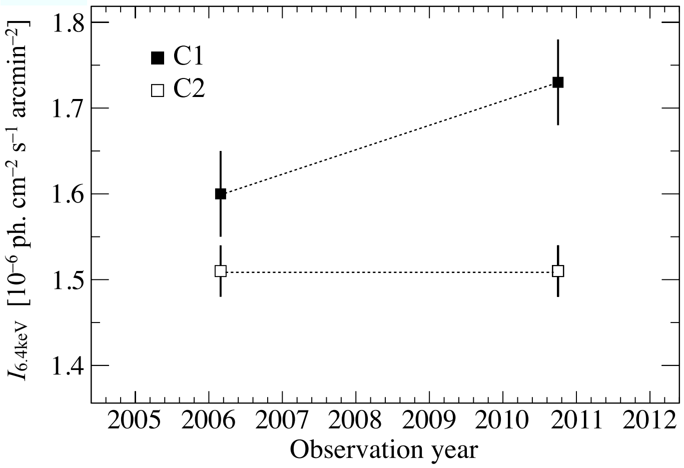

Fig. 5.6.—: Light curves (2006–2010) of the 6.4 keV intensity near Sgr C. Data points from C1 and C2 (c.f., table 5.2) are shown with the filled and open boxes, respectively.

5.3 Discussion for Sgr C

5.3.1 Association with the Radio MCs

The best-fit values of R (position indicator; see figure 5.2) are 0.23, 0.76, and 0.26 for C1, C2, and C3, respectively (table 5.2). These results indicate that C1 and C3 are in foreground to whereas C2 is beyond Sgr A*; they are largely separated in the line-of-sight positions, although proximately located at the projected distance. We search for the radio counterparts of C1, C2 and C3 from the CS (J=1→0) maps (Tsuboi et al. 1999) in different velocity ranges from -250 km s^{-1} to 250 km s^{-1}. As shown in figure 5.1c, C2 and C3 are respectively in good coincidence with MCs in the velocity ranges of -60 ± 20 km s^{-1} and $+50\pm30$ km s^{-1}. On the other hand, C1 is observed in the two separated velocity ranges of -60 ± 20 km s^{-1} and -100 ± 20 km s^{-1}. Using the data corresponding C2 and C3, we derived a conversion factor between the X-ray column density (Abs1; table 5.2) and the integrated CS intensity (contours; figure 5.1c), which is [CS/N_{H}] $\simeq 2.5$ [K km s^{-1}/(10^{22} H cm^{-2})]. The X-ray N_{H} of MC (Abs1) used in this study is determined directly from the absorption of GCPE continuum behind the cloud (c.f., figure 5.2). This method is available even if the MC is not an XRN, and thus does not depend on the properties of the illuminating source. Assuming the same [CS/N_{H}] factor near Sgr C, the observed X-ray column density of C1 (6.0–6.8$\times10^{22}$ H cm^{-2}; table 5.2) indicates a CS intensity of 15–17 K km s^{-1}. This generally excludes the -60 km s^{-1} MC as the counterpart of C1, because the average CS intensity is only 5–10 K km s^{-1}. The -100 km s^{-1} MC has a CS intensity of 10–25 K km s^{-1}, which

Table 5.2—: Best-fit spectral parameters of the Sgr C regions[*].

Local parameters

Region	Obs.Yr	$N_{\mathrm{H}}^{\dagger}$ (Abs1)	$N_{\mathrm{H}}^{\dagger}$ (Abs2)	$I_{6.4\ \mathrm{keV}}{}^{\ddagger}$	FE norm§	GCPE norm$_{\mathrm{LP}}{}^{\parallel}$	Fraction $R^{\#}$
C1	2006	$6.5^{+0.3}_{-0.5}$	$5.1^{+0.3}_{-0.3}$	$1.60^{+0.05}_{-0.05}$	$0.060^{+0.004}_{-0.004}$	$3.0^{+0.1}_{-0.1}$	$0.23\ ^{+0.03}_{-0.04}$
	2010			$1.73^{+0.05}_{-0.05}$			
C2	2006	$11.4^{+1.6}_{-1.4}$	$6.5^{+0.3}_{-0.2}$	$1.51\ ^{+0.03}_{-0.03}$	$0.100^{+0.005}_{-0.005}$	$2.0^{+0.1}_{-0.1}$	$0.72^{+0.12}_{-0.03}$
	2010			$1.51^{+0.03}_{-0.03}$			
C3	2010	$8.7^{+0.4}_{-0.6}$	$5.0^{+0.3}_{-0.2}$	$1.16^{+0.05}_{-0.05}$	$0.082^{+0.005}_{-0.003}$	$3.0^{+0.1}_{-0.1}$	$0.26^{+0.03}_{-0.03}$
ref1	2006	$7.9^{+0.5}_{-0.8}$	$5.3^{+0.2}_{-0.1}$	$0.36^{+0.03}_{-0.04}$	$0.059^{+0.003}_{-0.003}$	$2.3^{+0.1}_{-0.1}$	$0.40^{+0.04}_{-0.03}$
ref2	2010	$7.6^{+0.5}_{-0.7}$	$6.4^{+0.4}_{-0.3}$	$0.78^{+0.05}_{-0.05}$	$0.082^{+0.006}_{-0.006}$	$3.3^{+0.1}_{-0.1}$	$0.31^{+0.05}_{-0.05}$

Global parameters

kT_{LP}	α ratio $\left(\frac{\mathrm{norm_{HP}}}{\mathrm{norm_{LP}}}\right)$	$EW_{6.4\ \mathrm{keV}}$	Photon index Γ
$0.92^{+0.03}_{-0.05}$ keV	$0.28\ ^{+0.01}_{-0.05}$	$1.19^{+0.08}_{-0.04}$ keV	$1.63^{+0.08}_{-0.09}$

$\chi^2/\mathrm{d.o.f}^{**} = 3773/3031 = 1.26$

[*] The spectral regions are shown in figure 5.1. The uncertainties are at 90% confidence level (statistical).

[†] The value of column density in the unit of $10^{22}\,\mathrm{H\,cm^{-2}}$.

[‡] Intensity in the unit of 10^{-6} photons $\mathrm{cm^{-2}s^{-1}arcmin^{-2}}$.

[§] The normalization factor of the APEC model for the foreground emission. It is normalized with the region size A [arcmin^2] and expressed as $7.07 \times 10^{-13}/(4\pi D^2 A)\,EM$ [$\mathrm{cm^{-5}arcmin^{-2}}$], where D and EM are the distance to the source [cm], and the emission measure [cm^{-3}], respectively.

[‖] In the same expression as §, but the normalization factor of LP in the GCPE.

[#] R is the fraction of the GCPE not absorbed by MC (see equation (5.1) and figure 5.2), which is the indicator of the line-of-sight position for XRNe).

[**] The results are obtained by the simultaneous fitting of the 14 spectra from the FI and BI data.

is in agreement with the N_{H} estimated by the X-ray data. Thus, C1 is most likely to be situated in the velocity range of -100 ± 20 km s^{-1}.

5.3.2 Two-temperature Structure of the GC Plasma and the XRN Parameters

The best-fit temperature of LP (kT_{LP}) and the mixing ratio ($\alpha = \mathrm{norm_{HP}}/\mathrm{norm_{LP}}$) in the GCPE at Sgr C are 0.87–0.95 keV, and 0.23–0.29, respectively. These values are nearly equal to those in Sgr B region: kT_{LP} =0.81–0.91 keV and α =0.26–0.28 (chapter 4)). Sgr C and Sgr B are located at nearly the symmetrical positions with respect to Sgr A* on the Galactic plane, and hence these results indicate that the GCPE distribution is symmetrical not only in the flux profile (Uchiyama et al. 2012) but also in the spectral shape.

The photon index and $EW_{6.4\,\mathrm{keV}}$ for the 6.4 keV clumps in Sgr C are 1.54–1.71 and 1.15–1.27 keV, respectively (table 5.2). These values are approximately equal to the Sgr B results (chapter 4). The large *EW* is in favor of the X-ray reflection and fluorescent origin (e.g., Koyama et al. 1996; Murakami et al. 2001; section). The photon index is consistent with canonical low-luminosity active galactic nuclei (AGN; e.g., Ishisaki et al. 1996; Terashima & Wilson 2001), which favors the XRN scenario owing to the past flare of Sgr A*.

5.3.3 Time Variability of the 6.4 keV Line and the Flare Property of Sgr A*

Since the discovery of the neutral iron (6.4 keV) line near Sgr B as the X-ray echo of the SMBH (Koyama et al. 1996), one basic question has been asked that whether it was a single flare from Sgr A*. As the solid observational facts by the same instrument (Suzaku/XIS), Nobukawa et al. (2011) detected the decrease of the 6.4 keV intensity in Sgr B (Sgr B2 and M 0.74$-$0.09) by a factor of 2.0–2.5 from 2005 to 2009. In contrast, our data show that the 6.4 keV intensity in Sgr C1 and C2 is stable or slightly increasing in 2006–2010. The Sgr B results suggest a flare to be shorter than 4 years, while the Sgr C results require a flare duration longer than 4 years. Hence, these are unlikely due to a same flare. In addition, XMM-Newtoon (Ponti et al. 2010) found the superluminal motion, flux increase and decrease within a ∼15-ly region, propagating near Sgr A ($0.^\circ0 < l < 0.^\circ2$) in 2002–2009. In summary, although observed in the same years, the 6.4 keV emission (X-ray echoes) around the GC region shows different time behaviors, which are difficult to be explained by the Sgr A* luminosity at a same time in the past. The most direct verification for the single-flare (or multiple-flares) scenario is to see whether all XRNe around the GC are lying near a single parabola with focus at Sgr A*, from the face-on view (c.f., figure 2.22). We will discuss it in the chapter 7.

Chapter 6

Study of Sgr D & Sgr E

In this chapter, we apply the model developed in Sgr B and Sgr C (chapter 4 and chapter 5) to the Sgr D and Sgr E regions located near the edges of the central molecular zone (CMZ; section 2.1.2). We probe and investigate the farthest molecular clouds from the GC for the 6.4 keV emissions.

Contents

6.1 Observation 77
6.2 Data Analysis and Results 78
6.2.1 Images 78
6.2.2 Spectra 78
6.3 Discussion for Sgr D and Sgr E 80
6.3.1 Association with the Radio MCs 80
6.3.2 Origin of the 6.4 keV Line 81

6.1 Observation

The Sgr D and Sgr E regions, located at the contrary GC sides of $l \sim 1.^\circ 2$ and $-1.^\circ 2$, are bright in CO and/or CS emissions (e.g., Oka et al. 1998; Tsuboi et al. 1999), which suggest molecular clouds at the boundary of the CMZ. Suzaku had two pointing observations with XIS in normal mode to Sgr D region on March 2007 and Sgr E on September 2008, respectively. The observation log is shown in table 6.1.

Table 6.1—: Suzaku Observations near the Sgr D and Sgr E Regions.

Target name	Obs.ID	Pointing direction*		Obs.date	Exposure
		α (J2000.0)	δ (J2000.0)	(yyyy-mm-dd)	(ks)
GC Sgr D	501059010	$17^{\mathrm{h}}48^{\mathrm{m}}21.^{\mathrm{s}}91$	$-27°56'08.''1$	2007-03-15	98.3
GC_LP7 (Sgr E)	503013010	$17^{\mathrm{h}}42^{\mathrm{m}}41.^{\mathrm{s}}85$	$-30°04'13.''4$	2008-09-16	50.1

*The center of the XIS field of view.

6.2 Data Analysis and Results

In the generation of images and spectra for Sgr D and Sgr E, the screening and reduction for the XIS data were performed in the same way as those of Sgr B (described in section 4.1). The FI spectra were merged in the spectral fitting, and the NXB was subtracted from the raw data. In the following analyses, the software was HEADAS version 6.12 and the calibration database was the version released on 2011-02-10.

6.2.1 Images

In figure 6.1, we show the X-ray band images near the Sgr D and Sgr E regions. The 6.7 keV maps (figure 6.1 middle), tracing the large-scale high-temperature (HP: $k_{\mathrm{B}}T\approx$6.5 keV; Koyama et al. 2007c) plasma, basically show uniform distribution in the XIS FOVs. Similarly, the 2–3 keV maps (figure 6.1 top), tracing the low-temperature (LP: $k_{\mathrm{B}}T\sim$1 keV) plasma, is featureless except for the local diffuse sources reported by Sawada et al. (2009).

From the 6.4 keV maps (figure 6.1 bottom), we discovered clumpy structures both in the Sgr D and Sgr E FOVs; hereafter, we simply call them "Clump D" and "Clump E". Clump D and Clump E have angular sizes of $\sim10'$ and $\sim5'$, which are much more extended than the point spread function of XRT/XIS ($\sim1.8'$; see figure 3.7). Thus, these 6.4 keV emissions should have diffuse origin and are probably associated with molecular clouds (MCs), from our experiences in the Sgr B and Sgr C regions.

6.2.2 Spectra

In order to investigate the details of new 6.4 keV clumps found in the Sgr D and Sgr E regions, we extract spectra from the two circular regions shown in figure 6.1 bottom; the

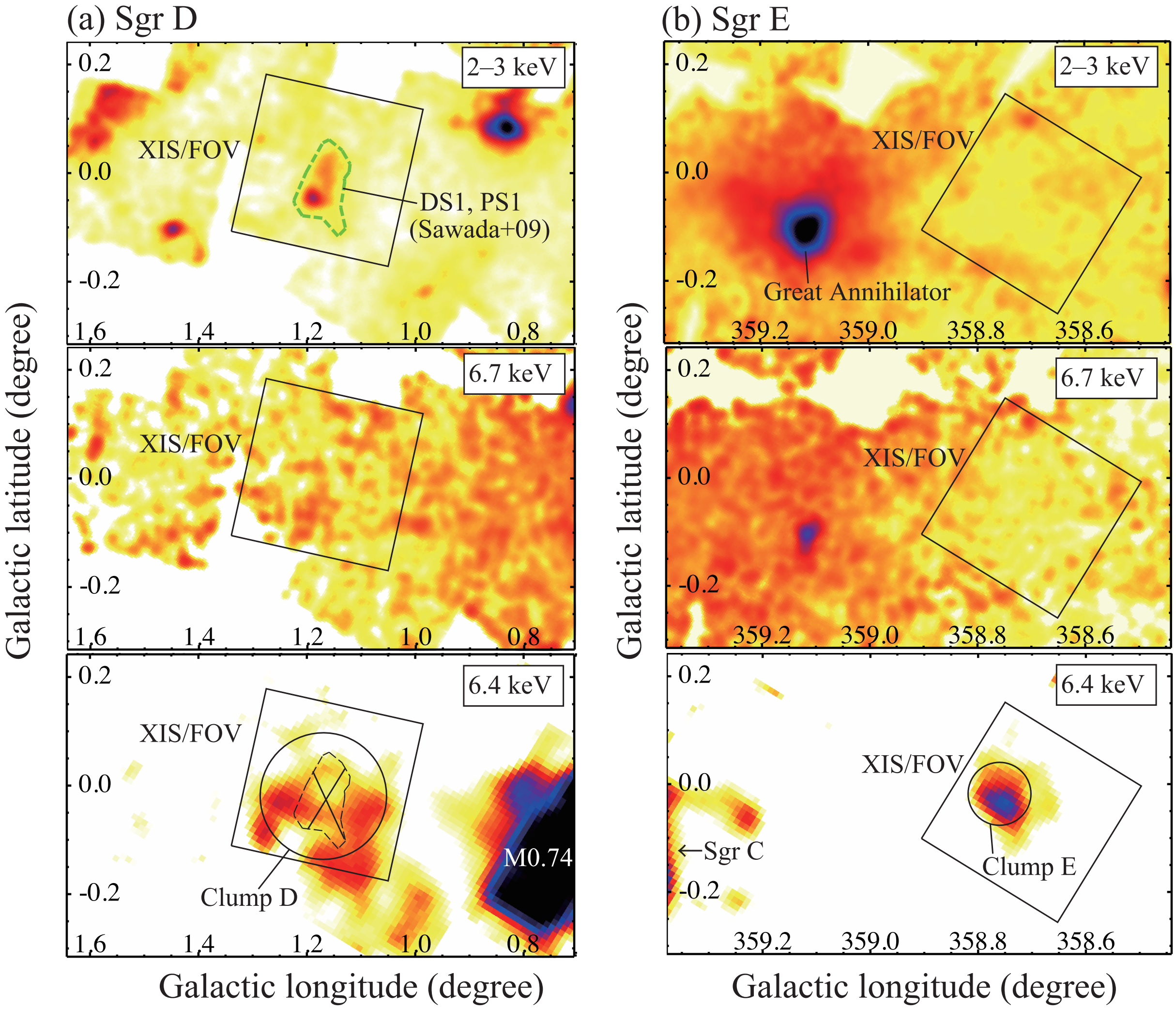

Fig. 6.1.—: X-ray band images of the (a) Sgr D and (b) Sgr E regions by Suzaku/XIS. The bin size of images is $\sim 1'$. The top, middle, and bottom panels represent images of the medium band (2–3 keV; S XV and continuum), the 6.7 keV (Fe XXV) line, and the 6.4 keV (Fe I) line, respectively. The 6.4 keV- and 6.7 keV- line images are intensity maps constructed from the 6.3–6.5 keV band and the 6.5–6.8 keV band, respectively, after continuum subtractions. The XIS field of views (FOV) of the data analyzed in this chapter (table 6.1) are represented by the large solid boxes. The regions for spectral analysis (Clump D and Clump E) are indicated with solid circles; the bright sources in Sgr D ((a) top; DS1 and PS1; Sawada et al. 2009) are excluded using the region shown with the dashed lines.

region containing local sources in Sgr D (DS1 and PS1; see figure 6.1a middle) are excluded. We apply the spectral model developed in Sgr B and Sgr C (c.f., equation (5.1) and figure 5.2) to the spectra of Clump D and Clump E. The temperature of LP, temperature of HP, and the normalization ratio (HP/LP) are fixed to $k_{\rm B}T$=0.9 keV, $k_{\rm B}T$=6.5 keV, and $\alpha = 0.27$, respectively. The temperature and absorption of the foreground emission (FE) and the photon index of the continuum ($\Gamma = 1.7$) are also fixed to the results obtained in Sgr B and Sgr C. Other parameters are free in spectral fitting. We set the equivalent width at 6.4 keV ($EW_{6.4\ \rm keV}$) as free parameters to testify the X-ray reflection process for each region. As shown in figure 6.2, the spectra of Clump D and Clump E are well reproduced by our spectral model with χ^2/d.o.f $\lesssim$ 1.2. The best-fit results are listed in table 6.2.

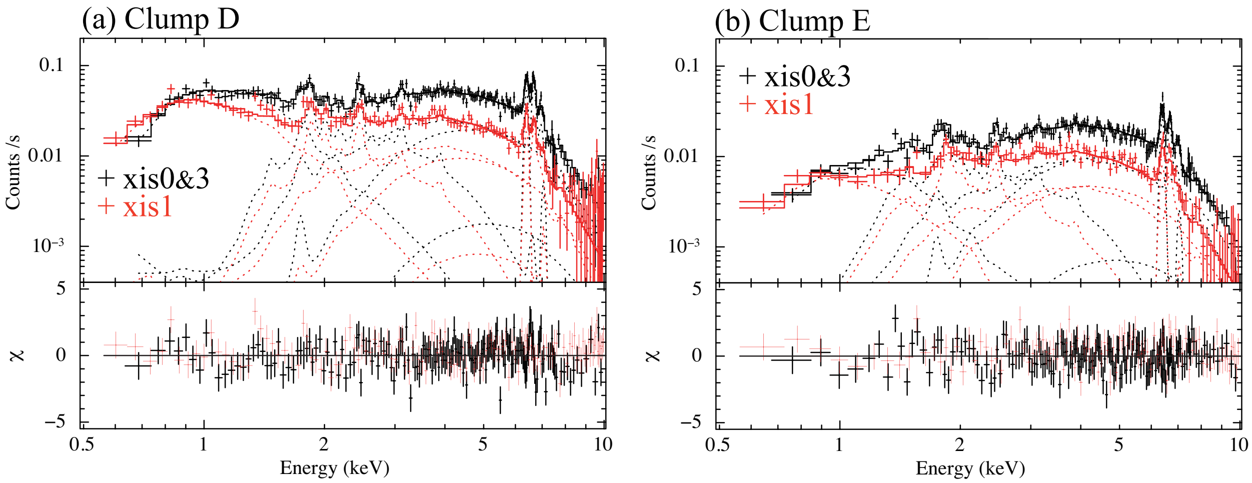

Fig. 6.2.—: XIS spectra of (a) Clump D and (b) Clump E (c.f., solid circles in figure 6.1 bottom). The FI and BI results are shown in black and red, respectively. The best-fit spectral models (c.f., figure 5.3) are shown in the dashed lines.

6.3 Discussion for Sgr D and Sgr E

6.3.1 Association with the Radio MCs

Strong absorption of $N_{\rm H}$~7×10^{22} H cm^{-2} (Abs1) is detected both from Clump D and Clump E, which should be due to the MCs lying in the line of sight. We look into the radio CO maps (Oka et al. 1998) in different velocity ranges to search for the MC counterparts. From the comparison between the CO and 6.4 keV maps in morphology, we identified two MCs in velocities near +100 km s^{-1} and −200 km s^{-1} that display good coincidence with clump D and clump E, respectively (figure 6.3). According to the CO maps (figure 6.3) and equation (2.3), the CO intensities of the counterparts in +110~+120 km s^{-1} and $-220\sim-210$ km s^{-1} suggest $N_{\rm H}\approx2N_{\rm H_2}$~4–$8\times10^{22}$ H cm^{-2} for Clump D and ~2–4×10^{22} H cm^{-2} for

Table 6.2—: Spectral fitting results of 6.4 keV clumps in Sgr D and Sgr E.

source	$N_{\rm H}^{\dagger}$ (Abs1)	$N_{\rm H}^{\dagger}$ (Abs2)	$I_{6.4}{}^{\dagger}$	FE§	GCPE§	$R^{\#}$	$EW^{\dagger}_{6.4 \text{ keV}}$
Clump D	$6.7^{+1.5}_{-1.0}$	$5.1^{+0.3}_{-0.3}$	$0.27^{+0.03}_{-0.03}$	$0.12^{+0.04}_{-0.04}$	$0.80^{+0.10}_{-0.10}$	$0.53^{+0.23}_{-0.18}$	$0.69^{+0.12}_{-0.11}$
			χ^2/d.o.f=278/258=1.08				
Clump E	$6.6^{+0.6}_{-0.6}$	$3.5^{+0.5}_{-0.4}$	$0.40^{+0.04}_{-0.03}$	$0.05^{+0.04}_{-0.04}$	$0.90^{+0.10}_{-0.10}$	$0.28^{+0.07}_{-0.08}$	$0.76^{+0.14}_{-0.11}$
			χ^2/d.o.f=348/299=1.16				

* The parameter uncertainties are at 90% confidence level.

† The values of absorption ($N_{\rm H}$), 6.4 keV intensity ($I_{6.4}$), and 6.4 keV equivalent width ($EW_{6.4 \text{ keV}}$) are in the units of $10^{22}\,{\rm H\,cm^{-2}}$, 10^{-6}photons cm^{-2}s^{-1}arcmin^{-2}, and keV, respectively.

§ The normalization factors of APEC models for the LP of the Galactic center plasma emission (GCPE) and the foreground emission (FE). The values are re-normalized with the region size A [arcmin^2], expressed as $7.07 \times 10^{-13}/(4\pi D^2 A) EM$ [cm^{-5}arcmin^{-2}], where D and EM are the distance to the source [cm], and the emission measure [cm^{-3}], respectively.

\# R is the fraction of the GCPE suffered by Abs2, which indicates the positions of MCs (c.f., equation (5.1) and figure 5.2).

Clump E, respectively. Although the above estimation contains uncertainties by a factor of ~ 2 due to the velocity range for integration, the $N_{\rm H}$ values by CO observations are basically consistent with the $N_{\rm H}$ values of MC measured from X-ray absorption (Abs1).

The $N_{\rm H}$ values of Abs2 are 3.5×10^{22} H cm^{-2} for Clump E and 5.1×10^{22} H cm^{-2} for Clump D, which are similar to pervious reports of Galactic ISM absorption at $|l| \sim 1^{\circ}$–$2.^{\circ}5$ (e.g., Sawada et al. 2009, 2011; Uchiyama et al. 2012). Also by taking the high velocities ($V_{\rm LOS} > 100$ km s^{-1}) into consideration, we conclude that the Clump D and Clump E are MCs located in the GC region, most likely as parts of the CMZ (c.f., section 2.1.2). The obtained R values, the position indicator (c.f., figure 4.7; section 4.3.2), suggest the line-of-sight placement that Sgr D ($R = 0.53$) lies slightly behind, while Sgr E ($R = 0.28$) is significantly in foreground to Sgr A*.

6.3.2 Origin of the 6.4 keV Line

The origin of the 6.4 keV emission can be inferred from the observed equivalent width ($EW_{6.4 \text{ keV}}$), which are 0.6–0.8 keV for Clump D and 0.7–0.9 keV for Clump E. In order to explain these $EW_{6.4 \text{ keV}}$ values, the required Fe abundance with respect to solar is 2.5–3 times in the electron process, or 0.6–0.9 times in the X-ray process (c.f., section 2.4.1). Local thermal sources near Sgr D show Fe abundance of less than 1 solar (Sawada et al. 2009) and the Galactic ridge emission at $|l| \sim 2^{\circ}$ shows sub-solar Fe abundance of 0.5–0.8 (Uchiyama et al. 2012; Sawada et al. 2011), which are consistent with the values of X-ray origin. Thus,

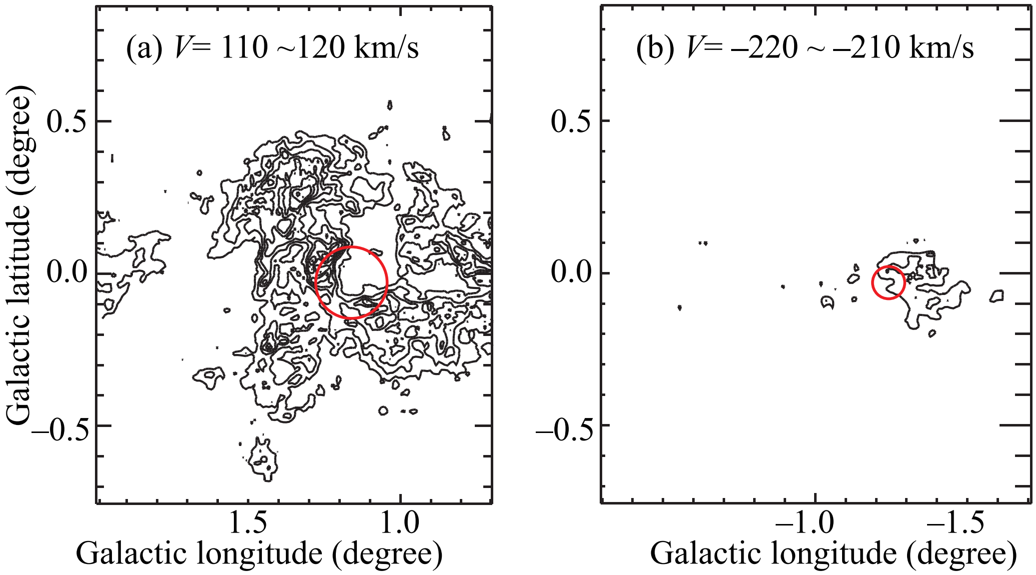

Fig. 6.3.—: Radio ^{12}C^{6}O ($J = 1 \rightarrow 0$) maps from Oka et al. (1998). (a) Sgr D region in velocity range of +110∼+120 km s^{-1}. (b) Sgr E region in velocity range of $-220 \sim -210$ km s^{-1}. Contours are set at intervals of 15 K km s^{-1}. The red solid circles represent the regions used for X-ray spectral analyses (c.f., figure 6.1. bottom)

we suggest that the 6.4 keV emissions from Clump D and Clump E are produced by X-ray reflections. These 6.4 keV clumps are the furthest X-ray reflection nebulae (XRNe) presently observed.

Chapter 7

Overall Results & Discussion

In this chapter, we summarise and analyse the results obtained in chapter 4–6. We quantitatively determine the line-of-sight positions for the XRNe in the GC region and discuss their three dimensional distributions in association with MCs in the CMZ. We finally derive an X-ray light curve for the activities of Sgr A* over the past six centuries.

Contents

7.1 Longitude Distribution of Physical Parameters 83

7.2 Face-on Distribution of XRNe in the GC Region 85

7.2.1 Computation of Line-of-sight Position 85

7.2.2 Association with the CMZ 90

7.3 Active History of Sagittarius A* 93

7.3.1 Derivation of X-ray Light Curve 93

7.3.2 Behaviours of the Past Flare State 94

7.3.3 Interpretation as Low-Luminosity AGN 97

7.1 Longitude Distribution of Physical Parameters

From the fitting results in chapter 4–6, we investigate the overall l distribution of physical parameters in the GC region. As shown in figure 7.1a, we can obtain a clear picture that the total absorptions toward the GC are separated into two kinds: Abs1 and Abs2. Abs1 displays nearly uniform distribution with average of $N_{\mathrm{H}} \approx 6 \times 10^{22}$ H cm^{-2}, which suggests its origin as the Galactic ISM between the GC and the Sun. The N_{H} values of Abs2 are comparable or higher than those of Abs1, which implies that Abs2 comes from the giant MCs (e.g., Sgr B2, Sgr C) in the CMZ. As shown in figure 7.1b, the l distribution of the GCPE basically follows the exponential model by Uchiyama et al. (2012), which is decaying from Sgr A* with an e-folding scale height of ∼0.°6. Thus, the overall distributions of the GCPE and its absorptions are self-consistent with the schematic picture we constructed in chapter 4 and 5 (see figure 4.4 and figure 5.2).

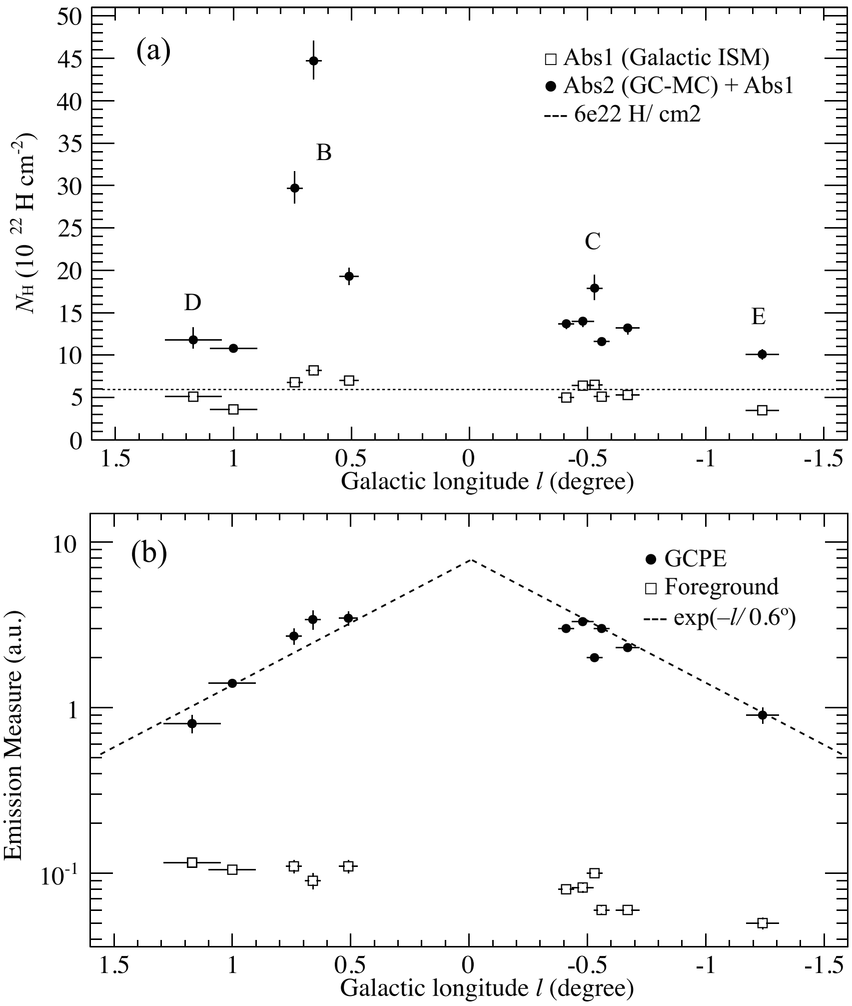

Fig. 7.1.—: Longitude (l) distribution of physical parameters in the GC. (a) Absorptions of the GCPE. (b) Emission measures of the GCPE and the foreground emission (FE). The values in the vertical axis are shown in arbitrary units (a.u.).

7.2 Face-on Distribution of XRNe in the GC Region

7.2.1 Computation of Line-of-sight Position

As illustrated in figure 5.2 and figure 4.4, the parameter R represents the line-of-sight position of XRN inside the GCPE; R is the fraction of the GCPE in front of the XRN with respect to the entire GCPE along the line-of-sight. Depending on the distance from Sgr A*, the GCPE is more or less contaminated by the Galactic ridge plasma emission (GRPE; section 2.3.1), which has a similar two-temperature spectral structure but a more extended spatial distribution (Uchiyama et al. 2012). In order to estimate the XRN positions numerically, we use the spatial distributions of these plasmas.

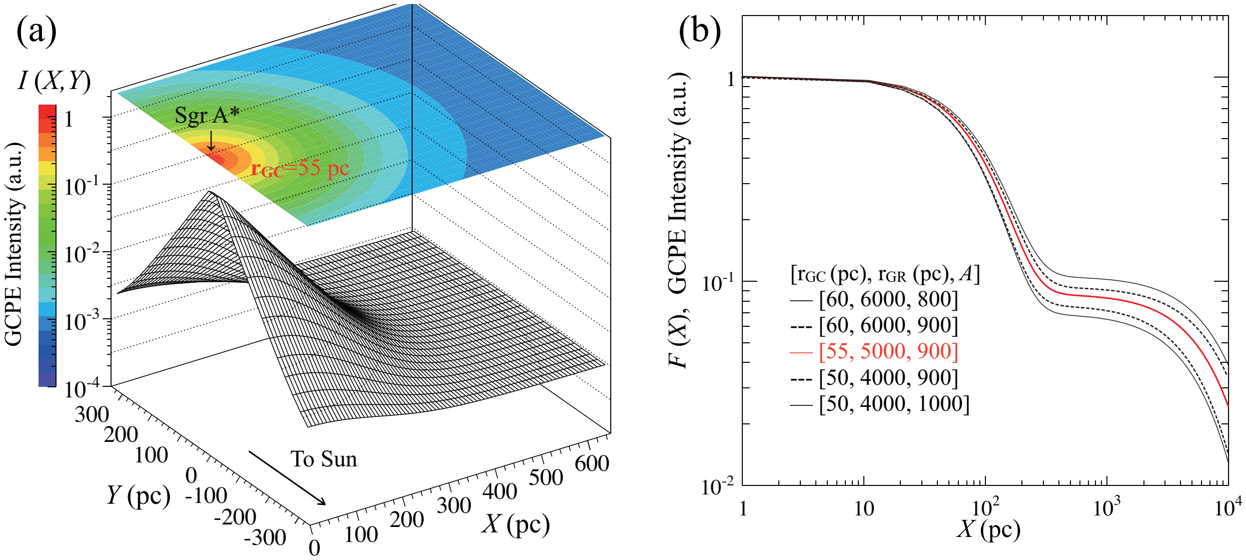

Fig. 7.2.—: (a) X-Y distribution of the GCPE, $I(X,Y)$ (see definition in text). (b) Profile of the GCPE along longitude (X-axis) calculated from integration of $F(X)=\int_{-\infty}^{\infty} I(X,Y)\,\mathrm{d}Y$. The red solid line represents the profile adopted for calculations of the line-of-sight positions. Other profiles with different parameters, corresponding to 10%, 20%, and 10% error ranges for $r_{\rm GC}$, $r_{\rm GR}$, and A in $I(X,Y)$, respectively, are also plotted to show model uncertainties estimated form the results of Uchiyama et al. (2012) (c.f., figure 2.17).

We introduce new coordinates (X,Y,Z) with origins at Sgr A* ($l=-0.^\circ056$, $b=-0.^\circ046$; Yusef-Zadeh et al. 1999), in which X, Z, and Y correspond to the directions of l, b, and line of sight, respectively (see figure 5.2). Because the relevant XRNe are all on or near the Galactic plane ($|b_{\rm XRN}-b_{\rm Sgr\ A*}|\leq 0.^\circ1$), we ignore the offset of Z, for simplicity, in the following calculations. Uchiyama et al. (2011) and Uchiyama et al. (2012) derived the X-axis flux distribution for many emission lines of ionized atoms (e.g., Fe and S) in addition to the soft and hard X-ray continuum bands. The data were fitted with a two-exponential function along the Galactic plane (X-axis): $F(X) = I_{\rm C}\exp(-X/l_{\rm C}) + I_{\rm R}\exp(-X/l_{\rm R})$. The values of e-folding length for HP and LP are similar to each other both in the GCPE and GRPE. In this paper, we adopted $l_{\rm C}$=0.°6, $l_{\rm R} = 50°$, and $I_{\rm C}/I_{\rm R}$=10 as the mean values (see table 2 in Uchiyama et al. 2012).

We assume that the X-Y plane distribution of the plasmas (see figure 7.2a) is an oblate spheroid expanded with two-exponential function as $I(X,Y) = A \times \exp(-r/r_{\rm GC}) + \exp(-r/r_{\rm GR})$, where $r = \sqrt{X^2+Y^2}$. A is the flux ratio (GCPE/GRPE), and $r_{\rm GC}$ and $r_{\rm GR}$ are the e-folding scale lengths of GCPE and GRPE, respectively. Integrating $I(X,Y)$ along the Y-axis as $F(X) = \int_{-8\,{\rm kpc}}^{\infty} I(X,Y)\,{\rm d}Y$, we find that the resultant projection of X-distribution is nearly the same exponential shape as those observed by Uchiyama et al. (2012). We then compare $F(X)$ with the results of Uchiyama et al. (2012) (figure 2.17) to match the shapes. The parameters are determined to be $r_{\rm GC}$=55 pc (or 0.°4), $r_{\rm GR}$=5000 pc (or 36°), and A=900. The uncertainties of these parameters, including statistical errors (at 90% C.L.) and systematical fluctuations between profiles in different bands from Uchiyama et al. (2012), are approximately 10%, 20%, and 10% for $r_{\rm GC}$, $r_{\rm GR}$, and A, respectively. In figure 7.2b, we show the results of numerical calculation for the GCPE profile $F(X)$ and its uncertainty ranges.

Considering that an XRN locating at (X_0,Y_0) and X_0 as its l offset from Sgr A*, the line-of-sight position (Y_0; c.f., figure 5.2) is a function of parameter R expressed in the following equation.

$$R(Y_0) = \frac{\int_{-8\,{\rm kpc}}^{Y_0} I(X_0,Y)\ {\rm d}Y}{\int_{-8\,{\rm kpc}}^{\infty} I(X_0,Y)\ {\rm d}Y} \tag{7.1}$$

In figure 7.3, we show examples of numerical calculation for the Y-R relation (equation (7.1)) at different X_0 positions, using the adopted spatial parameters of the GCPE and the GRPE ($r_{\rm GC}$, $r_{\rm GR}$, A; c.f., figure 7.2).

From the R values obtained in chapter 4–6 (table 4.4, table 5.2, table 6.2) and simulated Y-R curves, we determined the line-of-sight position (Y_0) for each XRN in Sgr B, Sgr C, Sgr D, and Sgr E. Here, the Y errors due to the uncertainties of the GCPE spatial parameters are $\leq$ 20 ly at a given R value in range of 0.2–0.8 (see black lines in figure 7.3), which are ignorable compared to the Y errors originated from statistical uncertainties of the best-fit R values (errors $\gtrsim$ 50 ly; table 7.1). Figure 7.4 illustrates the resultant face-on view of XRNe around Sgr A* on the X-Y plane. The units of (X,Y) are converted into the actual length of light year (ly). Detailed results are summarized in table 7.1.

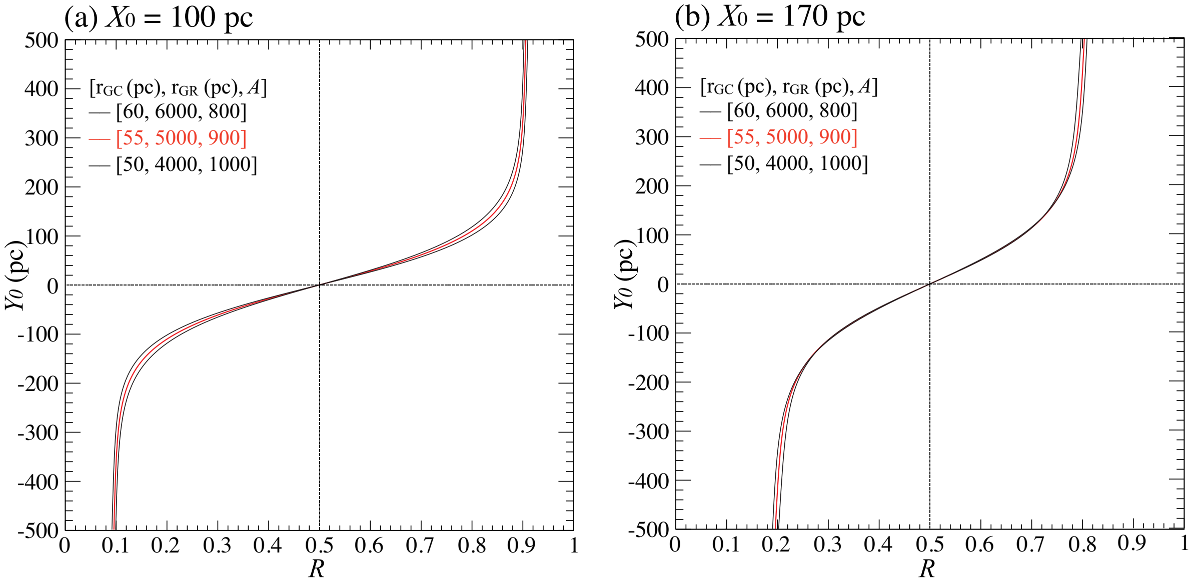

Fig. 7.3.—: Line-of-sight position (Y_0) as a function of the parameter R (see equation (7.1)). The cases for (a) Sgr B at X_0=100 pc and (b) for Sgr E at X_0=170 pc are shown. The red solid lines represent the Y-R curves adopted for calculations of the line-of-sight positions. Other Y-R curves (black lines), calculated from different parameters ($r_{\rm GC}$, $r_{\rm GR}$, A) in $I(X, Y)$, are also plotted to show model uncertainties estimated from the results of Uchiyama et al. (2012)(c.f., figure 7.2 and figure 2.17).

Table 7.1—: Three-dimensional positions[*] of XRNe.

XRN ID	l [deg.]	b [deg.]	X [ly]	Z [ly]	Y[†] [ly]
Clump D	1.17	−0.04	560	3	55^{+580}_{-310}
M0.74−0.09	0.74	−0.09	363	−25	-202$^{+50}_{-60}$
M0.74-sub	0.74	−0.15	363	−47	-280$^{+80}_{-60}$
Sgr B2	0.66	−0.05	327	−2	-55$^{+50}_{-60}$
Sgr B1	0.51	−0.11	258	−30	-75$^{+50}_{-50}$
Sgr C3	−0.41	−0.14	-162	−43	-173^{+30}_{-30}
Sgr C2	−0.53	−0.15	-216	−47	189^{+200}_{-30}
Sgr C1	−0.56	−0.06	-230	−7	-241^{+40}_{-60}
Clump E	−1.24	−0.02	-540	13	-408$^{+60}_{-570}$

[*] Values of l and b are the Galactic coordinates at the center of spectral regions used for each XRN. Values of X, Z, and Y respectively correspond to the positions along l, b, and line of sight, with origins at Sgr A*.

[†] The Y errors are calculated from statistical ranges of R at 90% confidence level.

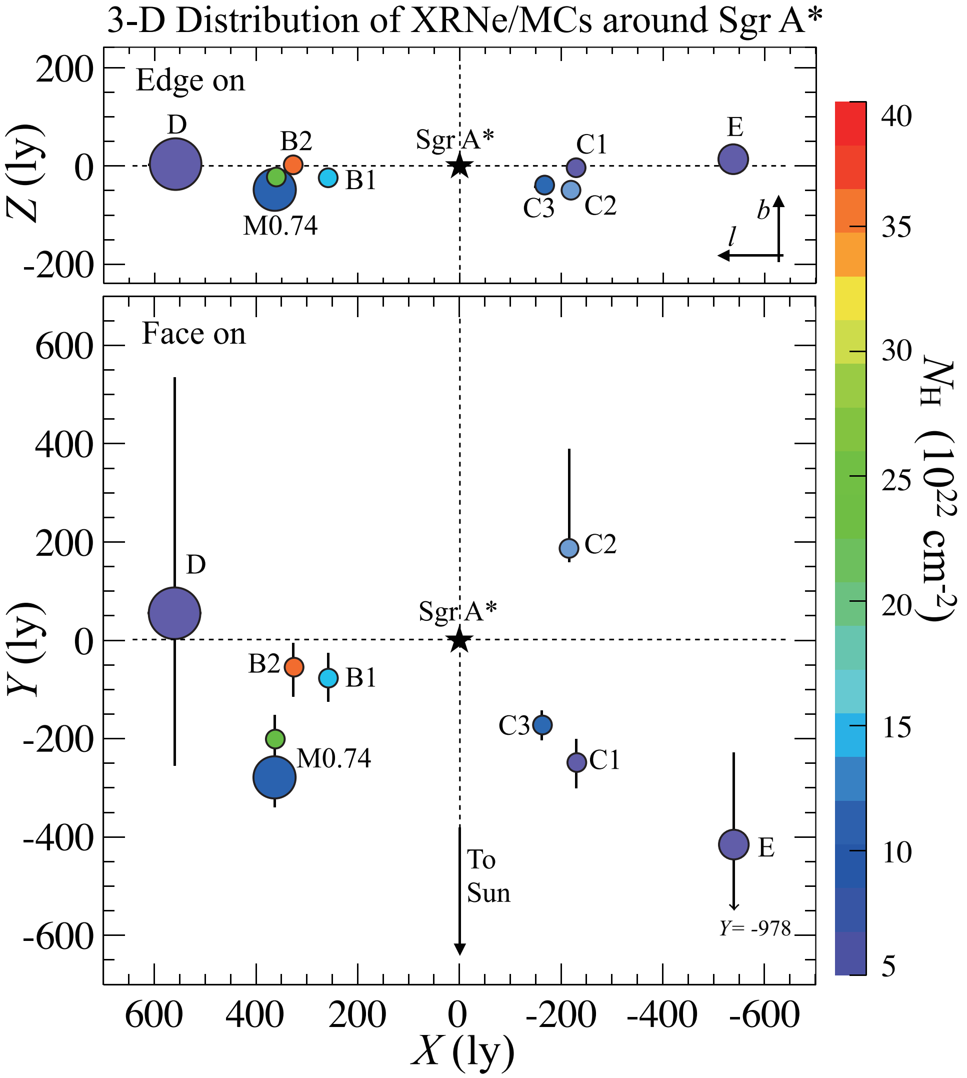

Fig. 7.4.—: (a) Three dimensional (face-on and edge-on) distribution of the XRNe/MCs around Sgr A*. Colors and sizes of the circles represent column densities ($N_{\rm H}$) and spatial sizes (from spectral regions) of the XRNe, respectively. Coordinates X, Z, and Y correspond to positions in the Galactic longitude (l), latitude (b), and the line of sight from Sgr A*, respectively. Position parameters for each XRN are given in table 7.1.

7.2.2 Association with the CMZ

We have obtained a face-on view of XRNe around the GC, directly and solely from the X-ray data and analyses. The *l*-*b* positions and large column densities ($N_{\rm H} \sim 5 - 40 \times 10^{22}$ H cm^{-2}) of the XRNe are consistent with those of the giant MCs (e.g., Sgr B2 and B1) in the CMZ (Morris & Serabyn 1996). Thus, these XRNe should be major components of the CMZ and therefore represent its basic structure. As shown in figure 7.4b, the Sgr B XRNe/MCs are mostly located in foreground to Sgr A*. Although proximately (∼40 ly) located in the projection, Sgr C1 and C3 is in front of the X-axis (Sgr A*), while Sgr C2 (the most massive one) is largely behind C1 by ∼400 ly beyond the X-axis. Clump E and Clump D lie before and slightly behind Sgr A*, respectively.

In a general perspective of the CMZ in radio studies, the theory of the central bar potential hypothesized closed elliptical orbits called the X1 and X2 families, which are originated from the Lindblad resonance between the gas and the bar (e.g., Contopoulos & Mertzanides 1977; Binney et al. 1991; Morris & Serabyn 1996). The X1 orbits are elongated along the bar, while the X2 orbits are rounder and perpendicular to the bar. In the *l*-*V* map, the X1 and X2 orbits should be projected as parallelogram structures, which is consistent with the radio observational results (see figure 2.6). Thus, following the X-orbits models, the radio observations on velocities of MCs can predict the line-of-sight positions and their large structures such as Arm I/II (Sofue, 1995) and the Galactic center bow (GCB; Tsuboi et al. 1999). These are, however, depending on the models and hence not conclusive.

The X-ray face-on view of MCs in the CMZ (figure 7.4b) is obtained without information of velocities, which can therefore verify the X-orbits model in the bar potential. In figure 7.5, we superpose the CMZ structures (Arm I/II) predicted by radio *l*-*V* observations and possible X1/2 orbits onto our X-ray face-on view. We find good coincidences between them. The details of their relations are discussed in the following paragraphs.

Arm I, Arm II, and GCB

The X-Y distribution of XRNe suggests that Sgr B2, B1, M 0.74, Sgr C1, and Clump D may belong to Arm I, while Sgr C2 and Clump E is in Arm II, because Sofue (1995) predicted that Arm I and Arm II are respectively located in the foreground and background with respect to Sgr A* by assuming a uniform circular rotation (c.f., figure 2.7a). These two arms were identified in the CO observation of *l*-*V* diagrams (Sofue 1995; see figure 7.6): Arm I is stretching from (−1.°0, −200 km s^{-1}) through (−0.°7, −150 km s^{-1}) to (0.°9, +80 km s^{-1}) and Arm II is stretching from (−0.°6, −80 km s^{-1}) through (−0.°1, +60 km s^{-1}) to (1.°0, +100 km s^{-1}). Although Sofue (1995) only defined Arm structures within $|l| \leq 1°$ (i.e., $|X| \leq 400$ ly), Arm I and Arm II respectively extend to east and west more than 1.°0,

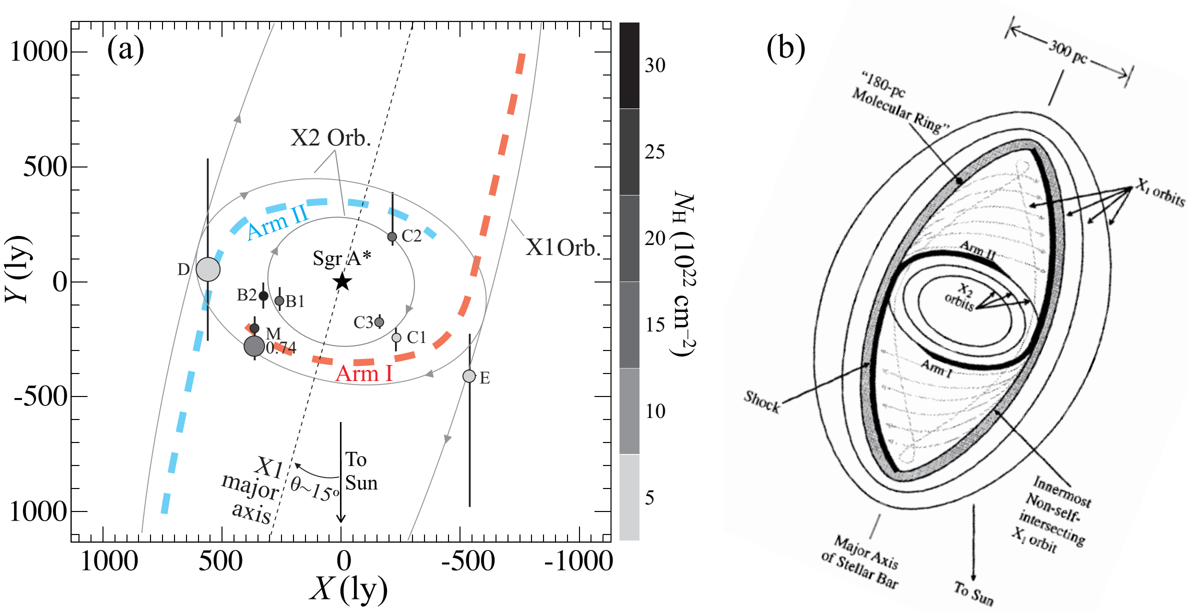

Fig. 7.5.—: (a) Face-on distribution of the XRNe around Sgr A* superposed with Arm I/II (dashed lines) and possible orbits of X1 and X2 (grey lines). The orbit parameters (major-axis length, eccentricity, inclination angle) used for inner X2, outer X2, and X1 are (310 ly, 0.2, 105°), (620 ly, 0.5, 105°), and (2400 ly, 0.9, 15°), respectively. (b) Schematic view of X1/2 orbits and Arm I/II structures (Morris & Serabyn 1996; Binney et al. 1991; Sofue 1995).

according to Morris & Serabyn (1996) (see figure 7.5b).

The face-on XRN alignments of M0.74, Sgr B1-2, Sgr C1, and Clump E (figure 7.4) also agree with the GCB (figure 2.7c). The GCB is found from the *l*-*b*-*V* observation of the CS line by Tsuboi et al. (1999), which shows continuous stream-like appearances start from ($-0.^\circ80$, $-0.^\circ08$, -150 km s^{-1}), bends at ($-0.^\circ7$, $-0.^\circ08$, $+50$ km s^{-1}), and end at ($1.^\circ50$, $-0.^\circ15$, $+50$–100 km s^{-1}). The GCB corresponds to a more general picture of Arm I. The absorption features (shadows at $l < 0$) are observed in the near-IR and H I maps, which indicates that the eastern part of the GCB is closer to Sgr A* than the western part (Tsuboi et al. 1999 and references therein; see figure 2.7c).

In figure 7.6, we show the *l*-*V* distributions of Arm I, Arm II, GCB, and the corresponding XRNe. The line-of-sight velocity for each XRN (c.f., table 7.2) had been estimated by comparing their positions and morphologies on the *l*-*b* plane between X-ray and Radio data (c.f., chapter 4–6).

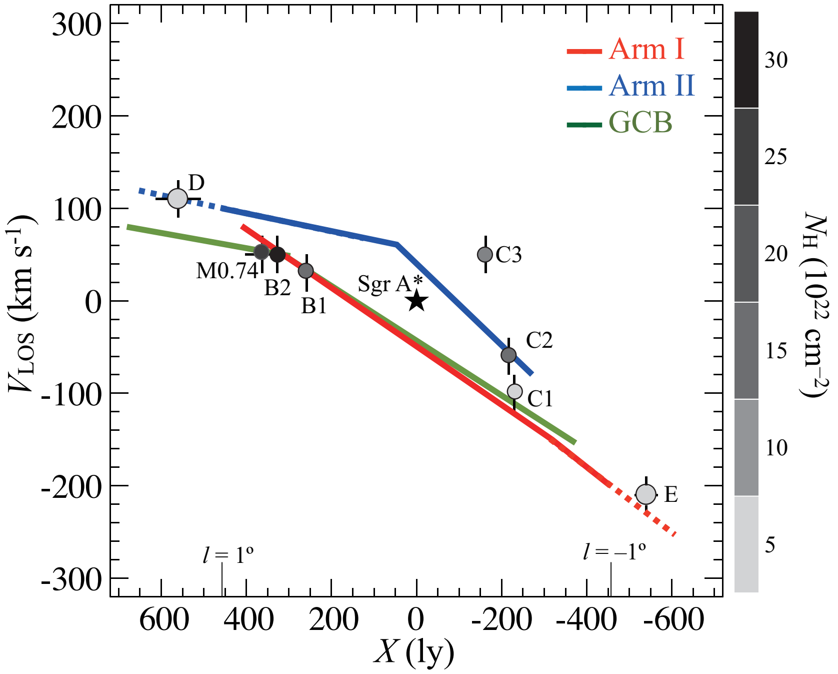

Fig. 7.6.—: Distribution of the line-of-sight velocity of XRNe near the GC (c.f., table 7.1). The vertical errors correspond to the typical velocity width of 40 km s^{-1}. The known l-V structures of Arm I, Arm II, and GCB are shown with red, blue, and green solid lines, respectively; the dashed lines extending from Arm I and Arm II are interpretations in this thesis (see details in the text).

X1 and X2 Orbits

As shown in figure 7.5, we can draw two X2 and one X1 orbits in order to match the face-on distribution of XRNe. The Sgr B1–2 and C1–3 are clearly located on a inner X2 orbit, while Clump D, M0.74, and Clump E are on a outer X2 orbit. Clump D and E are also near the intersections between the outer X2 and X1 orbits. The inclination angle of the X1 major axis with respect to our line of sight is about $\theta \sim 15^\circ - 30^\circ$, which is consistent with model predictions ($\theta \sim$15° to 45°; e.g., Morris & Serabyn 1996).

In summary, as an original result, the face-on view of XRNe basically proves the radio predictions for the CMZ structures such as Arm I and Arm II. The alignments of Sgr B and Sgr C XRNe suggest the existence of X2 orbits and hence support the bar-potential theory. This enhances the reliability of our new X-ray method which directly determines the line-of-sight position. Details of the X-ray and radio associations are listed in table 7.2.

Table 7.2—: Association of XRNe with radio structures in the CMZ.

XRN	$l^{\dagger}$	$V_{\mathrm{LOS}}^{\ddagger}$	Arm I (GCB)*	Arm II*	X1*	X2-in*	X2-out*
Clump D	1.17	+110		y	y		y
M0.74−0.09	0.74	+50	y				y
M0.74-sub	0.74	+50	y				y
Sgr B2	0.66	+50	y			y	
Sgr B1	0.51	+30	y			y	
Sgr C3	−0.41	+50				y	
Sgr C2	−0.53	−60		y		y	
Sgr C1	−0.56	−100	y			y	
Clump E	−1.24	−210	y		y		y

† The Galactic longitude coordinates (in units of degree) at the center of spectral regions used for each XRN/MC.
‡ Line-of-sight velocity (in units of km s^{-1}) measured from radio observations of doppler shift. Typical velocity width is 40 km s^{-1}.
* Possible associations with the radio structures and orbits described in text and figure 7.5. The mark "y" represents yes.

7.3 Active History of Sagittarius A*

7.3.1 Derivation of X-ray Light Curve

On the basis of the XRN model (c.f., figure 2.22) of the past flares from Sgr A*, we draw the parabolas in figure 7.7, with their common foci at Sgr A*, to illustrate the equi-delay-time contours for X-ray echoes. The time delay (T_*) of an echo, light-passage (Sgr A*-XRN-Sun) divided by light speed (c), is given as below.

$$T_* \; = \; (\sqrt{X^2+Y^2}+Y)/c \qquad \text{[yr]} \tag{7.2}$$

As shown in figure 7.7, we find that the XRNe are not located on a single parabola (i.e., same T_*), which directly indicates multiple flares from Sgr A* at different epochs in the past. This result is also supported by observations of different a-few-years time variabilities, of either flux decrease or increase, from 6.4 keV clumps in the Sgr B, Sgr C, and Sgr A regions (figure 5.6; figure 2.21; also see discussions in section 5.3.3). Then, we can quantitatively investigate the activity history for Sgr A*.

Using results (table 4.4; table 5.2; table 6.2; table 7.1) of the Fe I intensity by reflection ($I_{6.4\ \mathrm{keV}}$), the column density of XRN (Abs1), and the distance (D_*=$\sqrt{X^2+Y^2}$), the required

X-ray (2–10 keV) luminosity of Sgr A* ($L_{\mathrm{X}*}$) can be expressed in the following equation (from Nobukawa et al. 2008; Sunyaev & Churazov 1998; also c.f., equation (2.20) and figure 2.22).

$$L_{\mathrm{X}*} \approx 1.0 \times \frac{(I_{6.4\ \mathrm{keV}}\ /10^{-6}\ \mathrm{photons\ cm^{-2}s^{-1}arcmin^{-2}}) \times (\mathrm{D}_*\ /300\ \mathrm{ly})^2}{(N_{\mathrm{H}}\ /10^{22}\ \mathrm{H\ cm^{-2}})} \quad [10^{40}\ \mathrm{erg\ s^{-1}}] \tag{7.3}$$

Here, isotropic radiation with a photon index of $\Gamma = 1.6$ from Sgr A*, sphere structure (with sizes of the analyzed spectral regions) and the solar iron abundance for XRNe are the underlying assumptions. Also note that equation (7.3) gives the average luminosity of a flare over the light-crossing time of each XRN (c.f., section 2.4.3).

Using equation (7.2) and (7.3), we compute T_* and $L_{\mathrm{X}*}$ for nine XRNe in the Sgr C, Sgr B, Sgr D, and Sgr E regions. The resultant long-term light curve of Sgr A* is plotted in figure 7.8 and its details are summarized in table 7.3. Sgr A* was active with many short flares between $L_{\mathrm{X}*} = 1\text{–}3 \times 10^{39}$ erg s^{-1} during the past ~50 to ~600 years (i.e., past flare state). Thanks to the measurement of line-of-sight position of Sgr C2 and Clump D (see figure 7.7), we find that Sgr A* was experiencing periods of high luminosity already 600 years ago, which extends the light curve of Inui et al. (2009) and Ponti et al. (2010) back by 200–500 years.

7.3.2 Behaviours of the Past Flare State

During the past flare state, Sgr A* exhibited sporadic fluctuations (short flares) at 200–300 ago and ~100 years ago, as represented in figure 7.8. The short flare at 200–300 years ago would be responsible for the short-term time variability (2005–2009) of Sgr B2 and M 0.74−0.09 (figure 2.21; Nobukawa et al. 2011; Koyama et al. 2008; Terrier et al. 2010), and hence the time scale would be ~5 years. The other short flare at ~100 years ago has similar time scale as inferred by the 6.4 keV time variability (increase) of Sgr C1 in 5 years (2006–2010) at 3-σ level (table 5.2). This flare may correspond to the time variability of the Sgr A XRNe. Muno et al. (2007) and Koyama et al. (2009) reported variability of the 6.4 keV line from the Sgr A cloud in a short time-scale of 3–5 years at a $\sim 5\sigma$ sigma level. Then Ponti et al. (2010) and Capelli et al. (2012) predicted the flare events occurred between ~100 and ~400 years ago, which is basically consistent with our results.

The detailed behavior of the activity at ~100 years ago is not completely clear. From the illumination pattern in the Sgr A complex, Ponti et al. (2010) proposed that the flare should have started ~400 years ago, while Capelli et al. (2012) suggested that an active period ended ~150 years ago. However, the estimated flare luminosities were different: $L_{\mathrm{X}*} \sim 10^{39}$ erg s^{-1}

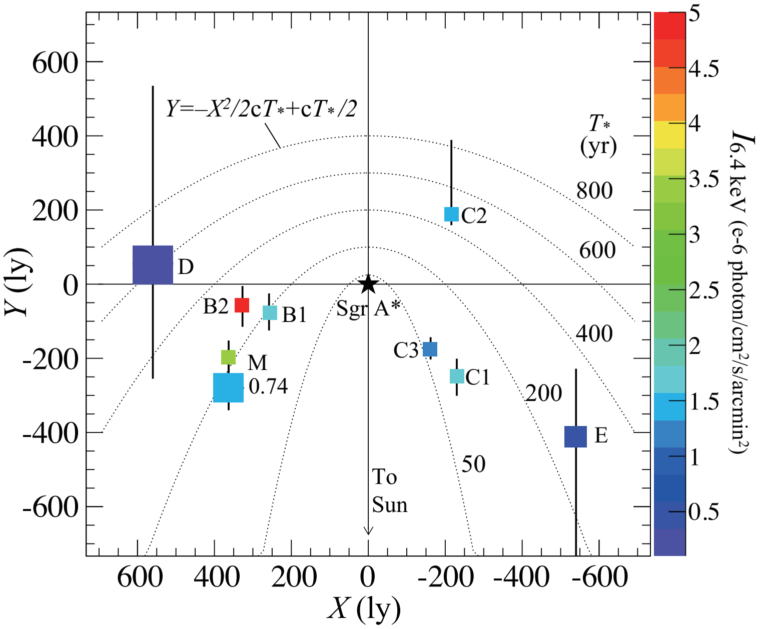

Fig. 7.7.—: Face-on distribution of XRNe superposed with parabolas (dashed lines) of equal-time delay (T_*; see definition in text) contours; different parabolas represent echoes due to Sgr A* flares in different past epochs. Coordinates X and Y correspond to positions in the Galactic longitude (l) and in the line of sight from Sgr A*, respectively.

was suggested by Ponti et al. (2010), while $L_{\mathrm{X}*} \sim 10^{38}$ erg s^{-1} was suggested by Capelli et al. (2012). These inconsistencies are mainly attributable to unclear line-of-sight positions and partly due to the difficult estimation of N_{H} for the Sgr A XRNe. The luminosity determined by Capelli et al. (2012) is $\sim 10^{37}$–10^{38} erg s^{-1} around 70 and 130 years ago, which is about 10 times lower than that obtained here: $L_{\mathrm{X}*} \sim 10^{39}$ erg s^{-1} at ~90 years ago. The high luminosity indicated by C1 may be attributed to a short-term flare that occurred in the fading period reported by Capelli et al. (2012). A unified analysis for the Sgr A XRNe by the same method performed in Sgr B, C, D, and E in this thesis would be able to solve these problems.

Apart from the 6.4 keV clumps with compact angular distribution such as Sgr B2, Sgr C1, and Sgr E, we also detected relatively weak 6.4 keV line ($I_{6.4\mathrm{keV}} \sim 5\times10^{-7}$ photons cm^{-2}s^{-1}arcmin^{-2}) all over the GC region (e.g., Sgr C ref 1–2, figure 4.1, table 4.4; Sgr B region 1, figure 5.1, table 5.2). The spectra of these regions exhibit large $EW_{6.4\ \mathrm{keV}}$ above 1 keV and high GC absorption of N_{H}=7–12$\times10^{22}$ H cm^{-2}, which are consistent with the XRN model. Thus, the spatially-featureless 6.4 keV emissions are probably originated from the X-ray reflections by diffuse molecular gas filling the CMZ rather than compact MCs (e.g., Sgr B2). In this case, the observed 6.4 keV intensity is the line-of-sight integration of

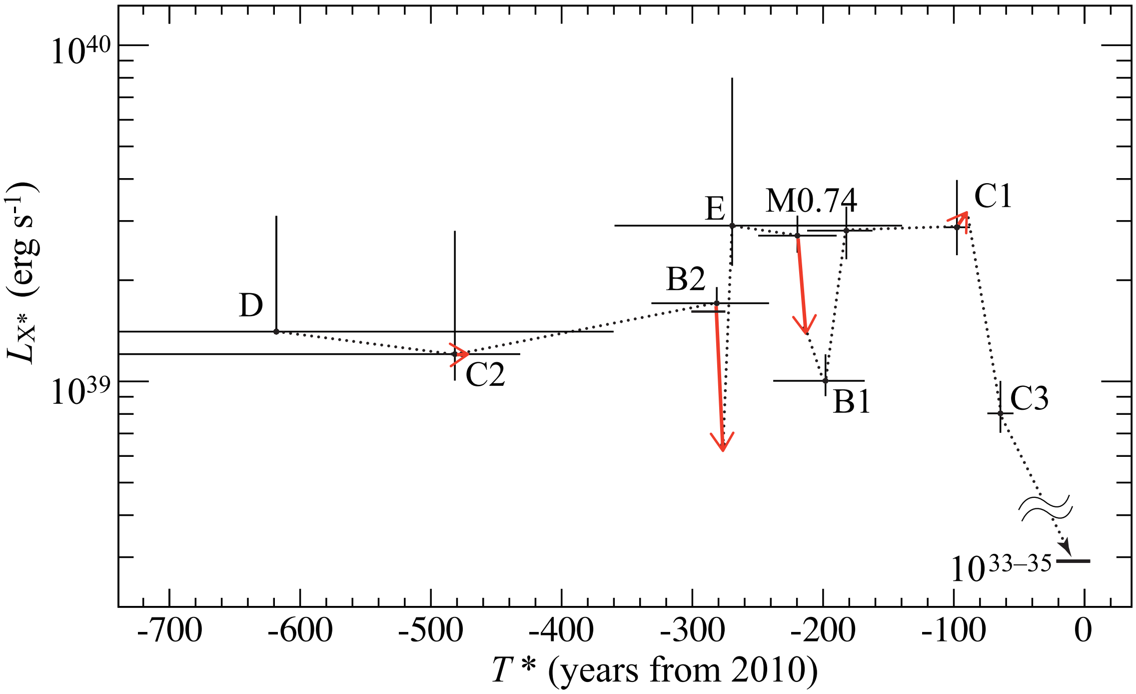

Fig. 7.8.—: X-ray light curve of Sgr A* for the past 600 years (see table 7.3 for parameter details). Red arrows show the results from observations of short-term 6.4 keV variabilities between 5 years. The present luminosity of Sgr A* is quoted from Baganoff et al. (2001) and Porquet et al. (2003).

reflections by continuous (or multiple) X-ray flares over the past 500 years (see details in Chernyshov et al. 2012). The average luminosity of Sgr A* over past several centuries (L_{X*}^{ave}) can be estimated from equation (7.3) using the best-fit parameters ($I_{6.4keV}$ and N_H) of Sgr C ref 1–2 and Sgr B region 1. Although the gas is most likely distributed continuously along the line of sight, the lower limit of L_{X*}^{ave} is still determined by the minimum distance, which is the project distance at a given X position ($D_*{=}|X|$). The L_{X*}^{ave} estimated from Sgr C ref 1, ref 2, and Sgr B region 1 are respectively, >0.47, >0.55, and >0.84 in unit of 10^{39} erg s^{-1}. These results are consistent with the picture that Sgr A* had been in a flare state with high luminosity ($L_{X*} \sim 10^{39}$ erg s^{-1}) over centuries in the past.

Table 7.3—: Parameters† of XRNe and past luminosity of Sgr A*.

XRN ID	Obs. Year	$D_*^{\S}$ [ly]	$T_*^{\parallel}$ [year]	$L_{\mathrm{X}*}^{\#}$ [10^{39} erg s^{-1}]
Clump D	2007	562^{+290}_{-2}	618^{+860}_{-260}	$1.4^{+0.3}_{-0.0}$
Sgr C2‡	2006 (2010)	287^{+150}_{-20}	476^{+350}_{-50}	$1.2^{+1.6}_{-0.2}$ (1.2)
Sgr B2‡	2005 (2009)	331^{+20}_{-5}	281^{+50}_{-40}	$1.7^{+0.2}_{-0.1}$ (0.65)
Clump E	2008	677^{+440}_{-90}	269^{+90}_{-130}	$2.9^{+5.1}_{-0.7}$
M0.74−0.09‡	2005 (2009)	416^{+30}_{-20}	219^{+30}_{-30}	$2.7^{+0.4}_{-0.3}$ (1.4)
Sgr B1	2006	269^{+20}_{-10}	198^{+40}_{-30}	$1.0^{+0.2}_{-0.1}$
M0.74-sub	2007	459^{+40}_{-40}	182^{+40}_{-20}	$2.8^{+0.5}_{-0.5}$
Sgr C1‡	2006 (2010)	333^{+50}_{-30}	92^{+10}_{-10}	$2.9^{+1.1}_{-0.5}$ (3.1)
Sgr C3	2010	237^{+20}_{-20}	64^{+10}_{-10}	$0.8^{+0.2}_{-0.1}$

† Errors of D_*, T_*, and $L_{\mathrm{X}*}$ are estimated using the error ranges of line-of-sight positions Y (see table 7.1).

§ Distance from Sgr A* calculated from $D_*=\sqrt{X^2+Y^2}$.

‖ Time delay of echo from Sgr A* calculated from equation (7.2) and counted from 2010.

\# Required past X-ray luminosity of Sgr A* calculated from equation (7.3), also see text.

‡ Values in brackets are the results from observations of short-term 6.4 keV variabilities between 5 years (C1 and C2, section 5.2.3, this work; B2 and M,0.74, Nobukawa et al. (2011)). Errors due to position uncertainties of Y are not included.

7.3.3 Interpretation as Low-Luminosity AGN

The average X-ray luminosity of Sgr A* in the past flare state was $L_{\mathrm{X}*}^{\mathrm{ave}} \simeq 2\times10^{39}$ erg s^{-1} (table 7.3), which corresponds to $\sim 4\times10^{-6}$ of the Eddington limit ($L_{\mathrm{E}} \simeq 5\times10^{44}$ erg s^{-1} at 4×10^6 M$_\odot$). As shown in figure 7.9a, comparing the luminosities, we may state that Sgr A* had been acting as a low-luminosity AGN, such as M 81* (Ishisaki et al. 1996; Devereux et al. 2003) and M 51* (Terashima & Wilson, 2001), during the past ~500 years.

The present X-ray luminosity of Sgr A* is $L_{\mathrm{X}*} \sim 10^{33-35}$ erg s^{-1} (Baganoff et al. 2001; Porquet et al. 2003), and hence a sudden luminosity drop, by 4–6 orders of magnitude from the flare state, should have occurred within ~100 years. Schawinski et al. (2010) reported that the quasar IC 2497 with mass of $\sim 10^9$ M$_\odot$ experienced an dramatic luminosity drop by more than 4 orders of magnitude in less than 70000 years. On the other hand, for Galactic X-ray binaries with a black hole mass of ~10 M$_\odot$ (e.g., GRS 1915+105; Greiner et al. 1996), a state change from high/soft to low/hard was detected on time scales of ~1 hour.

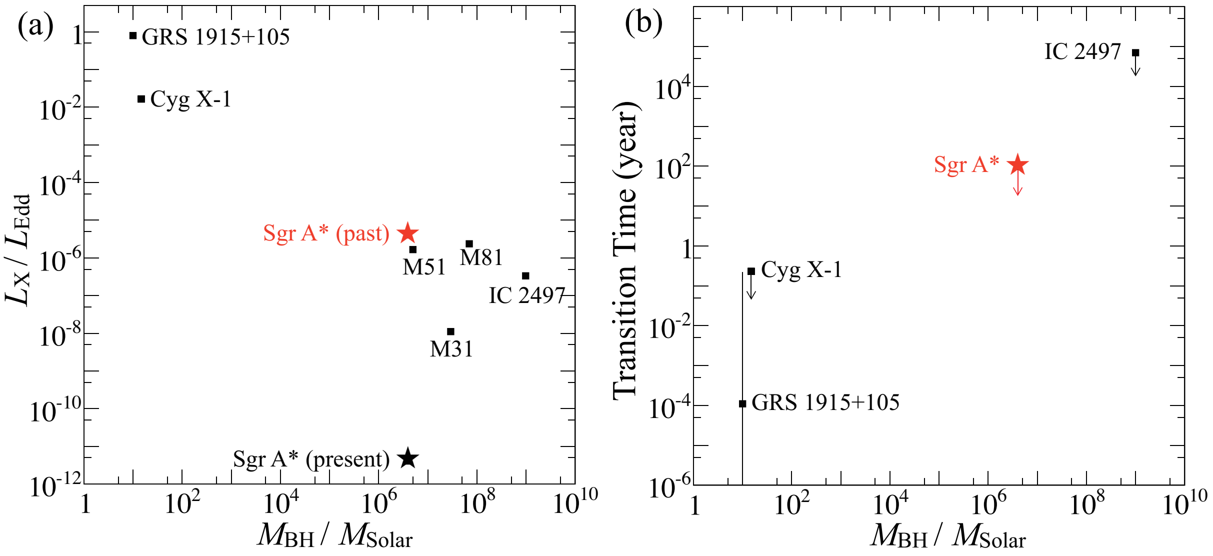

Fig. 7.9.—: Comparison of observational results between Sgr A*, Galactic black holes, and LLAGNs. (a) Plot of present X-ray luminosities (normalized with corresponding Eddington limits) against black-hole masses. The past luminosity of Sgr A* by this work is added. (b) Plot of state-transition time against black-hole masses. The diagrams include data points of Sgr A* (Baganoff et al. 2003), M 81* (Ishisaki et al. 1996; Devereux et al. 2003), M 31* (Garcia et al. 2000), M 51* (Terashima & Wilson 2001; Kohno et al. 1996), IC 2497* (Schawinski et al., 2010), Cyg X-1 (Zhang et al. 1997), and GRS 1915+105 (Greiner et al. 1996).

Assuming that the state-transition time scale is proportional to black-hole mass, at a mass of 4×10^6 $M_\odot$, 70000 years (for 10^9 $M_\odot$) and 1 hour (for 10 $M_\odot$) are scaled down to 280 years and up to 46 years, respectively. Then, the time scale of the luminosity drop for Sgr A* is estimated to be as fast as about 50–300 year, which is consistent with the prediction ($\lesssim 100$ year) in our light curve (figure 7.8).

Chapter 8

Conclusions

In this thesis, using the high-quality and high-statistic data by Suzaku, we carried out an unified study on various diffuse X-ray emissions from the major MC (Sgr B, C, D, and E) regions around the GC. The analyses were performed by careful spectral modeling in consideration of the three-dimensional alignments. Followings are the highlights.

- The diffuse 6.4 keV emissions over $|l| \sim 0.^\circ 5$–$1.^\circ 3$, including clumpy regions associated with giant MCs and spatially-featureless dim regions, are consistent with the spectral model of XRN.

- The diffuse thermal emission in 2–10 keV over $|l| \sim 0.^\circ 5$–$1.^\circ 3$ can be explained by the spectral model of a two-temperature ($k_{\mathrm{B}}T_{\mathrm{LP}} \approx 0.9$ keV and $k_{\mathrm{B}}T_{\mathrm{HP}} \approx 6.5$ keV) CIE plasma with the solar abundance; the mixing ratio between emission measures (EM) of the two plasmas is $EM_{\mathrm{HP}}/EM_{\mathrm{LP}} \approx 0.27$.

- The XRNe of Sgr B, C, D, and E, with different radial velocities, are largely separated in the line-of-sight position with respect to Sgr A*. The Sgr B is mostly located in foreground. The most massive one of Sgr C is beyond, while another two are in front. Sgr E and Sgr D are located before and slightly behind, respectively. The face-on distribution of XRNe basically proves the presence of dynamical structures in bar potential hypothesized by radio observations.

- The past X-ray activity from Sgr A* was not a single event, but consisted of multiple events. The SMBH had been in a flare state with sporadic fluctuations between L_{X}=1–3 $\times 10^{39}$ erg s^{-1}; the short (~5 years) flares occurred continuously during the past 50 to 600 years.

References

Aharonian, F., Akhperjanian, A. G., Bazer-Bachi, A. R., et al. 2006, Nature, 439, 695

Anders, E., & Grevesse, N. 1989, Geochim. Cosmochim. Acta, 53, 197

Baganoff, F. K., Bautz, M. W., Brandt, W. N., et al. 2001, Nature, 413, 45

Baganoff, F. K., Maeda, Y., Morris, M., et al. 2003, ApJ, 591, 891

Binney, J., Gerhard, O. E., Stark, A. A., Bally, J., & Uchida, K. I. 1991, MNRAS, 252, 210

Bleach, R. D., Boldt, E. A., Holt, S. S., Schwartz, D. A., & Serlemitsos, P. J. 1972, ApJ, 174, L101

Burke, B. E., Mountain, R. W., Harrison, D. C., Bautz, M. W., Doty, J. P., Ricker, G. R., & Daniels, P. J. 1991, Proc. IEEE, 38, 1069

Capelli, R., Warwick, R. S., Porquet, D., Gillessen, S., & Predehl, P. 2012, arXiv:1207.1436

Chernyshov, D., Dogiel, V., Nobukawa, M., et al. 2012, PASJ, 64, 14

Clemens, D. P. 1985, ApJ, 295, 422

Contopoulos, G., & Mertzanides, C. 1977, A&A, 61, 477

Dame, T. M., Hartmann, D., & Thaddeus, P. 2001, ApJ, 547, 792

Dahmen, S., et al. 1998, A&A, 331, 959

Dehnen, W., & Binney, J. 1998, MNRAS, 294, 429

Devereux, N., Ford, m8H., Tsvetanov, Z., & Jacoby, G. 2003, AJ, 125, 1226

Diehl, R., Halloin, H., Kretschmer, K., et al. 2006, Nature, 439, 45

Dobashi, K., Uehara, H., Kandori, R., et al. 2005, PASJ, 57, 1

Dogiel, V., Chernyshov, D., Koyama, K., Nobukawa, M., & Cheng, K.-S. 2011, PASJ, 63, 535

Ebisawa, K., Yamauchi, S., Tanaka, Y., et al. 2008, PASJ, 60, 223

Ezuka, H., & Ishida, M. 1999, ApJS, 120, 277

Fukuoka, R., Koyama, K., Ryu, S. G., & Tsuru, T. G. 2009, PASJ, 61, 593

Garcia, M. R., Murray, S. S., Primini, F. A., et al. 2000, ApJ, 537, L23

G. P. Garmire, M. W. Bautz, P. G. Ford, J.A. Nousek, and G. R. Ricker, Jr., in $Proc.SPIE$, vol. 4851, pp. 2844, 2003

Ghez, A. M., Salim, S., Hornstein, S. D., et al. 2005, ApJ, 620, 744

Ghez, A. M., Salim, S., Weinberg, N. N., et al. 2008, ApJ, 689, 1044

Güver, T., Özel, F. 2009, MNRAS, 400, 2050

Greiner, J., Morgan, E. H., & Remillard, R. A. 1996, ApJ, 473, L107

Inui, T., Koyama, K., Matsumoto, H., & Tsuru, T. G. 2009, PASJ, 61, 241

Ishida, M., Okada, S., Hayashi, T., et al. 2009, PASJ, 61, 77

Ishisaki, Y., Makishima, K., Iyomoto, N., et al. 1996, PASJ, 48, 237

Ishisaki, Y., Maeda, Y., Fujimoto, R., et al. 2007, PASJ, 59, 113

Iwan, D., Shafer, R. A., Marshall, F. E., et al. 1982, ApJ, 260, 111

Kaastra, J. S., & Mewe, R. 1993, A&AS, 97, 443

Kawai, N., Fenimore, E. E., Middleditch, J., et al. 1988, ApJ, 330, 130

Kelley, L. R., et al. 2007, PASJ, 59, S77

Kohno, K., Kawabe, R., Tosaki, T., & Okumura, S. K. 1996, ApJ, 461, L29

Kokubun, M., et al. 2007, PASJ, 59, S53

Koyama, K., Makishima, K., Tanaka, Y., & Tsunemi, H. 1986, PASJ, 38, 121

Koyama, K., Awaki, H., Kunieda, H., Takano, S., & Tawara, Y. 1989, Nature, 339, 603

Koyama, K. 1989, PASJ, 41, 665

Koyama, K., Maeda, Y., Sonobe, T., Takeshima, T., Tanaka, Y., & Yamauchi, S. 1996, PASJ, 48, 249

Koyama, K., et al. 2007a, PASJ, 59, S23

Koyama, K., et al. 2007b, PASJ, 59, S221

Koyama, K., et al. 2007c, PASJ, 59, S245

Koyama, K., Inui, T., Matsumoto, H., & Tsuru, T. G. 2008, PASJ, 60, S201

Koyama, K., Takikawa, Y., Hyodo, Y., Inui, T., Nobukawa, M., Matsumoto, H., & Tsuru, T. G. 2009, PASJ, 61, 255

Kushino, A., Ishisaki, Y., Morita, U., Yamasaki, N. Y., Ishida, M., Ohashi, T., & Ueda, Y. 2002, PASJ, 54, 327

Laustsen S., Madsen C., West R. M., 1987, Exploring the Southern Sky: A Pictorial Atlas from the European Southern Observatory. Springer-Verlag, Berlin

Launhardt, R., Zylka, R., & Mezger, P. G. 2002, A&A, 384, 112

LaRosa, T. N., Kassim, N. E., Lazio, T. J. W., & Hyman, S. D. 2000, AJ, 119, 207

Law, C. J., Yusef-Zadeh, F., Cotton, W. D., & Maddalena, R. J. 2008, ApJS, 177, 255

Lechner, P. et al., 2010, Proc. SPIE, 7742, 77420T-8

Masui, K., Mitsuda, K., Yamasaki, N. Y., Takei, Y., Kimura, S., Yoshino, T., & McCammon, D. 2009, PASJ, 61, 115

Mitsuda, K., et al. 2007, PASJ, 59, S1

Murakami, H., Koyama, K., Sakano, M., Tsujimoto, M., & Maeda, Y. 2000, ApJ, 534, 283

Murakami, H., Koyama, K., Tsujimoto, M., Maeda, Y., & Sakano, M. 2001, ApJ, 550, 297

Morris, M., & Serabyn, E. 1996, ARA&A, 34, 645

Magorrian, J., Tremaine, S., Richstone, D., et al. 1998, AJ, 115, 2285

Mori, H., Tsuru, T. G., Hyodo, Y., Koyama, K., & Senda, A. 2008, PASJ, 60, 183

Muno, M. P., Arabadjis, J. S., Baganoff, F. K., et al. 2004, ApJ, 613, 1179

Muno, M. P., Bauer, F. E., Bandyopadhyay, R. M., & Wang, Q. D. 2006, ApJS, 165, 173

Muno, M. P., Baganoff, F. K., Brandt, W. N., Park, S., & Morris, M. R. 2007, ApJ, 656, L69

Nakanishi, H., & Sofue, Y. 2006, PASJ, 55, 191

Nakanishi, H., & Sofue, Y. 2006, PASJ, 58, 847

Nobukawa, M., et al. 2008, PASJ, 60, S191

Nobukawa, M., Koyama, K., Matsumoto, H., & Tsuru, T. G. 2009, PASJ, 61, 93

Nobukawa, M., Koyama, K., Tsuru, T. G., Ryu, S. G., & Tatischeff, V. 2010, PASJ, 62, 423

Nobukawa, M., Ryu, S. G., Tsuru, T. G., & Koyama, K. 2011, ApJ, 739, L52

Nakajima, H., Yamaguchi, H., Matsumoto, H., et al. 2008, PASJ, 60, 1

Nakajima, H., Tsuru, T. G., Nobukawa, M., et al. 2009, PASJ, 61, 233

Narayan, R. 2005, Ap&SS, 300, 177

Oka, T., Hasegawa, T., Sato, F., Tsuboi, M., & Miyazaki, A. 1998, ApJS, 118, 455

Okuda, H., Maihara, T., Oda, N., & Sugiyama, T. 1977, Nature, 265, 515

Oort, J. H., Kerr, F. J., & Westerhout, G. 1958, MNRAS, 118, 379

Otranto, S., Olson, R. E., & Beiersdorfer, P. 2006, Phys. Rev. A, 73, 022723

Ozawa, M., Uchiyama, H., Matsumoto, H., et al. 2009, PASJ, 61, 1

Park, S., Muno, M. P., Baganoff, F. K., et al. 2004, ApJ, 603, 548

Ponti, G., Terrier, R., Goldwurm, A., Belanger, G., & Trap, G. 2010, ApJ, 714, 732

Porquet, D., Predehl, P., Aschenbach, B., et al. 2003, A&A, 407, L17

Predehl, P., & Truemper, J. 1994, A&A, 290, L29

Prigozhin, G. et al., 2009, IEEE Trans. Nucl. Sci., 56, 11, 2602

Ryu, S. G., Koyama, K., Nobukawa, M., Fukuoka, R., & Tsuru, T. G. 2009, PASJ, 61, 751

Ryu, S. G. et al., 2011, IEEE Trans. Nucl. Sci., 58, 5, 2528

Sakano, M., Koyama, K., Murakami, H., Maeda, Y., & Yamauchi, S. 2002, ApJS, 138, 19

Shakura, N. I., & Sunyaev, R. A. 1973, A&A, 24, 337

Sawada, T., Hasegawa, T., Handa, T., & Cohen, R. J. 2004, MNRAS, 349, 1167

Sawada, M., Tsujimoto, M., Koyama, K., et al. 2009, PASJ, 61, 209

Sawada, M., Tsuru, T. G., Koyama, K., & Oka, T. 2011, PASJ, 63, 849

Sidoli, L., Mereghetti, S., Israel, G. L., et al. 1999, ApJ, 525, 215

Serlemitsos, P. J., et al. 2007, PASJ, 59, S9

Smith, R. K., et al. 2001, ApJS, 556, L91

Sofue, Y. 1995, PASJ, 47, 527

Tanaka, Y., Koyama, K., Maeda, Y., & Sonobe, T. 2000, PASJ, 52, L25

Uchiyama, H., Ozawa, M., Matsumoto, H., et al. 2009, PASJ, 61, 9

Uchiyama, H., Nobukawa, M., Tsuru, T., Koyama, K., & Matsumoto, H. 2011, PASJ, 63, 903

Uchiyama, H., Nobukawa, M., Tsuru, T., Koyama, K. 2012, accepted to PASJ, arXiv:1209.0067

Revnivtsev, M., Sazonov

Rieke, G. H., Rieke, M. J., & Paul, A. E. 1989, ApJ, 336, 752

Schawinski, K., Evans, D. A., Virani, S., et al. 2010, ApJ, 724, L30

L. Strüder et al., A&A, 365, L18, 2001

Sunyaev, R. A., Markevitch, M., & Pavlinsky, M. 1993, ApJ, 407, 606

Sunyaev, R., & Churazov, E. 1998, MNRAS, 297, 1279

Suzaku Technical Description, 2011, http://www.astro.isas.ac.jp/suzaku/doc/suzaku_td/

Takahashi, T., et al. 2007, PASJ, 59, S35

Tatischeff, V. 2003, EAS Publications Series, 7, 79

Tawa, N., Hayashida, K., Nagai, M., et al. 2008, PASJ, 60, 11

Terashima, Y., & Wilson, A. S. 2001, ApJ, 560, 139

Terrier, R., Ponti, G., Bélanger, G., et al. 2010, ApJ, 719, 143

Torii, K., Kudo, N., Fujishita, M., et al. 2010, PASJ, 62, 1307

Tsuboi, M., Handa, T., & Ukita, N. 1999, ApJS, 120, 1

Tsuru, T. G., Nobukawa, M., Nakajima, H., et al. 2009, PASJ, 61, 219

Turner, M. J. L., Abbey, A., Arnaud, M., et al. 2001, A&A, 365, L27

Watson, M. G., Willingale, R., Hertz, P., & Grindlay, J. E. 1981, ApJ, 250, 142

Warwick, R. S., Turner, M. J. L., Watson, M. G., & Willingale, R. 1985, Nature, 317, 218

Worrall, D. M., Marshall, F. E., Boldt, E. A., & Swank, J. H. 1982, ApJ, 255, 111

Weisskopf, M. C., O'dell, S. L., & van Speybroeck, L. P. 1996, Proc. SPIE, 2805, 2

Yamauchi, S., Kawada, M., Koyama, K., Kunieda, H., & Tawara, Y. 1990, ApJ, 365, 532

Yamauchi, S., Ebisawa, K., Tanaka, Y., et al. 2009, PASJ, 61, 225

Yuasa, T., Makishima, K., & Nakazawa, K. 2012, ApJ, 753, 129

Yuasa, T., Nakazawa, K., Makishima, K., et al. 2010, A&A, 520, A25

Yusef-Zadeh, F., Choate, D., & Cotton, W. 1999, ApJ, 518, L33

Yusef-Zadeh, F., Muno, M., Wardle, M., & Lis, D. C. 2007, ApJ, 656, 847

Yusef-Zadeh, F., Arendt, R., Bushouse, H., et al. 2012, ApJ, 758, L11

Zhang, S. N., Cui, W., Harmon, B. A., et al. 1997, ApJ, 477, L95

List of Figures

2.1 Optical picture of the Milky Way galaxy. 4

2.2 Global view of the Galaxy. 5

2.3 Optical extinction map of the Galaxy. 5

2.4 Radio CO map of the Galaxy. 7

2.5 Face-on view of the molecular gas in the Galaxy. 7

2.6 Radio CS map of the central molecular zone. 9

2.7 Different predictions on the face-on view of the central molecular zone. . . . 9

2.8 Mass correlation between the super mass black hole and its host bulge. . . . 10

2.9 Proper motions of S stars around SMBH, Sgr A*. 11

2.10 X-ray Image of the vicinity of Sgr A* by Chandra. 11

2.11 X-ray spectra of Sgr A*. 12

2.12 Short X-ray flares of Sgr A*. 13

2.13 X-ray observation of the Galactic ridge by Tenma. 14

2.14 6.7 keV mapping of the Galactic center by Ginga. 15

2.15 CCD X-ray spectra of the GC region by ASCA and Suzaku. 16

2.16 X-ray band maps of the GC plasmas by Suzaku. 19

2.17 Intensity profiles of the plasma emission lines from the GC by Suzaku. . . . 20

2.18 Intensity distribution of the 6.4 keV emission in the GC by ASCA. 21

2.19 Equivalent width of the 6.4 keV line produced by protons and electrons. . . . 22

2.20 X-ray spectra of giant MCs in the GC region. 24

2.21 Time variabilities of the 6.4 keV flux from giant MCs in a few years. 24
2.22 Schematic face-on view of the XRN geometry. 25
2.23 The 6.4 keV map of the Galactic center by Suzaku. 27

3.1 Schematic view of the Suzaku satellite in orbit. 30
3.2 Configuration of the detectors in the Suzaku satellite. 31
3.3 Schematic view and picture of the XRT. 33
3.4 Schematic cross-section of Wolter-I type X-ray mirror. 34
3.5 Total effective area and vignetting of the XRT. 35
3.6 The Image of SS Cyg at the optical axis taken with XRT-I0. 36
3.7 PSF and EEF of the XRT. 36
3.8 Readout architectures of CCD and APS. 38
3.9 Picture and cross-section of XIS sensor. 38
3.10 XIS/CCDs in front illumination and back illumination. 39
3.11 Schematic view of the XIS CCD. 40
3.12 QE of the XIS. 40
3.13 Long-term trend of the XIS energy resolution. 42
3.14 XIS spectra of the NXB. 43

4.1 XIS band images around the Sgr B region. 47
4.2 One-dimensional profiles of the Sgr B region. 49
4.3 FI spectra of M 0.74-0.09 and Sgr B2. 50
4.4 Schematic view of the MCs distribution along the line of sight. 53
4.5 Correlations between the 6.4 keV-line flux and absorptions. 57
4.6 Flux distribution of the 6.7 keV and 2.45 keV lines. 59
4.7 Relative positions of each Sgr B MC along the line of sight. 60
4.8 The absorption (Abs1) vs the distance-corrected 6.4 keV-line flux. 62

5.1 XIS (FI+BI) images near the Sgr C region. 67
5.2 A schematic face-on view for line-of-sight alignment for Sgr C. 69
5.3 Simulated XIS/FI spectrum of GCPE. 70
5.4 Simulated XIS-FI spectra of the GCPE for the parameter R. 70
5.5 Fitting results for Sgr C spectra. 72
5.6 Light curves (2006–2010) of the 6.4 keV intensity near Sgr C. 73

6.1 XIS band images near the Sgr D and E regions. 79
6.2 XIS spectra of 6.4 keV clumps in Sgr D and Sgr E. 80
6.3 Radio CO maps of the Sgr D and Sgr E regions. 82

7.1 l distribution of absorption, GCPE, and FE in the GC region. 84
7.2 Spatial distribution of the GCPE. 85
7.3 Line-of-sight position (Y_0) as a function of the parameter R. 87
7.4 3-D distribution of the XRNe around Sgr A*. 89
7.5 Face-on distribution of the XRNe around Sgr A* and X1/2 orbits. 91
7.6 Velocity distribution of XRNe near the GC. 92
7.7 Face-on view of XRNe around Sgr A*. 95
7.8 X-ray light curve of Sgr A* in the past six centuries. 96
7.9 Comparison between Sgr A*, Galactic black holes, and LLAGNs. 98

List of Tables

3.1 Summary of the Suzaku capabilities. 32

4.1 Suzaku Observations near the Sgr B Region 46
4.2 Summary of free and fixed parameters in the fittings for Model A, B, and C. 54
4.3 Results of best-fit parameters* with Model A and B. 55
4.4 Detailed results of best-fit parameters with Model C. 57

5.1 Suzaku Observations at the Sgr C Region. 66
5.2 Best-fit spectral parameters of the Sgr C regions*. 74

6.1 Suzaku Observations near the Sgr D and Sgr E Regions. 78
6.2 Spectral fitting results of 6.4 keV clumps in Sgr D and Sgr E. 81

7.1 Three-dimensional positions* of XRNe. 88
7.2 Association of XRNe with radio structures in the CMZ. 93
7.3 Parameters† of XRNe and past luminosity of Sgr A*. 97

Acknowledgments

I express my deepest thanks to my supervisors Prof. T.G. Tsuru and Prof. K. Koyama for giving me the chance, instruction, advice, and encouragement to carry out this challenging and interesting study.

This work would also not be completed without fruitful discussions with Dr. M. Nobukawa and Dr. H. Uchiyama.

I really enjoyed the days with the other instructors and colleagues in (or had been in) the Kyoto-U/cosmic-ray (CR) group, which was indispensable for a productive and healthy academic life.

I want to thank people at KEK and MIT with whom I have worked on the SOIPIX detector.

Finally, I am so grateful to my family for the selfless supports throughout my student career.